FEMTOSECOND LASER MICROMACHINING OF LITHIUM NIOBATE

FEMTOSECOND LASER MICROMACHINING

OF

LITHIUM NIOBATE

By

PAUL T. DRIEDGER, B.Sc.

A Thesis

Submitted to the School of Graduate Studies

in Partial Fulfilment of the Requirements

for the Degree

Master of Applied Science

McMaster University

MASTER OF APPLIED SCIENCE (2006)   McMaster University
(Engineering Physics)   Hamilton, Ontario

TITLE: Femtosecond Laser Micromachining of Lithium Niobate

AUTHOR: Paul T. Driedger, B.Sc. (Queen's University)

SUPERVISORS: Professors Rafael N. Kleiman and John S. Preston

NUMBER OF PAGES: ix, 95

Abstract

Lithium niobate is an important photonic material that has potential applications in MEMS. Unfortunately, it is difficult to process using conventional methods. This thesis is an exploratory study to determine the viability of using a femtosecond laser as a fabrication tool for lithium niobate. Unexpectedly, a rich range of behaviour, likely arising from the complex material structure and composition, was discovered. Depending on the processing conditions, it was demonstrated that machining can either result in deep, high-aspect ratio grooves with minimal surrounding damage or dramatic modification of the lithium niobate to great depths with very little material removal.

When machining grooves, increasing the effective number of pulses N_{eff} (i.e. decreasing cutting speed) gave rapidly increasing ablation depths until a threshold was reached, after which the grooves were nearly filled with amorphous material. The depth of these amorphous channels rapidly saturates and becomes nearly independent of N_{eff}. The ablation depth dependence on fluence showed gentle and strong ablation regimes. The amorphous channel depth depended almost linearly on fluence. Subsequent laser passes over amorphous channels eventually removed the amorphous material from the groove, indicating a dependence on the time between laser pulses. Crystal orientation was not a factor.

The results are understood in terms of incubation and waveguiding. The first pulses ablate some material and incubate a channel of material below the surface. With further pulses, increasing incubation accelerates ablation. At the threshold N_{eff}, the absorption coefficient has increased enough that the next pulse is able to melt a significant amount of material, which expands to fill the groove. It is suggested that, initially, the amorphous material is able to guide subsequent pulses to the bottom of the channel, resulting in a very slowly increasing depth with N_{eff}. Subsequent passes cause ablation once again since compositional changes in the amorphous material have relaxed. Irradiated samples appear thermally reduced, which would create colour centres leading to increased absorption and thus incubation.

Femtosecond lasers are indeed able to create MEMS structures. Multiple passes in the ablation regime yielded deep grooves, with laser polarization perpendicular to the groove giving the best results. Fabrication of micro-cantilevers and bridges was demonstrated.

Acknowledgements

There are quite a few people who helped me throughout my graduate studies. First and most importantly, I would like to thank my supervisors Rafael Kleiman and John Preston for providing the opportunity to carry out this research. They have offered invaluable guidance, advice and discussion, without which I could not have completed this thesis. Special thanks go to Andrzej Borowiec, Travis Crawford and Henry Tiedje, who provided continuous assistance and advice in the lab. The microscope work was done with the help of Chris Butcher, Steve Koprich, Fred Pearson, Gianluigi Botton and Graham Pearson. Ken Baker was a great help in taking many of the images. I would also like to thank the others in my research group, in no particular order, Edgar Huante, Rob Lockhart and Oleksa Hulko, for making this an interesting place to work. Finally, I am grateful to my parents, sister, grandmother and wife for their love, encouragement and support.

Table of Contents

List of Figures

Chapter 1 Overview

1.1 Introduction

Lithium niobate is an important material in the field of integrated optics, and it is commonly used as a substrate for high-speed optical modulators, due to its strong electro-optic effect. "Indeed, in electro-optics it is the yardstick against which all other crystals are measured" [1]. It is also used in nonlinear optics, particularly for second-harmonic generation (SHG), holography and surface acoustic wave (SAW) devices for telecom applications. Lithium niobate is very well studied and its usefulness is undoubtedly established. Still, there is potential for further exploitation of its properties in other fields.

One such area is the growing field of microelectromechanical systems (MEMS). Lithium niobate would allow piezoelectric sensing and actuation, a distinct advantage that has been previously identified [2]. The additional advantage of its excellent optical properties would provide the opportunity to couple the electrical, optical and mechanical domains in novel devices. However, one significant barrier to this development is resistance of lithium niobate to common processing techniques such as wet etching [3].

Laser machining has long been a subject of interest and it may fill the processing void for lithium niobate. Laser ablation of a substrate, using any pulse duration, results in several key features. First, there is material removed from the sample surface. Among the other important features is a region surrounding the irradiated surface called the heat-affected zone (HAZ). The HAZ is a region over which heat diffuses causes thermal effects such as melting. Generally, a laser pulse heats a material by exciting electrons, which then relax on a time scale of a few picoseconds (10^{-12}s). A femtosecond is 10^{-15} seconds and femtosecond pulses are over before equilibrium can be reached between the electrons and the lattice. The result is a much smaller HAZ than occurs with nanosecond and longer pulses. The small HAZ allows very 'clean' features to be created with little collateral damage. Femtosecond lasers have been shown to be useful tools for micromachining metals, semiconductors and dielectrics.

When studying the ablation parameters of a material there are a few key quantities that are useful to establish. For single and multiple consecutive pulses on the same spot, one such parameter is the ablation threshold, which indicates how much energy is required for a single pulse to ablate the material. This threshold decreases with multiple pulses, due to incubation. Incubation is a material change on a microscopic level that results in increased absorption. For the machining of grooves, where the sample is

translated relative to the laser beam, it is desirable to characterize the ablation depth as a function of cutting speed, fluence and number of consecutive passes. Decreasing the cutting speed usually increases the ablation depth proportionally. With increasing pulse fluence, gentle and strong ablation regimes are often present. Multiple passes increase the groove depth.

This thesis is an exploratory study to determine the viability of using a femtosecond laser as a fabrication tool for lithium niobate. Laser interaction with lithium niobate has been studied in the past, though very few experiments have been carried out in the femtosecond regime. Many experiments have been performed below the ablation threshold to investigate refractive index changes, which are useful for holography and destructive to waveguides. However, in terms of ablation, most early studies focus on sputtering of thin films rather than micromachining, which brings about the motivation for this project

Machining of craters and grooves was carried out and, unexpectedly, a rich range of behaviour, likely arising from the complex material structure and composition, was discovered. When creating grooves, there are two main regimes, which depend on the processing conditions. For the first regime, it was demonstrated that machining can result in deep, high-aspect ratio grooves with minimal surrounding damage, as would be expected. The second regime involves dramatic modification of the lithium niobate to great depths with very little material removal.

When machining grooves, increasing the effective number of pulses N_{eff} (i.e. decreasing cutting speed) first gave rapidly increasing ablation depths until a threshold was reached, after which the grooves were nearly filled with amorphous material. The depth of these amorphous channels rapidly saturates and becomes nearly independent of N_{eff}. The ablation depth dependence on fluence showed the gentle and strong ablation regimes. The amorphous channel depth depended almost linearly on fluence. Subsequent laser passes over amorphous channels eventually removed the amorphous material from the groove, indicating a dependence on the time between laser pulses. Crystal orientation was not a factor, despite the highly anisotropic nature of the crystal.

The results are understood in terms of incubation and waveguiding. The first pulses ablate some material and incubate a channel of material below the surface. With further pulses, the increasingly strong incubation effect accelerates ablation. At the threshold N_{eff}, the absorption coefficient has increased enough that the next pulse is able to melt a significant amount of material, which expands to fill the groove. It is suggested that, initially, the amorphous material is able to guide subsequent pulses to the bottom of

the channel, resulting in a very slowly increasing depth with N_{eff}. Subsequent passes cause ablation once again since thermal or compositional changes in the amorphous material have relaxed.

The nature of the incubation effect was also studied. In separate experiments, irradiated samples appear thermally reduced. Thermal reduction in lithium niobate has been shown to create colour centres, which, in turn, lead to a broadband increase in absorption. This is a likely source of the incubation.

Finally, once the ideal ablation conditions were established, the usefulness of femtosecond lasers as a machining tool was investigated and, indeed, they were able to create MEMS structures. Multiple passes in the ablation regime yielded deep, high-aspect ratio grooves, with laser polarization perpendicular to the groove giving the best results. The fabrication of micro-cantilevers and bridges was demonstrated.

Given the central role of lithium niobate in so many areas and the successful femtosecond laser micromachining of other materials, it is a logical extension to explore the interaction of ultrashort laser pulses with lithium niobate. These first experiments can be used as a stepping-stone towards the development and fabrication of new MEMS devices.

1.2 Outline

The following chapters are organized into several main topics. Chapter 2 is an introduction to the important properties of lithium niobate as well as its applications. Chapter 3 includes a discussion of femtosecond lasers and pulses, as they are the main tools used in this research. Chapter 4 describes previous observations and parameters for femtosecond laser micromachining of other materials, followed by a review of results presented in the literature for lithium niobate to date. Chapter 5 describes the machining set up and experimental procedures. The results for femtosecond laser micromachining of lithium niobate are presented in Chapter 6, along with a discussion of the important observations. With applications of lithium niobate in MEMS as motivation for this research, Chapter 7 provides a preliminary discussion of femtosecond lasers as a machining tool in this respect and potential device configurations. Chapter 8 summarizes the results that are presented and includes some concluding remarks.

Chapter 2 Fundamentals of Lithium Niobate

Lithium niobate is a very well studied compound and over the past twenty years its technological importance has grown immensely. Since the goal is of this project is to establish the viability of femtosecond laser micromachining as a processing tool for lithium niobate, it is pertinent to include a description of some of the properties that may be useful in a MEMS devices. With this in mind, this chapter describes important physical phenomena and applications associated with this material, of which there are many. Prokhorov and Kuz'minov [4] give detailed descriptions of many of the properties of lithium niobate and Wong [5] provides a comprehensive catalogue of measurements associated with these properties. Of particular interest to this study is the rich variety of lithium niobate phases that exist. The most widely used form of lithium niobate, lithium metaniobate, exists only in a narrow region of the phase diagram, and its most useful properties are sensitive to composition.

2.1 Properties

2.1.1 Structure, Growth and Composition

Lithium niobate is an anisotropic crystalline material, which normally is clear and colourless. It is commonly available in wafer form in three orientations, x- y- and z-cut, corresponding to principal crystal axes. Various wafer thicknesses are available with either single- or double-sided polishing.

The structure of lithium niobate is a distorted cubic perovskite, a face-centred cubic with an atom at the body centre. In this case, oxygen is at the face centres, lithium is at the body centre and niobium is at the corners. Lithium niobate is also commonly described as stacked oxygen octohedra, alternating with lithium, niobium and a vacancy within. Agullo-Lopez [6] includes an excellent illustration. The axis through the Li and Nb atoms is the c- or z-axis and the perpendicular axes are x and y. The octohedra are distorted, with the O-O separation differing with location and the metal ions not being at the centre of the octohedra. The crystal is therefore non-centrosymmetric.

Lithium niobate crystals are commonly grown by the Czochralski method from a melt consisting of Li_2O and Nb_2O_5. The phase diagram of this system, as shown in Figure 2-1, is very complex and obtaining high-quality, uniform crystals is a non-trivial process. Originally, the melts used to create solid lithium niobate had a Li_2O/Nb_2O_5 ratio of 1 and the crystals were believed to have an identical stoichiometric composition.

However, the optical properties of these crystals were found to be non-uniform due to a varying deficiency of lithium. Crystals that have the same composition as the melt (congruent crystals) can be formed from a melt with a Li_2O/Nb_2O_5 ratio of 0.94 [1]. Congruent crystals have an optimal optical uniformity [7] and are the most widely used for optical applications. Stoichiometric crystals can be grown from melts with a Li_2O/Nb_2O_5 ratio of 1.4.
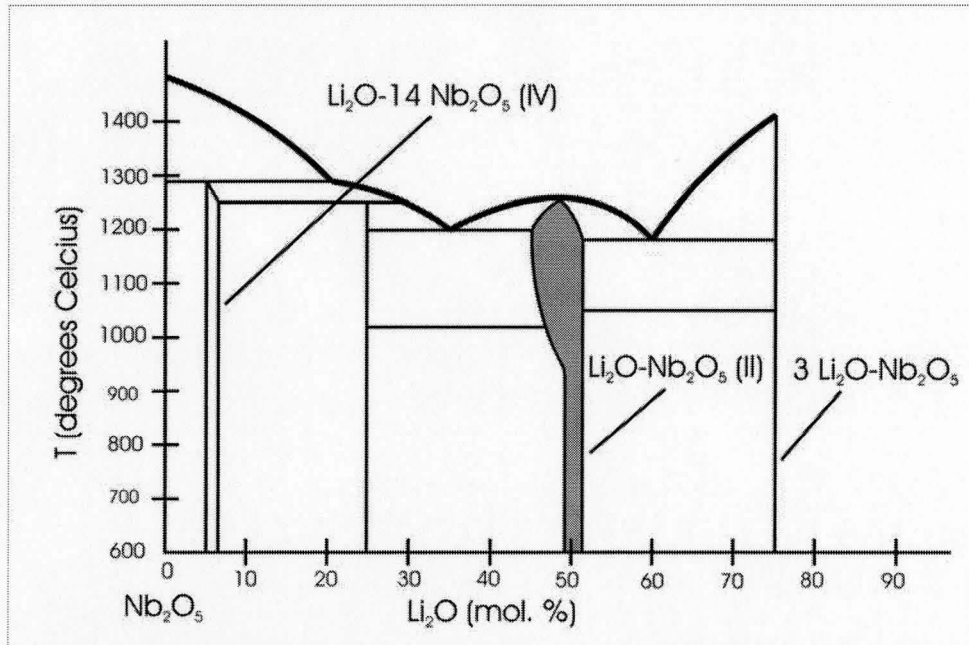
Figure 2-1: Approximate phase diagram for the Li_2O-Nb_2O_5 system. The most useful form of lithium niobate (lithium metaniobate) is in the shaded region. (Adapted from Prokhorov and Kuz'minov)

The departure of congruent lithium niobate from stoichiometry implies that there are a number of point defects in the crystal in order to maintain space-charge neutrality. It has been shown that the predominant defects are Li^+ and O^{2-} vacancies.

2.1.2 Ferroelectric Properties

Lithium niobate is a ferroelectric material, meaning it has a permanent but reversible spontaneous polarization. This dipole moment is due to the position of the metal ions relative to the oxygen lattice.

At elevated temperatures (i.e. above the Curie point), Li atoms can be found in the oxygen layer (between octohedra) and the Nb atoms along the z-axis are separated equally between the oxygen layers. This is the para-electric state. Upon cooling, the lithium ion is removed from the oxygen layer and constrained to one octahedron (above or below). To maintain maximum spacing between Li and Nb atoms, the Nb atoms shift

5

but are also constrained by the oxygen layers and the distance from the Li atoms to the Nb atoms above and below are different. This spacing difference gives rise to the dipole moment, which can be either parallel or anti-parallel to the z-axis, as shown in Figure 2-2. This is the ferroelectric state. Regions of a crystal can have oppositely oriented dipoles corresponding to positive and negative domains. Upon heating again, the para-electric state is re-established and the dipole lost. This temperature dependence of the dipole is called the pyroelectric effect.

If a crystal above Curie point is cooled in the presence of an electric field aligned positively or negatively with the z-axis, the dipole will be aligned with the field. This process is called poling. Wafers are available as single-domain or with multiple periodic domains (periodically poled lithium niobate, PPLN).
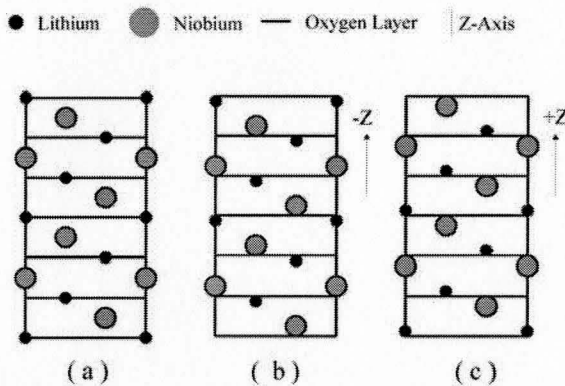
Figure 2-2: Dipole orientation and position of atoms in lithium niobate in (a) the para-electric state, (b) a negative domain and (c) a positive domain (Adapted from Prokhorov and Kuz'minov, 1990)

When an electric field is applied to a crystal below the Curie point, the permanent dipole can be made weaker if the field is aligned opposite the dipole and reversed if the field is strong enough. The polarization dependence on this external field displays a hysteresis loop as shown in Figure 2-3, a characteristic of all ferroelectrics. At electric fields above point A and below D, the behaviour is linear. At B and E (zero field) the polarization is equal to the spontaneous polarization. The field C and F (zero polarization) is the coercive field. At room temperature, as the electric field is increased, electrical breakdown in lithium niobate will occur before the polarization is inverted.

Another property of ferroelectrics is that they are piezoelectric, since a mechanical stress will affect the dipole. As a result, the relationship between stress and strain has an electric field dependence and the relationship between surface charge density (polarization) and the electric field has a stress/strain dependence. Damjanovic [8] gives further details on the properties of ferroelectrics.
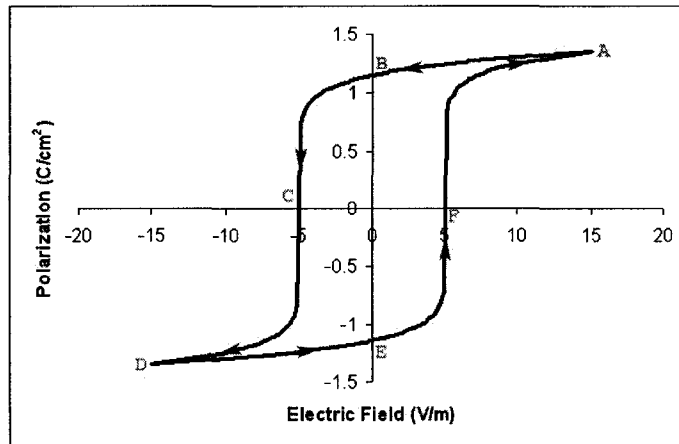
Figure 2-3: An arbitrary ferroelectric hysteresis loop showing dipole polarization dependence on an external electric field.

2.1.3 Optical Properties

The dielectric constant for lithium niobate is direction-dependent and the crystal is birefringent. The birefringence decreases with increasing temperature, but remains non-zero above the Curie temperature. It is uniaxial negative, where $n_o > n_e$ and n_o is the ordinary index and n_e is the extraordinary index. The extraordinary axis is aligned with z-axis. Prokhorov and Kuz'minov [4] and Wong [5] give extensive refractive index data.

The electronic bandgap of lithium niobate is indirect [9] and has a value of approximately 3.9 eV ($\lambda = 317$ nm) [4]. It is nominally transparent in the wavelength range of 0.4 µm to 5 µm. The transmission spectrum is given by Prokhorov and Kuz'minov [4]. High temperature annealing in an inert atmosphere causes the crystal colour to change from clear to yellow to brown to dark brown, as noted by [10]. As proposed by Arizmendi et al. [11], this is due to loss of oxygen and the creation of F and F^+ centres, which cause an increase in absorption in broad bands, centred at 2.6 eV (477 nm) and 3.1 eV (400 nm). A further absorption band at 1.6 eV (775 nm) can be induced with irradiation in either of the previous two bands.

2.1.4 Electro-Optic Properties

The electro-optic effect refers to a change in the refractive indices of a material induced by an external electric field and is explained by Agullo-Lopez [6] and Saleh and Teich [12]. Equation 2-1 gives a general expression for the refractive index of a material, showing its dependence on the electric field E applied to the material. The coefficient a_1 describes the Pockels, or linear electro-optic, effect and the coefficient a_2 describes the Kerr, or quadratic electro-optic, effect. Since lithium niobate is non-centrosymmetric, it displays the Pockels effect. The Kerr effect is negligible.

7

$$n(E) = n + a_1 E + \frac{1}{2} a_2 E^2 + \dots \quad 2\text{-}1$$

The electro-optic effect for a material is described by the electro-optic tensor r_{ij}. A simplified electro-optic tensor for lithium niobate is shown in Equation 2-2. The coefficient r_{33} is largest, so the electro-optic modulation of the index is most efficient when a field is applied in the z-direction. For an electric field applied in the z-direction and light propagating along the x-axis, the changes in index are given by Equation 2-3.

$$r_{ij} = \begin{bmatrix} 0 & -r_{12} & r_{13} \\ 0 & r_{12} & r_{13} \\ 0 & 0 & r_{33} \\ 0 & r_{42} & 0 \\ r_{42} & 0 & 0 \\ -r_{12} & 0 & 0 \end{bmatrix} \quad 2\text{-}2$$

$$\Delta n_o = \frac{1}{2} r_{33} n_o^3 E_z \quad \text{(a)}$$

$$2\text{-}3$$

$$\Delta n_e = \frac{1}{2} r_{33} n_e^3 E_z \quad \text{(b)}$$

2.1.5 Non-Linear Optical Properties

Lithium niobate is a nonlinear optical material, meaning the spontaneous polarization P depends on the square of an external electric field E as well as on the linear term in Equation 2-4 [12], where χ is the electric susceptibility and d and $\chi^{(3)}$ represent the nonlinear coefficients.

$$P = \varepsilon_o \chi E + 2 d E^2 + 4 \chi^{(3)} E^3 + \dots \quad 2\text{-}4$$

When E is an optical field of sufficient intensity such that the second order term is not negligible, several effects can arise from this nonlinearity. Second harmonic generation (SHG) is the most widely studied second order effect in lithium niobate. Third order effects are present in lithium niobate but are generally not significant. These phenomena are described in many texts, including Saleh and Teich [12].

2.1.6 Acousto-optic Effect

Lithium niobate also displays the acousto-optic effect, by which a sound wave travelling through the material induces a moving periodic modulation of the refractive index. This periodic index change can act as a Bragg grating and diffract light waves propagating within the material. The frequency of the sound wave can affect the diffraction angle and the frequency of the optical beam. Surface acoustic waves (SAW) can be launched in lithium niobate with the use of interdigitated electrodes by means of the inverse piezoelectric effect. Arizmendi [13] describes further details.

2.1.7 Photorefractive Effect

Another important property observed in lithium niobate is the photo-refractive effect, which refers to the refractive index change caused by illumination of the crystal.

Light incident on the material excites electrons, from donor impurity ions, usually Fe in lithium niobate, at a rate proportional to the intensity. The electrons then drift away from the illuminated region and are trapped elsewhere by acceptor impurity ions. The result is a non-uniform distribution of electric charge, which creates an internal electric field and locally modifies the refractive index through the electro-optic effect. A simplified model of this effect is presented in Saleh and Teich [12].

2.2 Applications

Lithium niobate has, to date, found a wide array of applications in photonics [1,13] and devices using all of the properties described in the previous section have been fabricated. In telecommunications, intensity modulators, based on the Mach-Zehnder interferometer and the electro-optic effect, have been fabricated. SHG is another common application for lithium niobate, as is difference frequency generation which can be used to generate infrared wavelengths for use in spectroscopy. SAW devices include multi-port optical switches and spectrum analyzers. The photorefractive effect also has the potential to be employed in devices. While it destroys the uniformity of the refractive index, and is thus destructive to waveguides, it does allow lithium niobate to be used as a holographic data storage medium. Many of these photonic devices involve the use of integrated waveguides and electrodes in various configurations. Waveguide and electrode fabrication in lithium niobate are well established.

Lithium niobate would be an ideal material for use in MEMS. Its piezoelectric effect would allow actuation that depends linearly on the applied voltage V instead of the V^2 dependence of the widely used electrostatic actuation [2] and its extensive optical properties would also allow a coupling of the optical, mechanical and electrical domains. However, there is almost no mention whatsoever of lithium niobate MEMS (SAW devices excepted) in the literature. This neglect is possibly due to the resistance of lithium niobate to common micromachining techniques [5] making the creation of complex microstructures difficult. While differential etching can be used to make relatively deep grooves [14], the process is slow.

2.3 Summary

Lithium niobate, $LiNbO_3$, is a very well studied ferroelectric compound. It has a complex structure and it exists in its most useful form in a narrow range of lithium dioxide content. It has been an important material in photonics due to its electro-optic, nonlinear optical, acousto-optic and photorefractive properties. Applications include,

among others, optical switches and intensity modulators, as well as holographic data storage. It has potential in MEMS but the lack of a viable micromachining process has inhibited this application. It was with this last point in mind that this work was carried out.

Chapter 3 Femtosecond Laser Systems

The previous chapter introduced many properties of lithium niobate that may be useful in MEMS devices. However, the resistance of lithium niobate to wet etching inhibits its application to this area. Femtosecond lasers have proved to be a useful tool for many types of materials and, in this work, their potential to overcome difficulties in lithium niobate processing is investigated. This project would be incomplete without a description of femtosecond pulses and the components of a femtosecond laser system. As such, these topics are addressed in this chapter.

3.1 Femtosecond Laser Pulses

A femtosecond laser pulse, also called ultrafast or ultrashort, is an optical pulse with duration on the order of 10^{-15} s. The generation of ultrashort pulses has been an active area of research [15] over the past several years.

Ultrashort pulses have two main characteristics. The first is their extremely high peak intensity. It is possible to obtain peak powers 100 TW with and higher with 25 fs pulses using a Ti:sapphire laser system [16]. This corresponds to intensities greater than 10^{20} W/cm^2 in a tightly focused beam, whereas in continuous-wave (CW) mode, the output power for a Ti:sapphire laser is 10 W [12]. The second is their intrinsically large bandwidth. Broadband femtosecond pulses having spectra with full-width at half maximum (FWHM) of 277nm (141 THz) have been reported [17]. Femtosecond pulses have been used in a wide variety of applications including imaging [18], holography [19], x-ray generation [20] and, of course, micromachining.

The remainder of this chapter describes optical pulses and the generation, amplification and characterization of femtosecond pulses. The discussion is derived mainly from Saleh and Teich [12] and Rullière [21], unless otherwise noted.

3.1.1 Optical Pulses

An optical plane wave can be described by Equation 3-1. This is a continuous monochromatic wave, infinite in duration with complex amplitude Eo, central angular frequency ω_0 and time-dependent phase term $\varphi(t)$. The spectral content of the wave can be determined using the Fourier transform. For the plane wave, this gives a delta function centred at ω_0. For simplicity, it can be assumed that the polarization of the wave is linear in the y-direction, propagation is in the z-direction and that $\varphi(t)=0$, giving Equation 3-2. To describe an optical pulse, the plane wave is modulated by the desired envelope function shape. A Gaussian pulse and its spectrum are given in Equations 3-3

and 3-4, where τ is the 1/e pulse half-width. When an optical wave is restricted in time, its spectrum broadens about the central frequency ω_o, as illustrated in Figure 3-1.

$$\mathbf{E}(\mathbf{r},t) = E_o e^{j(\omega_o t - \mathbf{k} \cdot \mathbf{r} + \varphi(t))} \quad \textbf{3-1}$$

$$E = E_o e^{j(\omega_o t - kz)} \quad \textbf{3-2}$$

$$E_{pulse}(t) = E_o e^{i(\omega_o t - kz)} e^{-\left(\frac{t}{\tau}\right)^2} \quad \textbf{3-3} \qquad E_{pulse}(\omega) = E_o \tau \sqrt{\pi} e^{\left(-\frac{\tau^2}{4}(\omega - \omega_o)^2\right)} \quad \textbf{3-4}$$
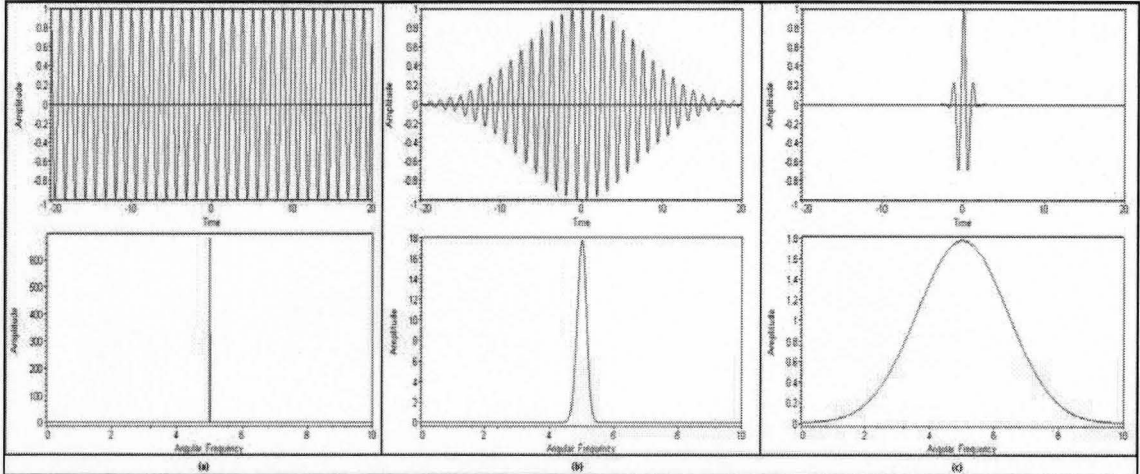
Figure 3-1: Time-domain plots and spectra of (a) a monochromatic wave, (b) a Gaussian pulse and (c) a short Gaussian pulse. Units are arbitrary.

Since a pulse is comprised of a continuum of frequencies, the instantaneous angular frequency will vary if the total phase of the pulse is not constant. The total phase is given by Equation 3-5 and the instantaneous angular frequency can be calculated using Equation 3-6. So, if $\varphi(t)$ varies with time such that $d\varphi/dt \neq$ const, the instantaneous angular frequency will vary with time. Figure 3-2 shows a Gaussian pulse with a quadratic phase term. The angular frequency is greater at one extreme of the pulse than it is at the other. Frequency variation within the pulse is called chirp and is an important effect to control when working with ultrashort pulses. Positive chirp occurs when the higher frequencies lag. Negative chirp occurs when the higher frequencies lead.

$$\Phi(t) = \omega_o t + \varphi(t) \quad \textbf{3-5} \qquad \omega(t) = \frac{\partial \Phi}{\partial t} = \omega_o + \frac{d\varphi(t)}{dt} \quad \textbf{3-6}$$

$$\Delta f \Delta t \geq K \quad \textbf{3-7}$$

12
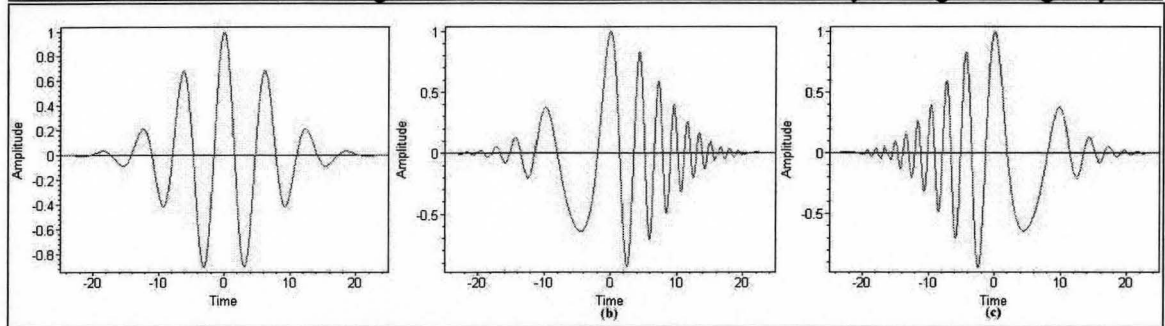
Figure 3-2: A Gaussian pulse with (a) no chirp, (b) positive chirp, (c) negative chirp.

Since the time and frequency representations of a pulse are related by a Fourier transform, the full width at half-maximum (FWHM) values of the pulse duration Δt and spectral width Δf are related by the inequality of 3-7, where K is on the order of unity and depends on the pulse shape. This inequality demonstrates the inverse relationship between pulse duration and bandwidth. When equality is attained, the pulse is Fourier transform-limited, having the shortest duration for a given bandwidth with no chirp.

3.1.2 Propagation of Optical Pulses

It is important to consider the effects of a medium on an optical pulse. The details of this discussion are explained in Saleh and Teich [12]. In dielectric media, the wave number k is complex and is given by Equation 3-8, where and k_o is the wave number in free space, χ is the susceptibility and β and $-1/2\alpha$ are the real and imaginary components of k. β is the propagation constant and α is attenuation coefficient, which are frequency-dependent.

$$k(\omega) = k_o \sqrt{1 + \chi'(\omega) + j\chi''(\omega)} = \beta(\omega) - j\frac{1}{2}\alpha(\omega) \quad \textbf{3-8}$$

For a wave propagating in a dielectric medium, a phase shift of e^{-jkz} is introduced. So, the plane wave of 3-9 with frequency ω_o, modulated by a harmonic complex envelope $A(z,t) = A(z,\omega)e^{j\omega t}$, becomes that of 3-10. By applying the slowly-varying wave approximation, the effect of the medium on the envelope is given by $H(\omega)$. The first exponential is an attenuation factor. The second exponential introduces a delay z/v_g, where $1/v_g = d\beta/d\omega$ is the group velocity of the pulse. The third exponential is a pulse broadening factor caused by the frequency dependence of the group velocity. This is known as group velocity dispersion (GVD). Frequency components of the pulse experience different delays which are characterized by the dispersion coefficient $D = d/d\omega(1/v_g)$.

$$U(z,t) = A(z,\omega)\exp(j(\omega_o + \omega)t)\exp(-j\beta_o z) \qquad \textbf{3-9}$$

$$U(z,t) = U(0,t)\exp(-jkz) = A(0,\omega)\exp(j(\omega_o + \omega)t)\exp\left(-j\beta(\omega_o + \omega)z - \frac{\alpha z}{2}\right) \quad \textbf{3-10}$$

13

$$H(\omega) = \frac{A(z,\omega)}{A(0,\omega)} \qquad = \exp\left(\frac{-\alpha z}{2}\right)\exp\left(-j\omega\frac{d\beta}{d\omega}z\right)\exp\left(-j\omega^2\frac{d^2\beta}{d\omega^2}z\right)$$

$$= \exp\left(\frac{-\alpha z}{2}\right)\exp\left(-j\omega\frac{z}{v_g}\right)\exp\left(-j\omega^2 Dz\right)$$

3-11

GVD causes a pulse to become chirped. In normally dispersive materials (D>0) and higher frequency components experience a greater delay than lower frequency components. In anomalously dispersive materials (D<0), the opposite is true. By controlling GVD, a pulse can be temporally expanded or compressed.

A Gaussian pulse propagating in a dispersive medium is given by 3-12. τ_o is the $1/e$ pulse half-width and the central frequency is delayed by $\tau_D = z/v_g$. The distance over which the spreading effects cannot be neglected is $z_o = \pi\tau_o^2/\text{-D}$. For a Gaussian pulse, the width after distance z is given by 3-13 and the amplitude by 3-14. The chirp is linear since the phase term is quadratic. Group velocity dispersion is illustrated in Figure 3-3. As the propagation distance z increases, the pulse broadens and becomes chirped.

$$A(z,t) = \left(\frac{jz_o}{z+jz_o}\right)^{\frac{1}{2}}\exp\left(j\pi\frac{(t-\tau_d)^2}{D(z+jz_o)}\right) \quad \textbf{3-12}$$

$$\tau(z) = \tau_o\sqrt{1+\frac{z}{z_o}} \qquad \textbf{3-13} \qquad A_z = \frac{\tau_o}{\sqrt{\tau_o^2 - \frac{Dz}{\pi}}} \quad \textbf{3-14}$$
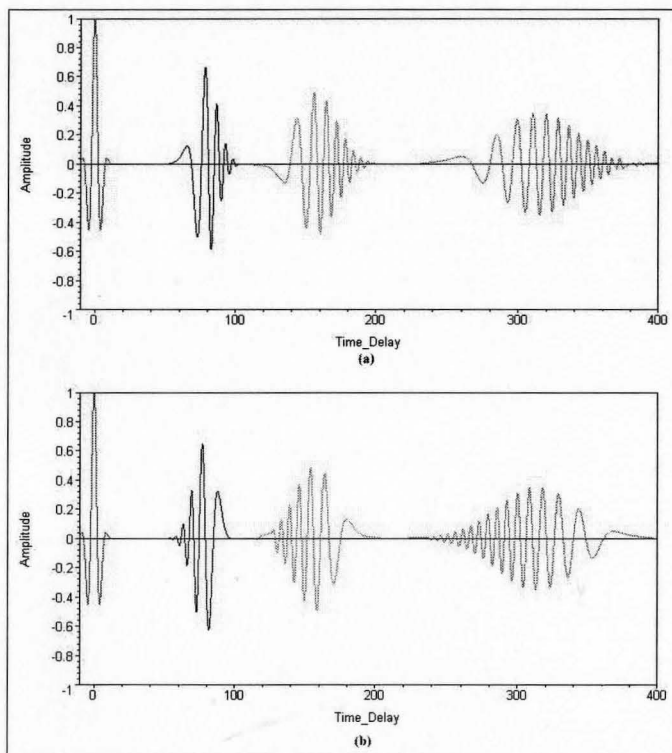
Figure 3-3: Propagation of a Gaussian pulse in (a) a normally dispersive medium and (b) an anomalously dispersive medium. Units are arbitrary. Both (a) and (b) show the pulse as a function of time for (from left to right) z=0, z=2z$_0$, z=4z$_0$ and z=8z$_0$.

There exist devices that are capable of compensating for chirp, expanding the pulse or compressing it back to its original duration by increasing or reducing chirp. Pairs of prisms or reflective gratings are commonly used. The effect of the gratings is to introduce different path lengths to the frequency components of the pulse, delaying certain frequencies more than others. A grating stretcher and compressor are shown in Figure 3-4.

(a)

(b)
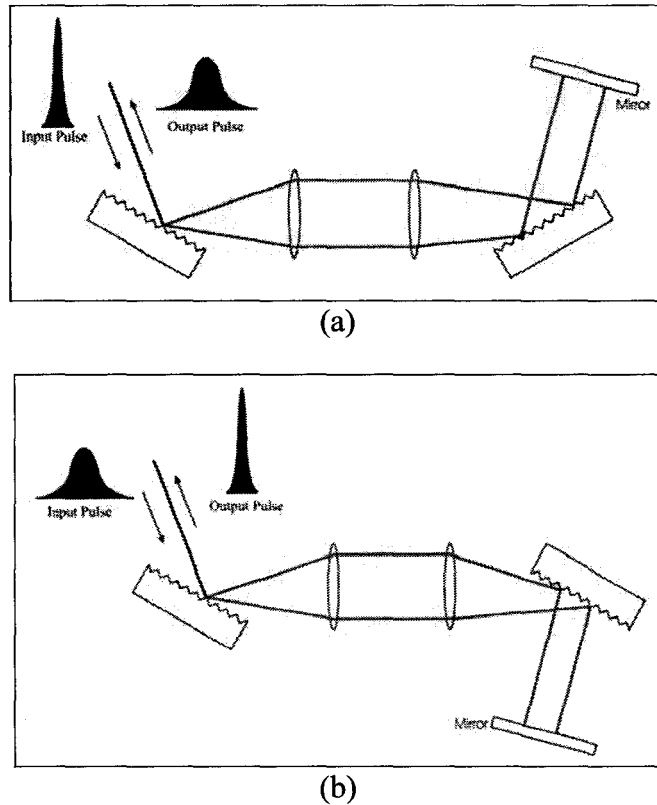
Figure 3-4: (a) Grating stretcher (b) Grating Compressor (adapted from [22])

Spatially, laser light is often described as a Gaussian beam. The beam profile is circular with the intensity following a Gaussian function across the diameter and peaking at the center. The beam radius $W(z)$ as a function of the propagation distance is given by Equation 3-15. At the beam waist z =0 and the radius is a minimum W_o. The spot size is $2W_o$ and the depth of focus of the beam is $2z_o$ where $z_o = 2\pi W_o/\lambda$. Beam divergence, or diffraction, also occurs. At large z, the increase in beam radius becomes linear and a divergence angle given by 3-16 can be defined.

$$W(z) = W_o\left[1 + \left(\frac{z}{z_o}\right)^2\right]^{\frac{1}{2}} \quad \textbf{3-15} \qquad \theta = \frac{2}{\pi}\frac{\lambda}{2W_o} \quad \textbf{3-16}$$

Since the peak intensities of ultrashort pulses are very high, nonlinear optical effects must be considered in dielectric media. In Kerr media, where the third order nonlinear effect is dominant, there are two main effects: self-focusing and self-phase modulation. Self-focusing occurs because large light intensities will cause an intensity-dependent change in refractive index. If the incident beam profile is Gaussian, the intensity is largest at the beam centre. This leads to an index gradient within the medium causing the beam to become increasingly focused. This effect, also called Kerr lensing, is eventually balanced by the large diffraction caused by a small beam radius. Self-phase modulation is also a consequence of the intensity-dependent index change. When high-intensity pulsed light travels in a Kerr medium, the index and thus the phase shift induced by the medium becomes time-dependent. This causes results in a delay of the high-frequency components [23], resulting in a chirped pulse.

3.2 Pulse Generation

One common laser used to generate femtosecond optical pulses is the titanium-sapphire (Ti:sapphire, Ti: Al_2O_3) laser. The reason for this is that it has a large gain bandwidth and a relatively simple resonant cavity.

Generally, a laser has multiple longitudinal modes that can oscillate its cavity. A Ti:sapphire laser has on the order of 100,000 longitudinal modes. During free-running operation, the modes oscillate independently, with random phase differences. The beam is CW but exhibits large fluctuations due to mode competition, as shown in Figure 3-5 (a). If the modes are locked together, such that the phase difference is constant in time, then the longitudinal modes represent the Fourier components of a periodic function and the laser output becomes a periodic pulse train as shown in Figure 3-5 (b).
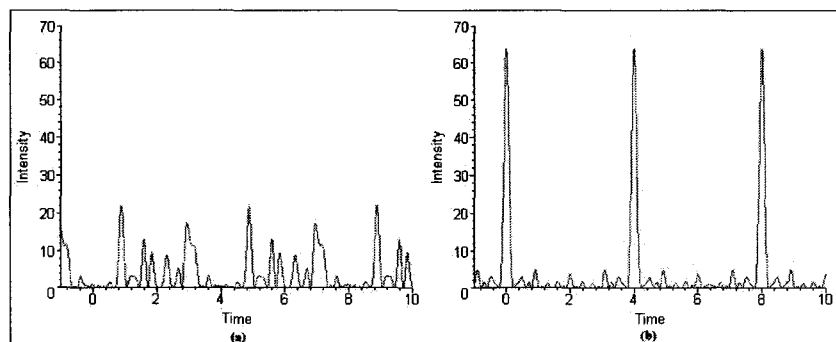
Figure 3-5: Intensity output of a laser (a) in the multi-mode regime and (b) the mode-locked regime

Ti:sapphire lasers create short pulses by the method of self-mode-locking, or Kerr lens mode-locking. The self-focusing effect causes the high intensity peaks of the beam to be spatially compressed, making them less susceptible to cavity losses. The lower

intensity wider part of the beam suffers a greater loss and the result is a sequence of high-intensity pulses. Self-mode locking is stable but it generally must be induced by creating an initial intensity variation between high intensity peaks and low intensity wings of the beam. Further details about generation of femtosecond pulses are given by Rullière [21].

3.3 Amplification of Ultrashort Pulses

In ultrafast beams, the energy per pulse is usually in the nano-Joule range but micro-Joule pulses are often required for micromachining purposes, requiring the pulses to be amplified. However, the peak intensities of femtosecond pulses are sufficiently high to cause damage to optical components even when the pulse energy is quite low, so direct amplification is not possible. Chirped-pulse amplification (CPA) [21] is used to overcome this difficulty. A chirped-pulse amplifier consists of a grating stretcher, a regenerative amplifier and a grating compressor. A time-stretched (chirped) pulse can be amplified without damage to optical components since the peak intensity is much lower. A regenerative amplifier consists of a resonator cavity with a gain medium (also a $Ti:Al_2O_3$ crystal), two Pockels cells and a thin film polarizer (TFP). The crystal is pumped by an external laser. The linearly polarized input pulse is reflected into the cavity and the polarization is rotated by the first Pockels cell PC1. The polarization is aligned with the TFP and the pulse oscillates in the cavity until the maximum amount of energy is transferred to the pulse. At that point, PC2 is activated and rotates the polarization of the pulse such that the TFP reflects the pulse out of the cavity. The process of CPA and a regenerative amplifier cavity are illustrated in Figure 3-6.

(a)

(b)
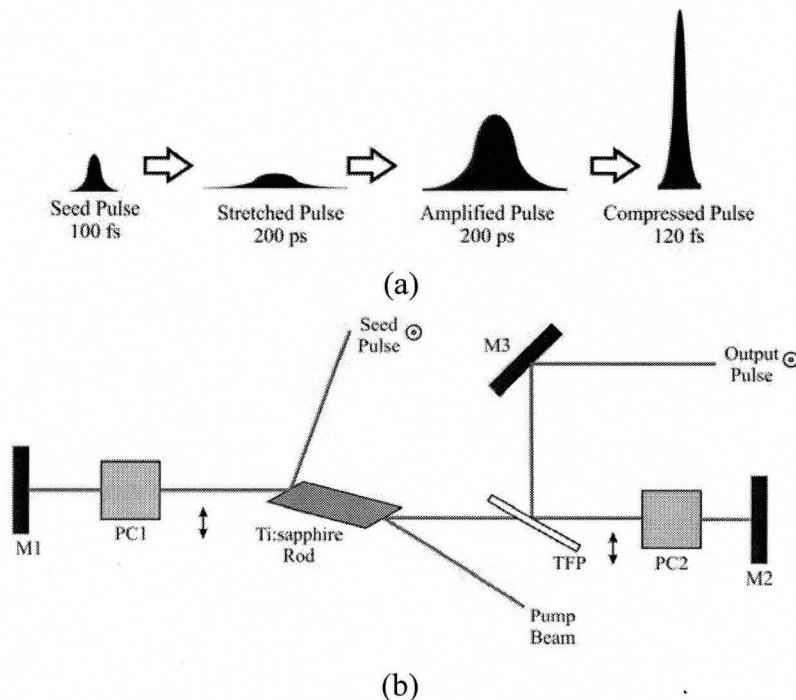
Figure 3-6: (a) Chirped-pulse amplification (b) A regenerative amplifier cavity

3.4 *Time Measurements of Ultrashort Pulses*

Direct temporal profile measurements of femtosecond pulses are not possible due to limitations in the response times of optical detectors. Photodiodes can only measure pulses down to several picoseconds, so ultrashort pulses require alternative methods.

A common technique for determining the time duration of ultrashort pulses is intensity autocorrelation. Autocorrelation is based on the use of a 'slow' detector to measure the time-integrated intensity profile of two identical pulses separated in time by a delay τ, as in Equation 2-1, where $A(\tau)$ is the autocorrelation function and $I(t)$ is the intensity profile of the pulses. Since the relationship of $A(\tau)$ to $I(t)$ is known, spread of the pulses in time can be determined if a model for $I(t)$ is assumed. The most common profiles assumed for femtosecond pulses are the Gaussian and hyperbolic-secant squared (sech^2) functions. The widths of the normalized autocorrelation traces are $\sqrt{2}$ and 1.543 times larger than the Gaussian and sech^2 intensity profiles, respectively.

$$A(\tau) = \int_{-\infty}^{\infty} I(t) \cdot I(t - \tau)\,dt \quad \text{3-17}$$

An intensity autocorrelator setup is based on the Michelson interferometer, as shown in Figure 3-7 (a). A beam splitter is used to split the pulses into two identical pulses with half of the original energy. The split pulses travel along the arms of the interferometer, one of which has a variable path length which controls the delay τ. The two pulses are then directed to parallel paths by the beam splitter and focussed to the same point in a nonlinear crystal. The focusing overlaps the pulses and the nonlinear crystal is used for second harmonic generation, creating an intensity function proportional to $\{E(t) \cdot E(t-\tau)\}^2$ or $I(t) \cdot I(t-\tau)$, which is detected and integrated by the photodiode to give $A(\tau)$. $A(\tau)$ is a maximum when the pulse overlap entirely and is zero when there is no overlap so, when the variable delay is scanned to vary the pulse overlap, the photodiode output will be a peak function with a shape similar to the assumed model (Gaussian or sech^2). A typical intensity autocorrelation trace is shown in Figure 3-7 (b).

(a)   (b)
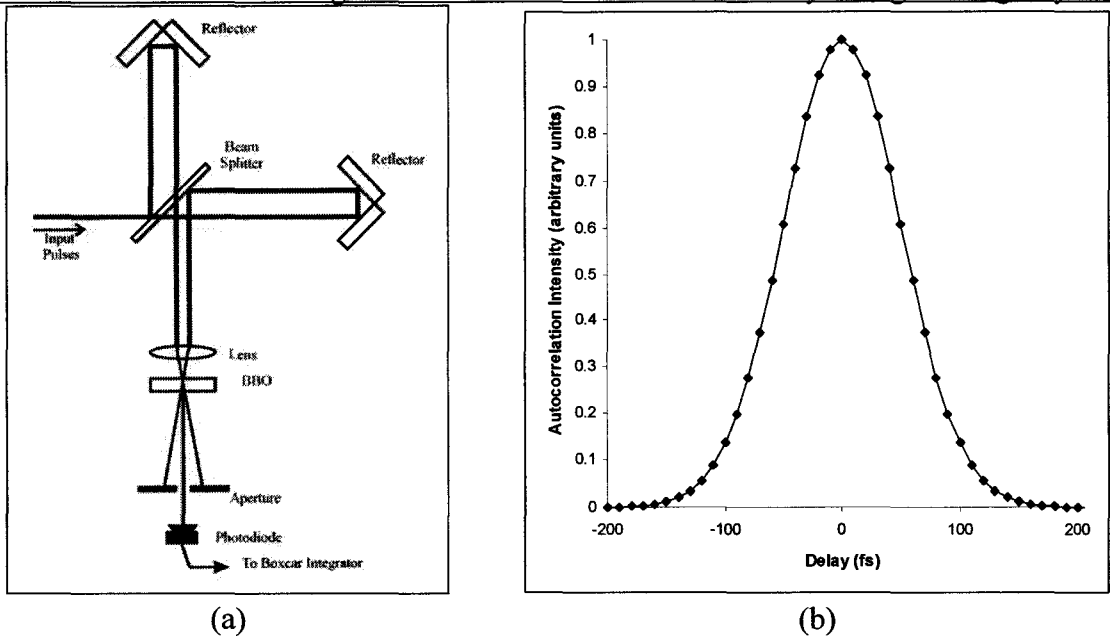
Figure 3-7: Intensity autocorrelation (a) setup (b) Typical trace

3.5 Summary

As they are the main tools used in this research, a discussion of femtosecond laser pulses was presented in this chapter. Femtosecond laser pulses have characteristic properties of large bandwidth and high peak power that make them ideal for many applications, including imaging and micromachining. Ti:sapphire lasers are among the most common femtosecond sources and, along with chirped-pulse amplification, are ideal for micromachining. Femtosecond pulses require indirect measurement techniques, such as intensity autocorrelation. These concepts are applied in the experiment procedure, which is discussed in Chapter 5. The following chapter discusses the effect of femtosecond radiation on a material surface.

Chapter 4   Femtosecond Laser Processing

The properties of both lithium niobate and femtosecond pulses are now familiar topics, as they have been addressed in the previous two chapters. Before introducing the results for femtosecond laser micromachining of lithium niobate (Chapter 6), laser interaction with materials is discussed. In the following sections, some of the current results pertaining to laser ablation processes, along with previous work on lithium niobate, are presented.

4.1 Characterization of Craters and Grooves

While little has been done in the area of femtosecond ablation of lithium niobate, many other materials have been studied in great detail. This section contains a basic description of the processes and parameters involved in femtosecond machining of dielectrics and semiconductors. Many of the details have been summarized by Kruger and Kautek [24] and Richardson et al. [25]. D. Ashkenasi et al. have studied ablation dynamics in detail [26].

The interaction of a laser pulse with a material surface results in several main features on the sample, which are depicted in Figure 4-1. Photon absorption causes the lattice to heat up. If a certain energy threshold is reached, there will be material vaporization or ablation, resulting in a crater and an expanding plasma plume, which exerts pressure on the surface resulting in a melt layer. Heat is dissipated in the surrounding material resulting in a heat-affected zone (HAZ). In sensitive materials, a shock-affected zone (SAZ) is also present.
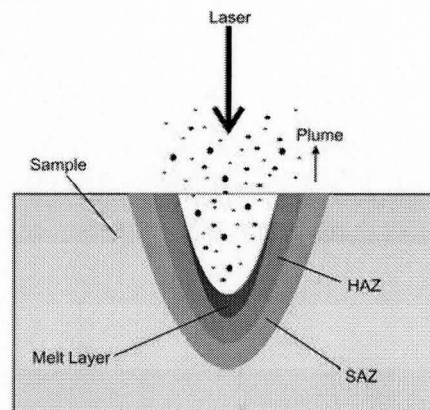
Figure 4-1: Sample features after irradiation with a laser pulse

Sample heating is due to optical excitation of electrons from their low energy state followed by relaxation. In opaque materials, linear absorption is the dominant

process. For transparent materials, the nonlinear process of multi-photon ionization provides seed electrons for avalanche ionization to occur [27]. As the electrons relax, there is an energy transfer to the material lattice, an interaction that occurs on a time scale of several picoseconds.

For pulses longer than a few picoseconds, the energy transfer can be modelled as heat diffusion, which yields a large volume of affected material. The pulse duration is also long enough such that the plasma plume shields the surface from the later portion of the pulse. The HAZ can be relatively large and the crater morphology is very rough. Craters often display highly non-uniform rims and cracking in the surrounding material. For femtosecond pulses, a more complicated energy transfer model is required and results have shown a largely reduced damaged area, smoother material removal and reduced shielding effects. A decrease in threshold with pulse duration is often observed and crater features include ripples [24] and pits [28], with little collateral damage.

The ablation threshold is a key parameter which is material-dependent since the optical energy absorbed depends on the reflective and absorptive properties as well as the thermal properties of the substrate. Most often the threshold is given in terms of fluence (J/cm^2) applied to the sample surface. For single-pulse ablation, the relationship of Equation 4-1 has been found to fit for many materials, where d is the crater depth, α is an absorption coefficient, F_o is the peak fluence of the pulse and F_{th} is the threshold fluence. So measurements of crater depth as a function of fluence will give the desired result. Alternatively, a method introduced by Liu [29] allows the determination of the ablation threshold from the crater diameter D according to Equation 4-2 assuming the pulse profile is Gaussian. This method also yields the beam waist radius ω_o, allowing a simple calculation of the peak fluence using Equation 4-3, where E is pulse energy.

$$d = \frac{1}{\alpha} \ln\left(\frac{F_o}{F_{th}}\right) \quad \textbf{4-1}$$

$$D^2 = 2\omega_o^2 \ln\left(\frac{E}{E_{th}}\right) \quad \textbf{4-2} \qquad\qquad \phi = \frac{2 \cdot E}{\pi \omega_o^2} \quad \textbf{4-3}$$

A decrease in the ablation threshold with N-pulse irradiation has also been observed in many materials. This phenomenon, known as incubation, is commonly characterized by Equation 4-4 [30], where ξ is degree of incubation. The form of Equation 4-5 is often plotted. Incubation is caused by a pre-ablation modification of the material, often involving the creation of defects in the irradiated material, which results in electron states within the bandgap and increased absorption. In barium aluminium borosilicate glass, colour centres are responsible for this increased absorption [31].

$$\phi_{th}(N) = \phi_{th}(1) \cdot N^{\xi-1} \qquad \text{4-4}$$

$$\ln(\phi_{th}(N)) = (\xi - 1)\ln(N) + \ln(\phi_{th}(1)) \quad \text{4-5}$$

Beyond single- and multiple-pulse ablation, micromachining of grooves for practical applications has been studied in various materials, though not in great detail for dielectrics. Characterization of femtosecond laser-machined grooves has been carried out thoroughly for indium phosphide by Borowiec [32]. In his groove cutting experiments, where the sample was translated relative to the laser beam, an approximate effective number of pulses N_{eff} delivered was considered, as in Equation 4-6, where f is the laser repetition rate and v is the translation speed. Groove depth h as a function of energy fluence was found to behave as Equation 4-7. At slower feed rates, gentle and strong ablation regimes were observed. Groove depth dependence on feed rate was characterized according to Equation 4-8. A, B and h_o are fit parameters. Multi-pass grooves were also machined with the depth approaching a finite limit. Laser polarization orientation with respect to the scanning direction was also found to affect groove quality.

$$N_{eff} = \sqrt{\frac{\pi}{2}} \frac{\omega_o f}{v} \qquad \text{4-6}$$

$$h(\phi_o) = h_o \ln\left(\frac{\phi_o}{\phi_{th}}\right) \qquad \text{4-7}$$

$$h(v) = \frac{A}{v} \quad \text{4-8 (a)} \qquad\qquad h(N_{eff}) = B \cdot N_{eff} \quad \text{4-8 (b)}$$

4.2 Laser Processing of Lithium Niobate

A systematic study of ablation parameters for femtosecond machining of lithium niobate is still lacking. One goal of this work is to begin this characterization. However, there has been interest in laser processing of lithium niobate, which is summarized here.

Prokhorov and Kuz'minov [4] review the work of several groups researching laser interaction with lithium niobate. Most early work involved the study of local variations of the refractive index (optical distortion) induced by laser light. Continuous wave irradiation resulted in the photorefractive effect. The effects of irradiation time, laser power, sample temperature and external electric fields on the change in refractive index were explored. It was concluded that irradiation of lithium niobate with a laser excites electrons to the conduction band. This excitation occurs even in the transparent portion of the spectrum, so energy levels must exist within the bandgap. Pulsed laser irradiation also showed the photorefractive effect, leaving a net residual change in refractive index that depends on pulse energy and number of pulses. No optical distortion threshold has been observed. Laser irradiation of lithium niobate also resulted in other physical effects. In the electrical domain, short circuit currents and the Hall

Effect were observed in illuminated crystals. A long-term distortion of the crystal structure was also found. The distortion, evident in localized inversions of the domain structure, is attributed to the inverse-piezoelectric effect induced by fields created by the non-uniform charge distribution.

Until recently, research into laser ablation of lithium niobate has been largely geared towards the deposition of high quality thin films [33,34] and the post-irradiation study of lithium niobate targets has been studied by only a few groups. Preuss [35] found that for irradiation with two 500 fs pulses, shielding effects are significant if the delay between them is less than a few picoseconds. During studies of laser-induced desorption of lithium niobate molecules, Affatigato et al. [36] noted that there are two dominant effects near the ablation threshold. They are an increased absorption, due to a change in composition and higher temperature, and an accumulation of defects near the surface, including colour centres and excess metal atoms. Sorescu [37] found a broadband increase in absorption in the visible wavelengths as well as recrystallization of different crystal phases and ablation in irradiated regions of iron-doped lithium niobate. Luo [38], as well, found new crystal phases were formed during fabrication of optical gratings. Bunton [39] was perhaps the first to propose a more complete mechanism for the ablation process in lithium niobate. A laser pulse first modifies the crystal resulting in a material with an increased absorption coefficient. Subsequent pulses then heat the material, further increasing the absorption, which leads to melting and vaporization. This is called the 'bootstrap effect.' The results suggest that pre-ablation material modification is the more important effect. Initial sample temperature and pre-exposure thermal reduction were found to have little effect, though laser pulses may locally cause thermal reduction since the area surrounding craters was discoloured due to the presence of polarons. Chong et al. [40] identify several types of damage induced by laser machining of grooves in lithium niobate of which surface discolouration surrounding the exposed region and 'exfoliation' near the grooves are the most notable. Discolouration is attributed, as with Bunton, to polaron creation. The exfoliation was assumed to be caused by shock waves. The experiments in this work were driven by a desire to create high aspect ratio features with minimum damage to the surrounding material. A SiO_2 over-layer improved groove quality greatly and it was suggested that ultrafast machining would also improve results.

All work reviewed so far has been carried using ultraviolet lasers and long pulse durations. UV lasers are able to drive ablation mechanisms in transparent materials via linear absorption. While ablation with ultrafast lasers requires high energies and short pulse durations for controlled multi-photon absorption, it is possible to focus below the surface to create structures in the bulk of the material, making the study of ultrafast

ablation processes worthwhile. A comparison of ultraviolet and ultrafast ablation in glass showed promising results [41].

Deshpande et al. [42] have done the most comprehensive study of femtosecond ablation of lithium niobate so far. In experiments using 800 nm, 300 fs pulses, craters were created using single and multiple pulses with the laser focus above and below the surface. The single- and 5-pulse ablation thresholds were reported as 2.5 and 1 J/cm^2, respectively. The decrease in threshold is attributed to material modification causing an increase in absorption coefficient and a rougher surface. Ablation rates decreased with a larger number of pulses due to material redeposition. Cracks appear around high-pulse-energy craters. Chemical analysis showed that near the surface of processed areas there was a deficiency of oxygen. An amorphous layer lined the surface of the craters, below which was a region of highly defective crystalline material. It is suggested that several phenomena are involved in the irradiation of lithium niobate with femtosecond pulses, including dielectric breakdown, melting, ablation, amorphization and shock-waves.

Most recently, Galinetto et al. [43] performed an ablation study using 810 nm, 130 fs pulses. They concluded that there was a highly defective crystalline structure near the ablated regions. Low energy, high repetition rate pulses caused the release of lithium from the surface and the formation of niobium oxides near the irradiated region. High energy, low repetition rate pulses resulted in the formation of a surface amorphous layer.

4.3 Summary

Femtosecond laser machining can be used to create craters with little affect to the surrounding material, as well as grooves. These features have been well characterized in many materials. The crater diameter squared for single and multiple pulses depends logarithmically on the number of pulses. The threshold decreases with an increasing number of pulses. For grooves, the depth increases logarithmically with fluence with gentle and strong regimes present. The groove depth is inversely proportional to the cutting speed and depends linearly on the effective number of pulses. Laser ablation studies of lithium niobate to date have been limited, focussing mainly on deposition of thin films and the use of ultraviolet lasers. It has been identified that femtosecond pulses affect the composition and crystal structure of lithium niobate but there remains a need for further characterization. This project begins this characterization, which is presented in Chapter 6. First, however, a detailed description of the experimental procedure is included in Chapter 5.

Chapter 5 Experimental Set-Up and Procedures

A sufficient introduction to the topic of laser processing in general, and lithium niobate in particular, has been presented and the results of the current study can be presented. First, however, for the benefit of those conducting future research on the topic, a description of the experimental apparatus and procedures is presented in this chapter.

5.1 Femtosecond Laser System and Procedures

The laser used for all experiments was a Spectra-Physics Ti:sapphire system. A diagram of the laser system is shown in Figure 5-1. The core of the system is a Tsunami femtosecond oscillator which uses a Ti:sapphire crystal as the gain medium. The Tsunami is pumped by the Millenia V, a frequency-doubled diode-pumped neodymium yttrium vanadate (Nd:YVO$_4$) laser (λ=532 nm). The output beam from the Tsunami is passed into the Spitfire chirped pulse-amplifier, which is in turn pumped by the Merlin frequency-double Q-switched Nd:YAG laser (λ=532 nm). The Spitfire output consists of 150 fs pulses at 800 nm, with a bandwidth of 10 nm and a repetition rate of 1 kHz.

Figure 5-1: Femtosecond Laser System
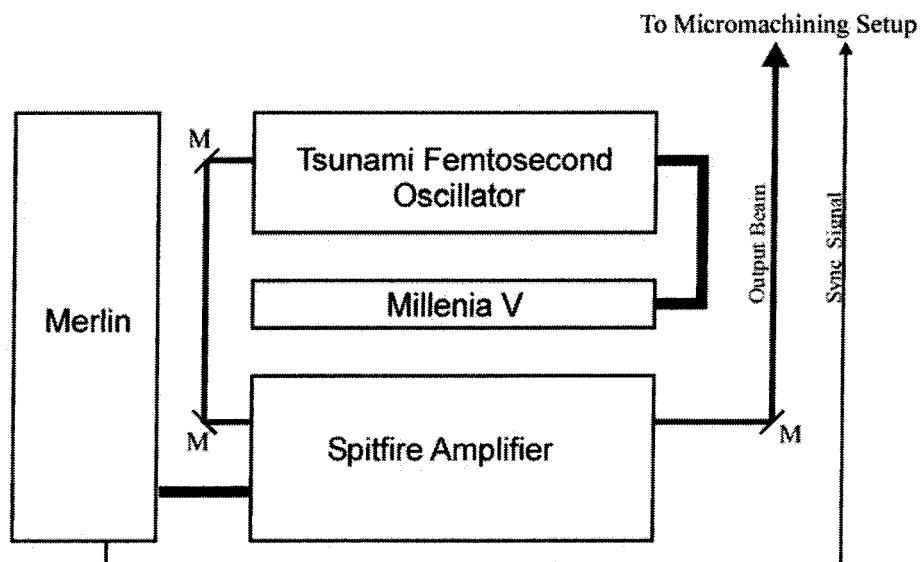
The output of the Spitfire was passed through a wide aperture and then directed to the machining set-up. While an aperture does modify the beam shape to a top-hat function which relaxes to a Bessel function, machining set-up was sufficiently far away to allow the beam profile to be approximated as Gaussian, an important assumption for later analysis. The machining setup is shown in Figure 5-2.
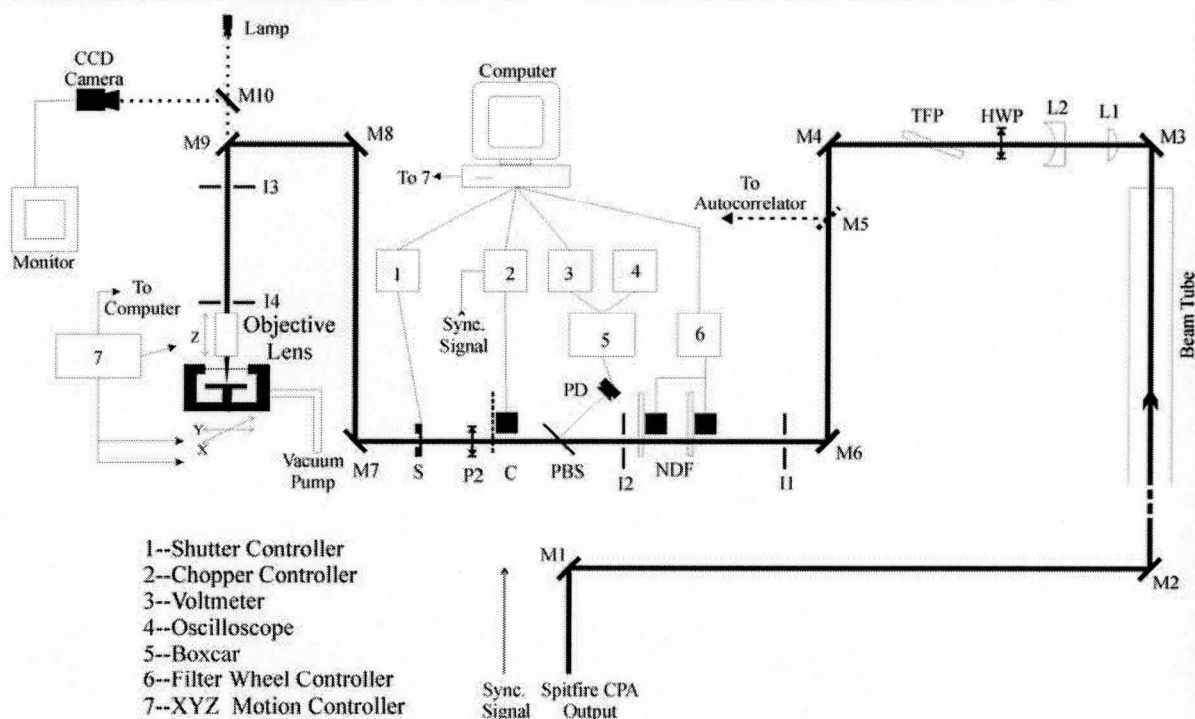
Figure 5-2: Laser micromachining setup

The beam diameter and pulse energy output from the Spitfire are approximately 10 mm and 100 μJ, respectively. The beam is directed to the machining setup using dielectric mirrors M1, M2 and M3. Lenses L1 and L2, achromatic doublet and plano-concave, respectively, serve to reduce the beam diameter for transmission through downstream optics. The half-wave plate HWP and thin film polarizer TFP are used to reduce the beam power to the maximum level used in ablation experiments. Typically, this was 20 μJ per pulse. The beam polarization is vertical before the HWP and horizontal after the TFP. M5 is a removable mirror which is inserted to direct the beam to an intensity autocorrelator for pulse duration measurements prior to machining experiments. Mirrors M4 and M6 are used to align the beam through irises I1 and I2. Neutral density filters NDF were mounted on two filter wheels. This allows easy stepwise attenuation of the beam. The neutral density filters can have optical density of 0.0 to 2.5 in steps of 0.1. A pellicle beam splitter PBS was used to continuously monitor the beam power via a photodiode and a boxcar integrator. The boxcar was triggered by the synchronization signal of the Merlin to ensure the power was measured at the time the pulses occurred. The boxcar gate and photodiode signal were observed with an oscilloscope. A voltmeter connected to the computer was used to record the photodiode signal. The laser had a repetition rate of 1 kHz. For single- and multiple-pulse experiments, an optical chopper C was used to decrease the repetition rate to 500 Hz. Nine of ten pulses were also blocked resulting in an end repetition rate of 50 Hz. A

mechanical shutter S triggered by the Merlin sync signal was used to pass single pulses. In some experiments, a polarizer P2 (half-wave plate or quarter-wave plate) was used to alter the beam polarization. Mirrors M8 and M9 were used to aligned the beam through irises I3 and I4 and through the focussing objective lens. The objective used for this work was a Mitutoyo M-Plan NIR 5x, with a working distance of 4 cm and focal length 3.7 cm. The objective was mounted on a vertical (Z) translation stage so the focus could be adjusted. The sample was placed on a level stage in a stainless steel vacuum chamber. The beam passed into the chamber through an anti-reflection-coated glass window that was protected from ablation debris by a microscope cover slip. The vacuum chamber was mounted on two perpendicular linear translation stages to allow for sample motion in the horizontal plane. A confocal CCD camera viewing system allowed for easy sample alignment and observation of experiments. The machining system was, for the most part, computer-controlled.

Prior to all machining experiments, beam characterization measurements were carried out. First the beam spectrum was measured to ensure the centre wavelength was set near 800 nm. Typically, the spectrum was centred at 800 nm with a full-width at half-maximum (FWHM) of approximately 20 nm. Next, the pulse duration was measured using an intensity autocorrelator. The beam profile was then measured after the objective lens using a CCD profiler. Next, a power calibration of the neutral density filters and the corresponding photodiode signal was carried out. A power meter was placed below the focal point of the objective and an AR-coated window and cover slip were placed in the beam path to account for reflections upon entry to the vacuum chamber. The power meter measured the average power of the beam. To determine the energy per pulse, the measured power (J/s) was divided by the repetition rate (1 kHz), giving the relationship 1 mW = 1 μJ/pulse. The beam power with no neutral density filters was then set to 20 μJ per pulse by rotating the HWP. The beam power and photodiode signal were recorded for filters up to optical density 2.0. Typical parameters for each of these measurements are shown in Figure 5-3.

Once this calibration was complete, the sample was placed on the stage in the vacuum chamber. The camera was focussed on the sample surface and the sample was aligned with the axes of the translation stages, so machining could be aligned with the major crystal axes. The vacuum chamber lid was put in place and the pump turned on. To shield against x-rays that may be generated at high fluences, the chamber was made of stainless steel, and a stainless steel sleeve was places around the objective, shielding the window of the chamber lid. Leaded glass was also placed between the chamber and computer workstation.

(a)

(b)

(c)

(d)
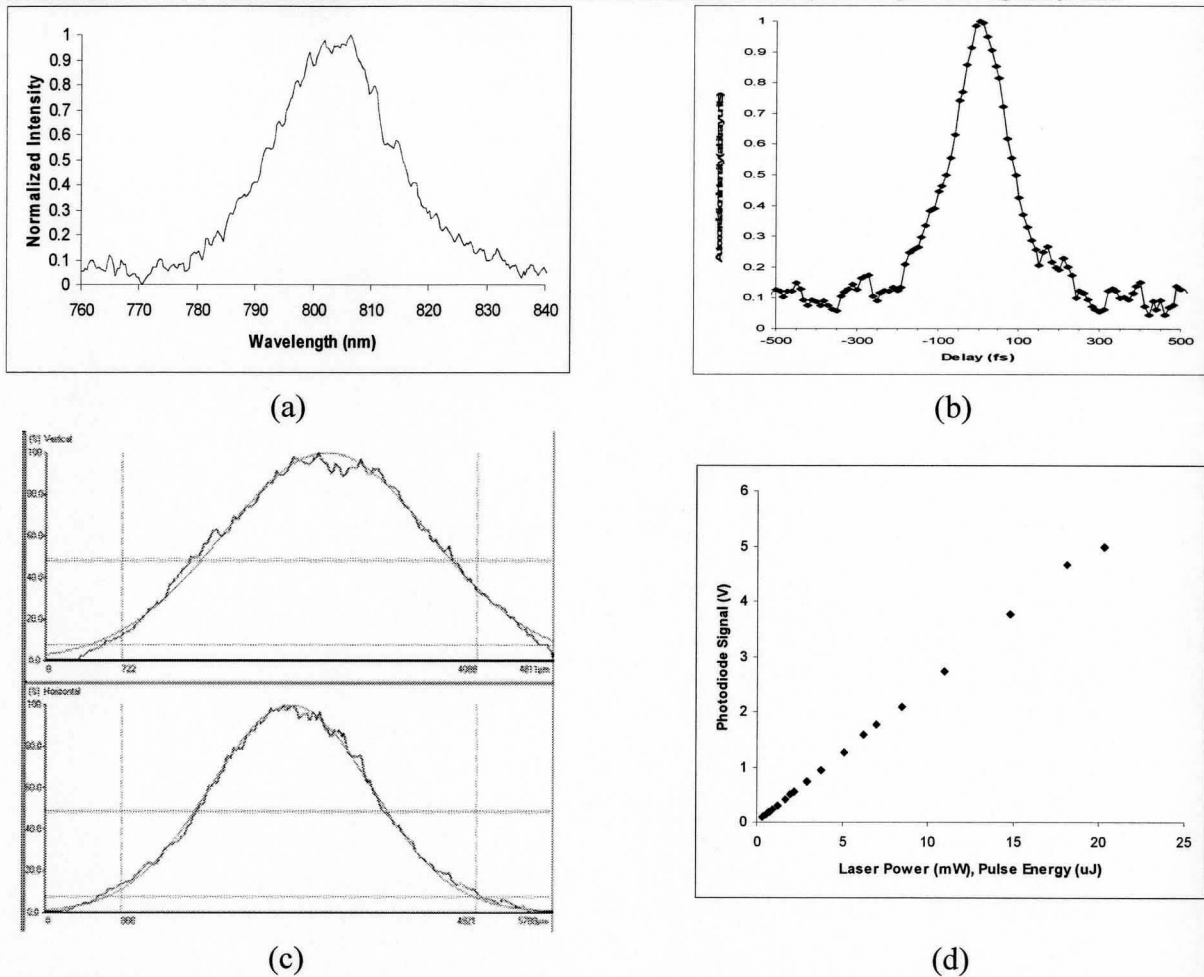
Figure 5-3: A typical (a) spectrum, (b) (c) beam profile and (d) photodiode calibration

It was desired to have the femtosecond beam focussed at the sample surface as well as the CCD camera. This was accomplished using the following procedure. The camera was focussed on the sample surface and the machining setup was programmed to continuously machine a series of parallel grooves. The sample height was adjusted so that laser was visibly damaging the surface. The sample was then lowered relative to the focus of the beam until damage was no longer occurring and raised once more until the point where the surface was once again being damaged. At this point, the sample surface is below the focal point of the beam but close enough that the laser fluence (energy delivered per unit area) was high enough to damage the surface. The camera focus was adjusted so the sample surface was in focus. The pulse energy was then decreased (a neutral density filter was added) and the process repeated. The lower fluence means that the sample surface must be even closer to the focal point for damage to occur.

Several iterations were carried out until the maximum laser fluence was below the damage threshold of the sample (i.e. no visible damage occurred). The sample surface was then as close as possible to the focal point of the beam and the camera was simultaneously focussed on the sample surface. From this point forward, the beam was assumed focussed on the sample surface if the image on the monitor was in focus.

5.2 Lithium Niobate Sample Preparation and Analysis

The lithium niobate crystals used in this work were supplied by Crystal Technology. Three types of wafers were used: x-cut (99-00630-01), y-cut (99-30002-01) and z-cut (99-60011-01). The x- and z-cut wafers were 1000 µm thick and double-side polished. The y-cut wafer was 500 µm thick and single-side polished. All wafers were three inches in diameter.

For machining purposes, only small samples were required. Unlike many semiconductors, lithium niobate cannot be easily cleaved. Instead, a precision wafer dicing saw (Loadpoint Ltd. MicroAce 3) with diamond blades was used to cut the wafers into 1 x 2 cm pieces. Resin-bonded diamond dicing blades from Thermocarbon, Inc. were used (2.187-8A-30RU7-3, 2.050-3A-30RU7-3). For the x- and z-cut wafers a large diameter, wide-kerf blade (2.187 inches, 0.0110 inches) was used to cut 700 µm into the wafer. For the y-cut wafer, a smaller blade was used (diameter 2.050 inches, kerf 0.003 inches) for a cutting depth of 400 µm. The blade rotation rate and translation speed of the sample relative to the blade affect the quality of the cuts. The goal is to cut with minimal chipping at the cut edge and no sample cracking. Rotation at 18000 rpm and translation at 1000 µm/s gave good results; so further polishing of facets is not required. Faster rotation and slower translation also work well. The cuts do not penetrate the entire sample surface to avoid saw and blade damage. This procedure is used for wafer dicing, cross sectioning of laser-machined grooves and in the creation of 'slices' of grooves cross-sections, which are used for transmission electron microscope (TEM) imaging.

Before cutting, the samples are placed on thin tape that is then mounted to the saw. After cutting, the sample pieces can be gently broken apart by hand along the cut line and left on the tape for later use (in the case of wafer dicing) or separated and removed from the tape for examination (in the case of groove cross-sectioning).

Subsequent to laser machining, the samples were cleaned in an ultrasonic bath using acetone, followed by methanol, and then dried with compressed air or nitrogen. Samples were cross-sectioned (if necessary) and imaged using an optical microscope (Zeiss), with polarized light and in some cases Nomarski contrast. Following optical imaging, samples were sputter-coated with gold for scanning electron microscope (SEM)

imaging. For one experiment involving grooves, the sample was cut into 1mm strips, thinned by polishing and then ion-milled for TEM imaging, according to the instructions of the lab technician. Measurements were performed using commercial imaging software.

5.3 Summary

The laser system used in these experiments consisted of a Ti:sapphire oscillator followed by a chirped-pulse amplifier. The peak pulse energy can be controlled using a half-wave plate and a polarizer and decrease incrementally using a series of neutral density filters. Pulse power could be continuously monitored via a beam splitter and photodiode. Prior to all experiments, the beam was aligned and the profile, pulse duration and beam power were measured. A fast mechanical shutter and an optical chopper allowed control of the number of pulses reaching the sample. The beam was focussed with a long working-distance 5x objective lens and the sample was in a vacuum chamber that was moved relative to the beam using precision linear translation stages. A confocal viewing system was used and the set-up was largely computer controlled. X-, y- and z-cut lithium niobate samples from Crystal Technology were used. Samples were cut using a precision dicing saw with diamond-tipped blades. Sample analysis consisted of polarized light microscopy followed by SEM or TEM imaging. SEM samples were sputter-coated with gold. TEM samples were thinned by polishing and ion milling. Measurements were taken using imaging software. The results for several samples prepared in this manner are presented (finally!) in Chapter 6.

Chapter 6 Laser Micromachining of Lithium Niobate

Lithium niobate is a well-studied ferroelectric compound with a strong electro-optic effect. These properties give it the potential to find applications in MEMS. However, there is currently no viable method for creating MEMS structures in this material. Femtosecond lasers have been used successfully in the machining of other materials due to the small heat-affected zone that is created. Laser ablation of lithium niobate has been studied previously, but usually in the context of sputtering thin films. Very little has been done in the femtosecond regime. In this chapter, results of femtosecond laser micromachining experiments are presented.

Section 6.1 covers single- and multiple-pulse experiments, where crater morphology is examined and the ablation thresholds and incubation coefficients are determined for the three crystal orientations and various laser polarizations. Section 6.2 discusses the machining of grooves. Characterization of groove morphology and depth as a function of pulse fluence and cutting speed are presented. The effects of crystal orientation, laser polarization with respect to the cutting direction and number of consecutive passes are examined. Most notably, when attempting to cut grooves, at fast cutting speeds there is excellent ablation, whereas at slower speeds channels of amorphous material are created with very little apparent material removal. Reasons for this are suggested. Finally, the mechanisms for absorption and incubation are discussed.

Each of the above sections are divided into two subsections: Results, where the images, graphs and fitting equations are presented, and Discussion, where the current results are compared to results from the literature and the observed phenomena are explained. The results are presented as clearly and concisely as possible, although there are many images and plots.

6.1 Single and Multiple Pulse Ablation

The first experiments involved single- and multiple-pulse irradiation in order to observe the crater morphology and determine the ablation thresholds and incubation factors for x-, y- and z-cut lithium niobate. On each sample, three 6 x 20 arrays of craters was created, with the six rows corresponding to different numbers of pulses (N=1, 5, 10, 20, 50, 100) and the twenty columns corresponding to different pulse energies with a maximum of 20 µJ and attenuated with a sequence of neutral density filters (OD=0.0 to

1.9, in increments of 0.1). The spacing between crater centres was 50 μm. The three arrays on each sample corresponded to different laser polarizations. One array was created using circular polarization. The other two arrays were created using linear polarization parallel to the two crystal axes in the plane of the sample surface (i.e. on an x-cut sample: parallel to z and parallel to y). The repetition rate for multiple pulses was 50 Hz.

6.1.1 Results

Figure 6-1 shows craters on each sample with varying pulse energy. The crater morphology is similar for each crystal orientation. The highest pulse energies result in cracks within the crater boundary and some splattering of now-frozen liquid material. A decrease in pulse energy decreases both effects. With pulse energy below 3 μJ, no cracking is observed. Elliptical craters can be attributed to an asymmetrical beam profile and are likely not due to the crystal orientation.

Figure 6-2 and Figure 6-3 show craters on each sample with an increasing number of pulses N. Each crater was created at a different location on the sample surface. The resulting crater morphologies depend on the pulse energy used. For the higher pulse energy used for Figure 6-2, the crater bottom and walls remain smooth. With increasing N, there is an increase in diameter, the creation of a 'rim' along with significant splattering and cracking. At the lower pulse energy used for   Figure 6-3, there are sub-micron-sized pits on the crater bottoms. In the 5-pulse case there is also a circular pattern. The crater walls are also quite rough. However, there is very little surface debris and no cracking even at 100 pulses.

Figure 6-4 shows craters on each sample with 10 pulses and three different laser polarizations. In certain cases, the pattern on the crater bottom appears to depend on the laser polarization. For linear polarization, ripples are formed parallel to the polarization of the laser beam. These ripples are most apparent when between 2 and 20 pulses are used with energy per pulse less than 2.5 μJ. For the x- and y-cut samples the ripple period is approximately 800 nm. The ripple period for the z-cut sample was approximately 900 nm. For each crystal orientation, using circular polarization, there is no distinct periodic pattern, although there appears to be some regularity to the structure, perhaps due to the combination of perpendicular linear polarizations.

Figure 6-5 shows a plot of single-pulse crater diameter squared as a function of pulse energy for the y-cut sample. No dependence of crater size on laser polarization is observed.

Pulse Fluence (J/cm^2)	X-cut	Y-cut	Z-cut
49			
27			
13			
5			
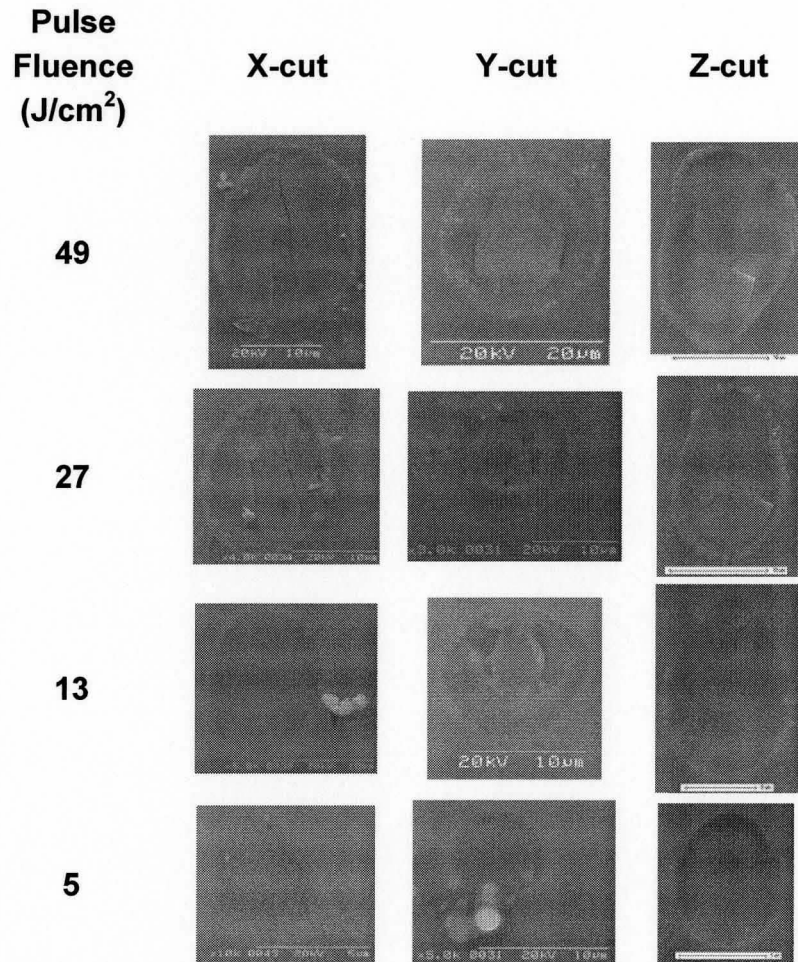
Figure 6-1: SEM images of single-pulse ablation craters made using varying pulse energies and circularly polarized light. Note the scale on each image.

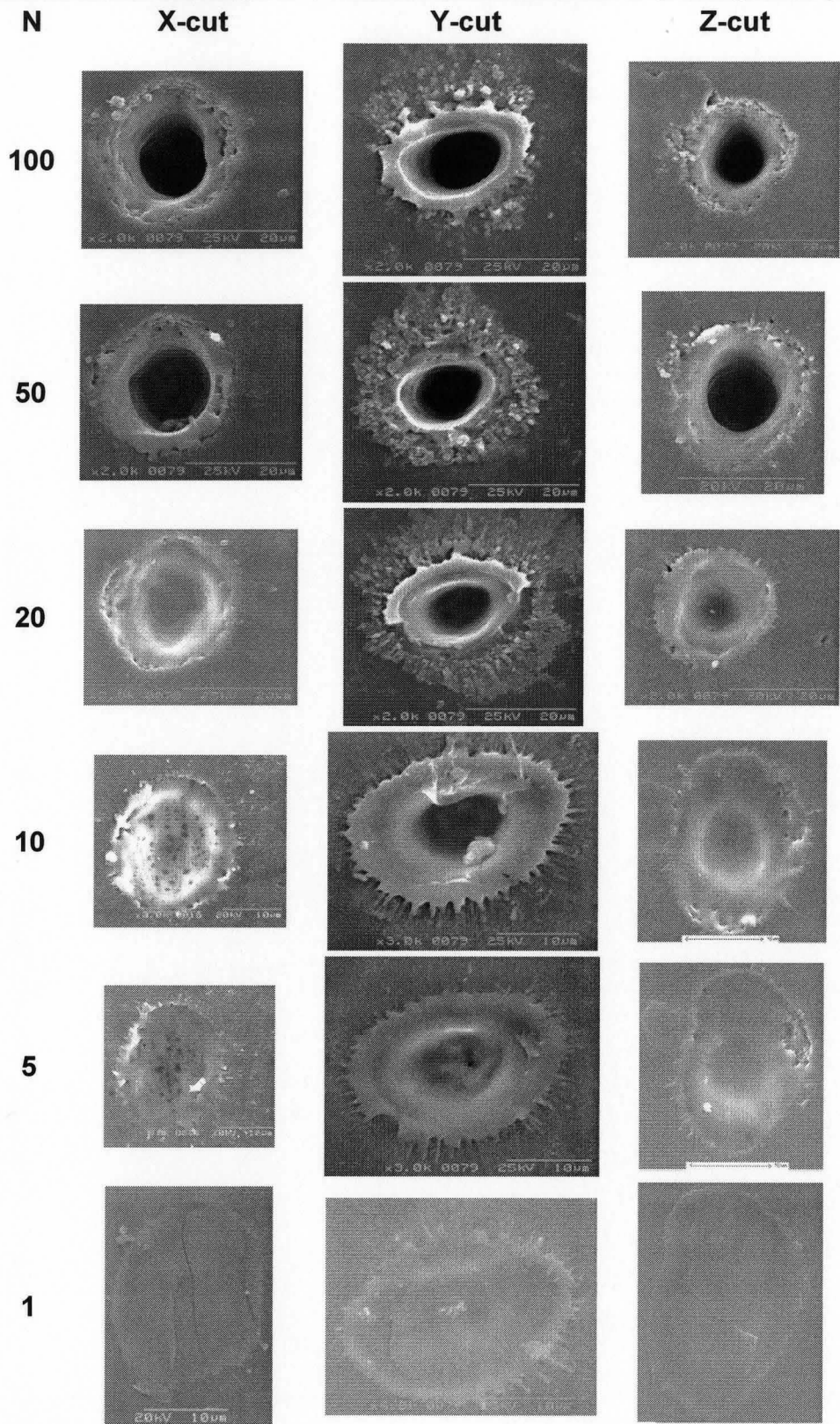| N	X-cut	Y-cut	Z-cut
100			
50			
20			
10			
5			
1			

Figure 6-2: SEM images of ablation craters using circularly polarized light, 20 μJ/pulse (49 J/cm^2), and varying number of pulses/crater. Note the image scales.

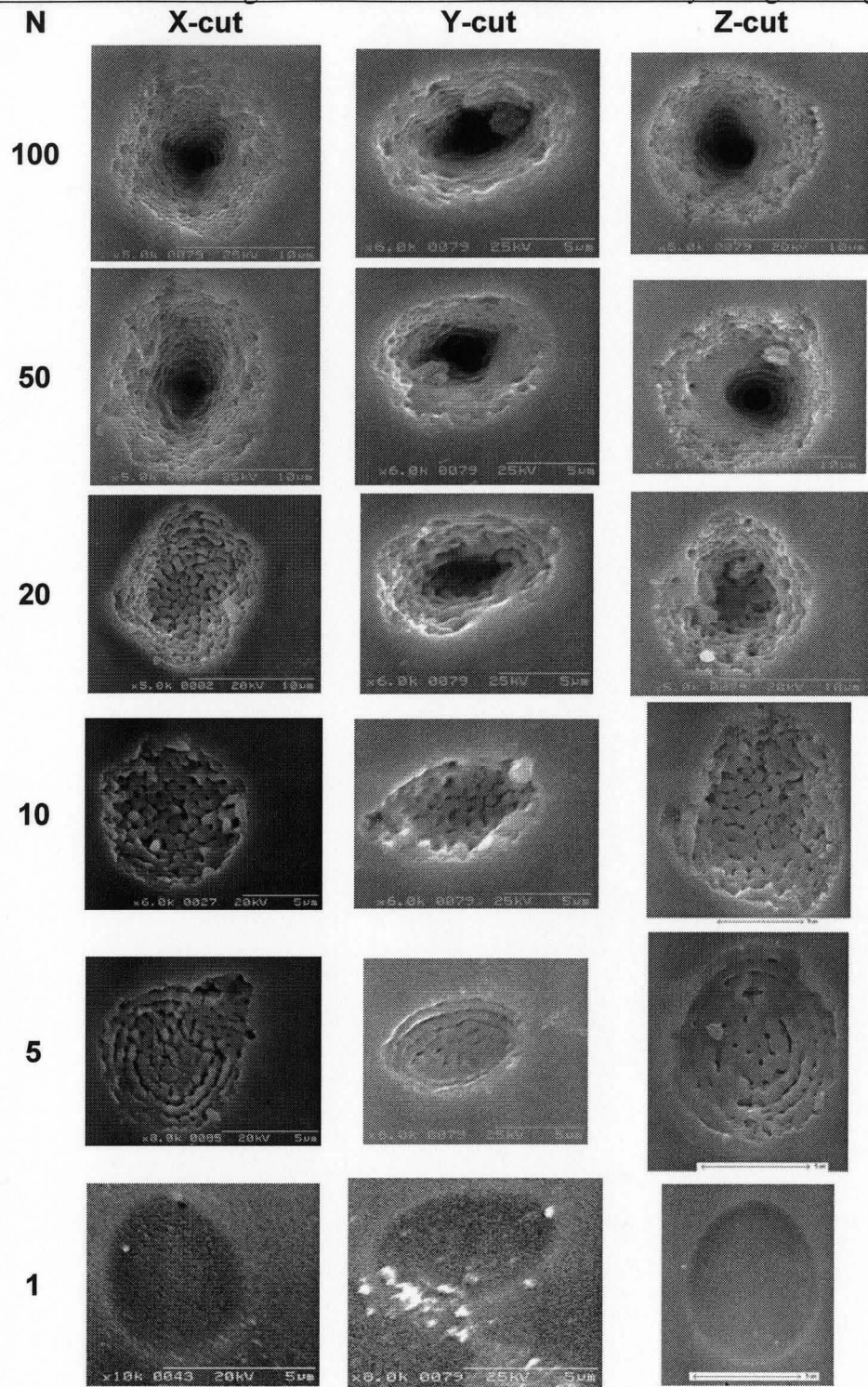| N	X-cut	Y-cut	Z-cut
100			
50			
20			
10			
5			
1			

Figure 6-3: SEM images similar to those of Figure 6-2, using 1.0 µJ/pulse (2.1 J/cm^2).

Polarization	X-cut	Y-cut	Z-cut

(a) Circular
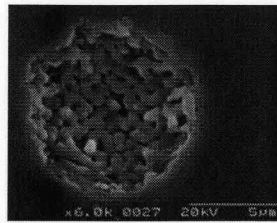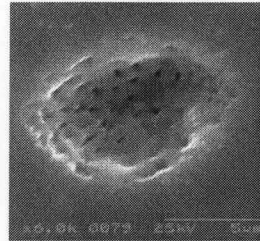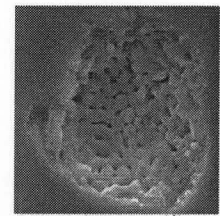
y-axis→   x-axis→   x-axis →

(b) Linear 1
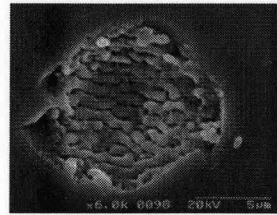
Polarization Parallel to Y   Pol. Parallel to X   Pol. Parallel to X
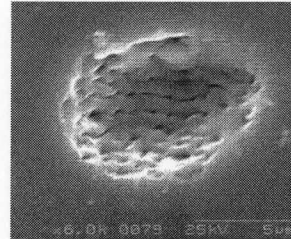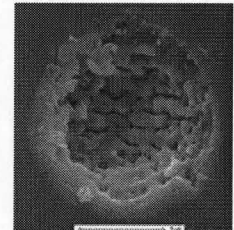
(c) Linear 2
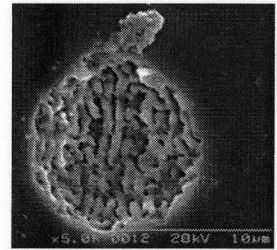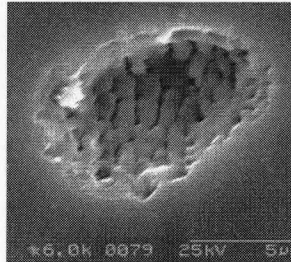
Pol. Parallel to Z   Pol. Parallel to Z   Pol. Parallel to Y
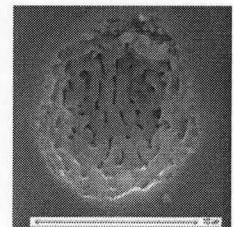
Figure 6-4: SEM images of 10-pulse ablation using (a) circular polarization, (b) and (c) linear polarization parallel to the crystal axes in the sample surface plane. The direction of a second crystal axis is shown below the images in (a). The direction of laser polarization is shown below the images in (b) and (c).
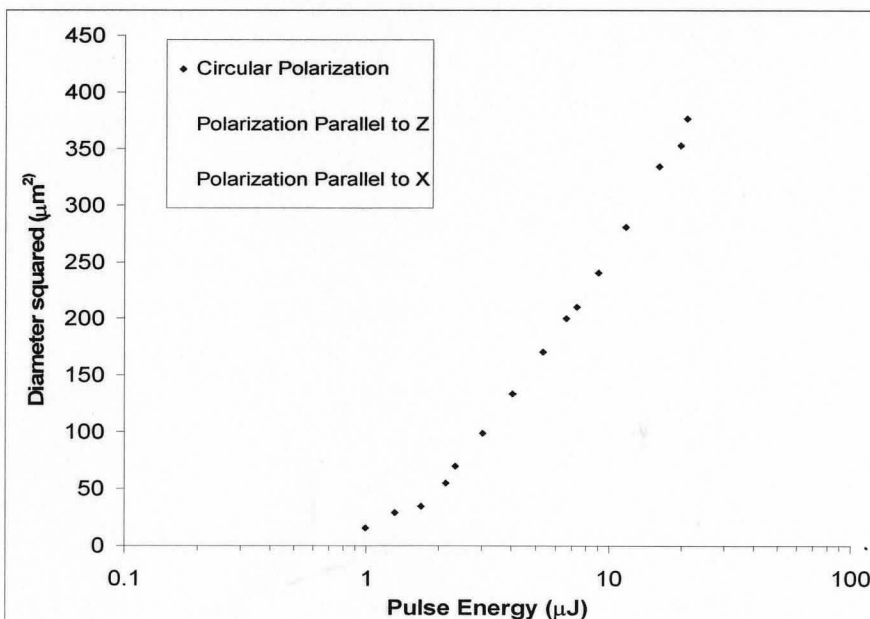
Figure 6-5: Crater diameter dependence on pulse fluence of a y-cut sample for (a) single pulse ablation, all polarizations

Equation 4-2 suggests that the data should give a straight line on a semi-log plot when the beam profile is assumed Gaussian. This does not appear to be the case for higher pulse energies, as the crater diameters show a greater increase with higher pulse energies. Two ablation regimes, called gentle and strong, have been observed previously in dielectrics [44] and are attributed to a transition from vaporization to explosive boiling [45]. This could be the case for lithium niobate as well, since ablation is well defined at lower energies and appears less controlled at higher energies with evidence of explosive liquid deposition, as seen in Figure 6-2. However, the deviation could also be due to the beam profile.

To investigate this second possibility, single pulse ablation experiments were performed on a silicon sample. Figure 6-6 (a) shows the diameter-squared dependence on pulse energy results. In this case, there appear to be two regimes for silicon as well, with the transition in regimes occurring in the 2 to 6 μJ range.

A comparison of the measured beam profile and a Gaussian profile was then made, as illustrated in Figure 6-6 (b). From the image, it is clear that a single Gaussian cannot approximate the entire beam profile. A better approximation involves one Gaussian to fit the peak of the curve and a different Gaussian to fit the tails of the curve. From Figure 6-6 (a) it also appears as though two different Gaussian beam profiles may have caused the ablation, since there appear to be two straight line portions. This data can yield what those two Gaussians are and if they match the two Gaussians of the measured profile, then the change in slope is due to the beam profile.

Equation 6-1 can be fit to the two straight line portions of Figure 6-6 (a). This yields $\omega_{0,lower} = 5.5$ μm, $E_{th} = 0.23$ μJ and $\omega_{0,upper} = 9.2$ μm, $E_{th} = 1.2$ μJ. For a given Gaussian profile, the peak fluence can be determined using Equation 6-2. Given the peak fluence and ω_0, the beam profile can be calculated by Equation 6-3 [46]. The threshold fluence for the lower region is 0.49 ± 0.30 J/cm^2, in agreement with at least one other published value [47].

For the upper portion to cause ablation, energy of 1.2 μJ is required, giving the amplitude of Equation 6-4. When this energy is used to plot the profile for the lower regime, the amplitude of Equation 6-5 is obtained, giving an amplitude ratio of 0.29 (Equation 6-6). The two Gaussians are plotted to scale in Figure 6-6 (c), with the higher peak normalized.

$$d^2 = 2\omega_o^2 \ln\left(\frac{E}{E_{th}}\right) \qquad \text{6-1}$$

$$F_o = \frac{2E}{\pi\omega_o^2} \qquad \text{6-2}$$

$$F(r) = F_o \exp\left(\frac{-2r^2}{\omega_o^2}\right) \qquad \text{6-3}$$

$$F_{o,upper} = \frac{2E_{th,upper}}{\pi\omega_{o,upper}^2} \qquad \text{6-4}$$

$$F_{o,lower} = \frac{2E_{th,upper}}{\pi\omega_{o,lower}^2} \qquad \text{6-5}$$

$$\frac{F_{o,upper}}{F_{o,lower}} = \frac{2E_{th,upper}}{\pi\omega_{o,upper}^2} \cdot \frac{\pi\omega_{o,lower}^2}{2E_{th,upper}} = \frac{\omega_{o,lower}^2}{\omega_{o,upper}^2} = 0.29 \qquad \text{6-6}$$

The measured beam profile gives for the two Gaussians an amplitude ratio of 0.9 (Figure 6-6 (b)). This indicates that the beam profile gives $E_{th,upper}$ = 0.26 µJ, which is much lower than the observed $E_{th,upper}$ = 1.26 µJ, so it is unlikely that the beam shape alone is the source of the change in slope.

To summarize, lithium niobate does not follow 4-2 (6-1) over the entire energy range used for the experiments that were performed. There appears to be a threshold above which the rate of increase of the crater diameter increases (Figure 6-6 (a)). The deviation could be caused by the presence of gentle and strong ablation regimes or by the beam profile, which is approximated by two Gaussians (Figure 6-6 (b)). The ablation data for silicon showed that the change in slope in Figure 6-6 (a) occurs at a much higher energy than the beam profile predicts (Figure 6-6 (b)). So, the likely explanation is that there are two ablation regimes. The transition from gentle to strong ablation over several experiments occurs somewhere between 2 and 10 µJ/pulse (5 to 24 J/cm^2). Two ablation regimes were also observed in the machining of grooves, as will be presented in the next sections. The transition in the case of grooves occurs near 20 J/cm^2. The immediate consequence is that the in determining the ablation thresholds of lithium niobate, only the lower energy regime will be used.
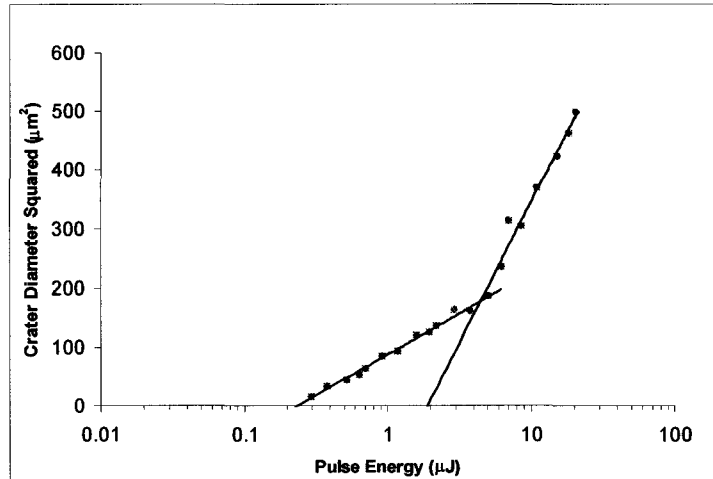
(a)
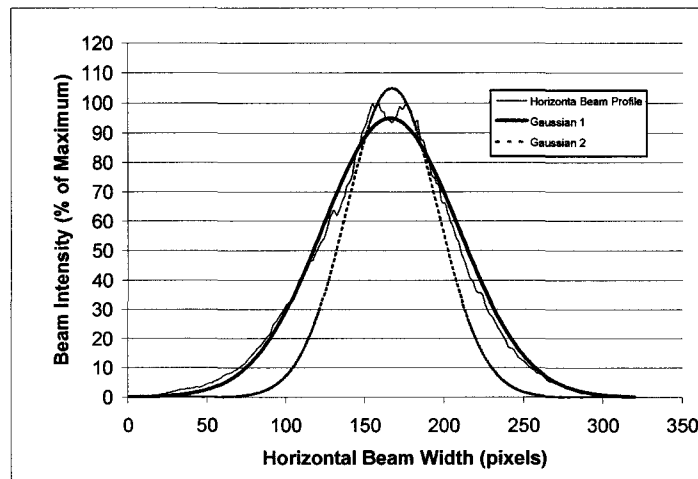
(b)
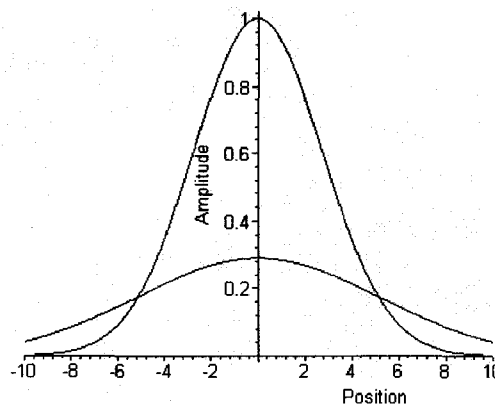
(c)

Figure 6-6: Single-pulse ablation of silicon: (a) diameter dependence on pulse fluence (b) beam profile approximated by two Gaussians and (c) Two Gaussians obtained from (a). The beam profile in (b) suggests that the shift should occur at a lower energy than it actually does. This means that the beam profile alone does not account for the change in slope, so gentle and strong ablation likely play a role.
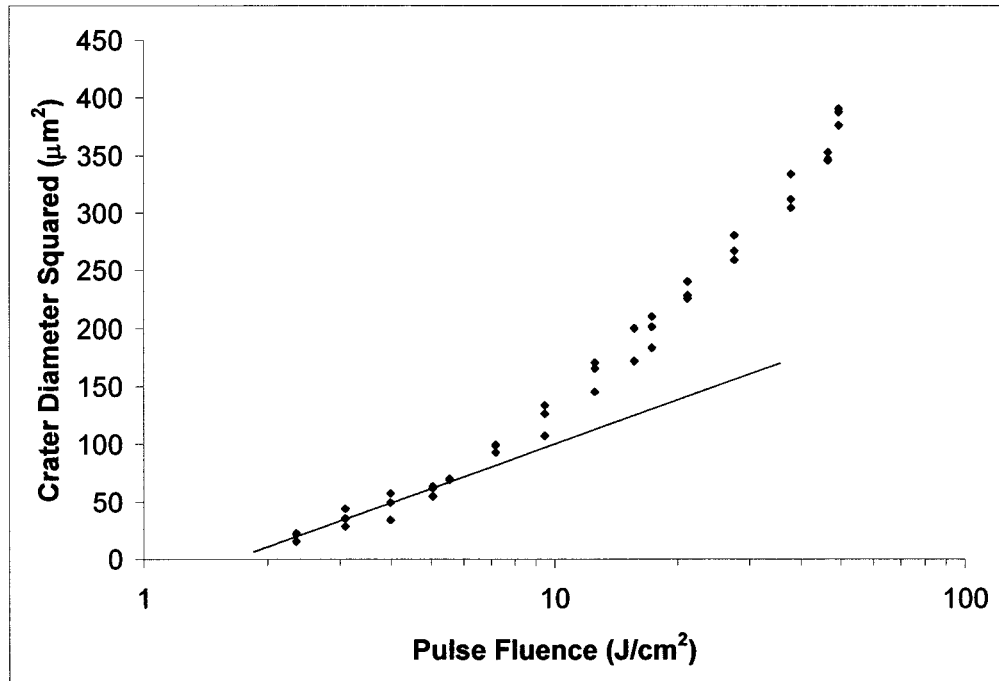
(a)
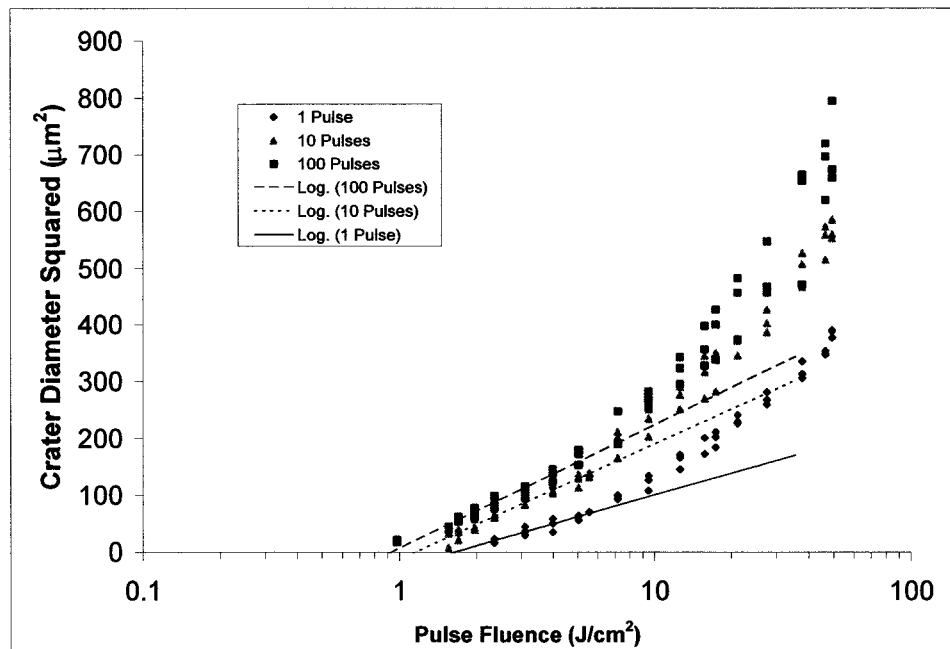
(b)

Figure 6-7: A least-squares fit to the lower-energy craters on a y-cut sample (a) Single Pulses (b) Multiple Pulses

A least-squares fit to the lower-energy data from all polarizations on a y-cut sample, shown in Figure 6-7 (a), gives an ablation threshold of 1.6 ± 0.2 J/cm^2 and a laser spot size of 5.2 ± 0.2 µm. Figure 6-7 (b) shows the same plot but also includes the data

for 10 and 100 pulses. The same two-regime behaviour was observed for multi-pulse ablation. Fits to the lower energy data show a decrease in the ablation threshold with increasing number of pulses, as illustrated in Figure 6-8, which shows accumulated fluence at the ablation threshold. A fit to Equation 4-5 yields an incubation factor of $\xi = 0.74 \pm 0.05$.

Analysis of the other crystal orientations yielded similar results. The x-cut and z-cut ablation thresholds were 1.3 ± 0.1 J/cm^2 and 1.5 ± 0.2 J/cm^2, respectively. The incubation factors were 0.76 ± 0.03 and 0.74 ± 0.04. The uncertainties in all of the calculations were determined purely from the uncertainties of the fits. Within their respective uncertainties, the single pulse ablation thresholds and incubation factors for each crystal orientation are in agreement, so there is no discernable difference. Averaging over the three orientations gives a threshold of 1.5 ± 0.2 J/cm^2 and incubation factor of 0.75 ± 0.07.
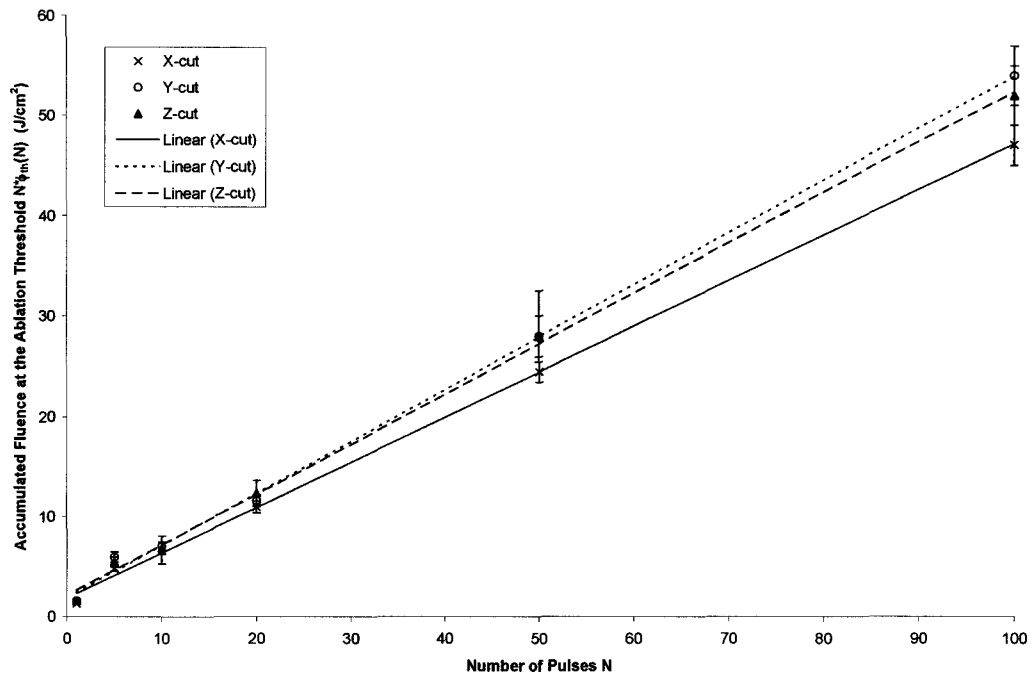
Figure 6-8: Accumulated fluence at the ablation threshold for multi-pulse ablation

6.1.2 Discussion

Single and multiple pulses were used to irradiate stationary samples. All three major crystal orientations were examined, as were three different polarization orientations (linear and perpendicular to the two axes in the sample plane, as well as circular). The ablation thresholds were determined, as well as incubation coefficients.

These quantities did not depend on crystal orientation or laser polarization. However, in some cases ripples were observed on the crater bottom, which did appear to depend on the polarization orientation.

For single-pulse ablation, the threshold of 1.5 J/cm^2 is somewhat less than the value of 2.5 J/cm^2 reported by Deshpande [42]. A threshold of 0.63 J/cm^2 was also reported [49], though no explanation of the calculation was given. Deshpande used a pulse duration of 300 fs whereas 150 fs pulses were used in this work, giving a ratio of $\phi_{th}(150\,fs)/\,\phi_{th}(300\,fs) = 0.60$. A decrease in ablation threshold with pulse duration has been reported in barium aluminium borosilicate glass (a commonly studied dielectric when it comes to femtosecond ablation, with a bandgap close to that of lithium niobate), with a ratio of $\phi_{th}(120\,fs)/\,\phi_{th}(300\,fs) = 0.70$ in the thresholds [48]. Assuming that the pulse duration measurements are accurate, the value obtained here is not entirely unexpected. This decrease in single-pulse ablation threshold is due to the increased pulse intensity for shorter pulses, which increases the likelihood that multi-photon ionization will excite seed electrons for avalanche ionization [24].

Deshpande also reports a 5-pulse ablation threshold of 1 J/cm^2, in agreement with the value obtained from the present experiments of 1.1 ± 0.2 J/cm^2. The decrease in ablation threshold indicates that the material absorption coefficient is increased, although no visible damage is apparent until the fifth pulse. This decrease also suggests that the 5-pulse threshold becomes independent of pulse duration. This will be discussed further later on, when the absorption mechanism is addressed.

There was no apparent dependence of ablation threshold or crater size and shape on laser polarization or crystal orientation. This is an interesting result, since lithium niobate is ferroelectric and one may expect nonlinear effects to play a role in the ablation process.

Both gentle and strong ablation regimes seem to be present, since the higher energy pulses result in crater rims that appear to have been created by an explosive removal of liquid material. The transition from gentle to strong ablation occurs between 5 and 24 J/cm^2. This phenomenon has been reported in lithium niobate, though also with no precise determination of the transition [49]. The existence of two-regimes is usually determined using depth profiles, whereas diameters were used to determine the threshold in these experiments. Ideally, depths would be measured as well, although this proved difficult since the craters were too deep for atomic-force microscopy and an optical profilometer lacked a sufficient objective lens.

The circular pattern observed for 5-pulse irradiation due to multiple pulses, only visible for 5-pulse irradiation in Figure 6-3, is likely due to the incubation. The first pulse will only ablate a portion of the sample that is nearest the centre of the beam profile, where the intensity is highest. A region surrounding the initial crater will be modified but not ablated. The second pulse will ablate the centre region again, and initiate ablation in the surrounding region, resulting in a crater with a subsurface rim. The region surrounding the new crater will also be modified but not ablated. The third pulse will ablate the centre region and rim further, as well as the surrounding region, resulting in a three-tiered crater. This process will repeat for only a few pulses. After ablation occurs across the entire beam, the tiers will begin to vanish as the crater deepens with further pulses. This appears to be the case, as seen in the images of 10, 20 50 and 100-pulse craters in Figure 6-3.

The ripple formation observed on the crater bottoms is an interesting phenomenon. Ripples have been previously observed in the femtosecond ablation of dielectrics [24, 44] and lithium niobate [49]. While a complete description of ripple formation is beyond the scope of this thesis, early explanations attributed ripple formation to the interference of light scattered from imperfections on the material surface with the incident beam, resulting in a periodic, non-uniform energy distribution across the irradiated region. At normal incidence and with a linear imperfection present, ripples would be perpendicular to the polarization of the beam with spacing equal to the wavelength of the light. However, many observations of ripples that do not conform to this theory have been made. Ripples with periodicity much less than the wavelength of the light [50] and that depends on the intensity [51] and repetition [52] rate of the pulsed have been observed. It has been proposed that the post-irradiation relaxation of the surface involves material self-organization [24, 50, 51, 52], although the mechanism by which these ripples are far from being understood.

The 'classical' explanation of ripple formation [53, 54] in lithium niobate is given by Kitano [49] and cannot be entirely ruled out in the current experiments since the period is quite close to the laser wavelength and for circularly polarized light no ripples were observed. However, many of the ripples do qualitatively resemble those reported by Seifert et al [52] in both the irregularities and the alignment of the ripples parallel to the laser polarization. The ripples are attributed to the relaxation of surface liquid within a temperature gradient in the presence of the laser electric field. This could be a plausible explanation for the ripples in lithium niobate. Liquid material is clearly formed in the ablation process as in Figure 6-2 where the crater bottom appears to be covered with a smooth layer of frozen liquid at the lower numbers of pulses and liquid spills over the crater edge at larger numbers of pulses. Further experimentation would give deeper

insight into both the optimal conditions for ripple formation as well as the mechanism behind their formation.

6.2 Micromachining of Grooves in Lithium Niobate

In addition to single and multiple-pulse experiments, micromachining of grooves in lithium niobate was also studied. The first grooves were machined using a single pass of the laser beam over the sample surface in sets corresponding to different translation speeds of the sample relative to the beam. Speeds of 1000, 750, 500, 250, 100, 75 and 50 µm/s were used. In each set, 15 grooves were created using decreasing pulse energy. Again, the effects of laser polarization and crystal orientation were examined. Next, trenches were machined using multiple consecutive passes over the same groove. The pulse repetition rate for grooves was 1000 Hz.

6.2.1 Results

6.2.1.1   Groove Morphologies

Beginning with the y-cut sample, grooves were machined parallel to the z-axis of the crystal with laser polarization perpendicular to the cutting direction. A variety of groove morphologies were observed depending on the machining parameters. These are shown schematically in Figure 6-9, with micrographs in Figure 6-10, Figure 6-11 and Figure 6-12.
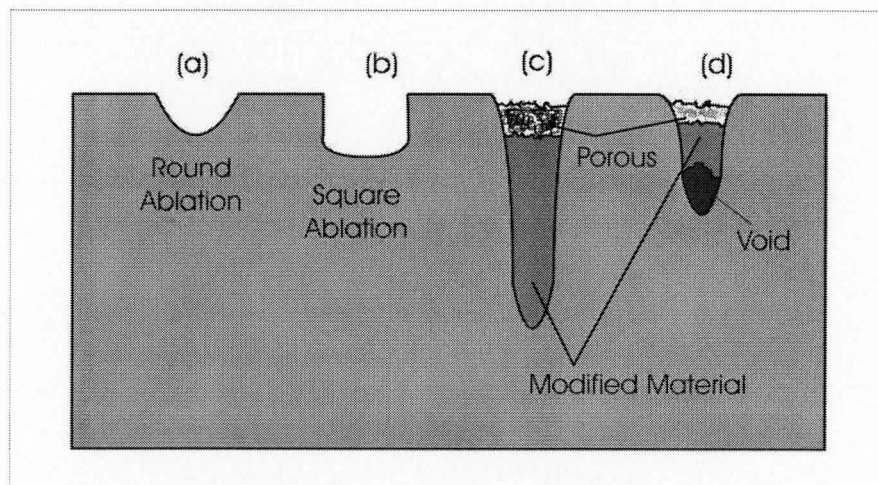
**Figure 6-9: Schematic of observed groove morphologies (a) round ablation (b) square ablation (c) subsurface modification with no void (d) subsurface modification with a void**

Many of the grooves clearly have a rounded bottom with no damage in the surrounding material (Figure 6-9 (a) and Figure 6-10(a)). Some of the grooves have vertical side-walls and a flat bottom. This is labelled 'square ablation' (Figure 6-9 (b)

and Figure 6-10 (c)). A few of the grooves appear to be transitional, between round and square ablation (Figure 6-10 (b)).

Entirely different groove morphologies were also observed, where ablation was minimal but there was a significant amount of material modification well below the sample surface (Figure 6-9 (c)). This is shown in the optical micrograph of Figure 6-11(a). The modification is more evident when crossed polarizers are in the light path (Figure 6-11 (b)). On a few of the samples, the modification could be clearly seen as a dark region below the surface damage using the SEM when the contrast and brightness were adjusted appropriately (Figure 6-11 (c), (d)). There also appears to be material modification (light coloured) surrounding the dark 'groove,' where the laser did not directly irradiate the sample. However, with most samples the modification was not as clear in the SEM (Figure 6-11 (e)).

This deep modification exhibited different features, again depending on the machining parameters such as pulse energy and sample translation speed. These features are shown in Figure 6-12. In Figure 6-12 (a), the surface has been ablated. However, the grooves appear filled with 'porous' material. Beneath the porous region, there is deep modification, at the bottom of which is a void (Figure 6-9 (d)). As the pulse energy is decreased, the modified region decreases in size and the void merges with the porous region (Figure 6-12 (b)) and eventually becomes a hollow groove. In many cases there was no void at the bottom of the deep modification (Figure 6-12 (c)). Finally, in some cases there was only porous material at the surface with no damage below (Figure 6-12 (d)).

| (a) | (b) | (c) |
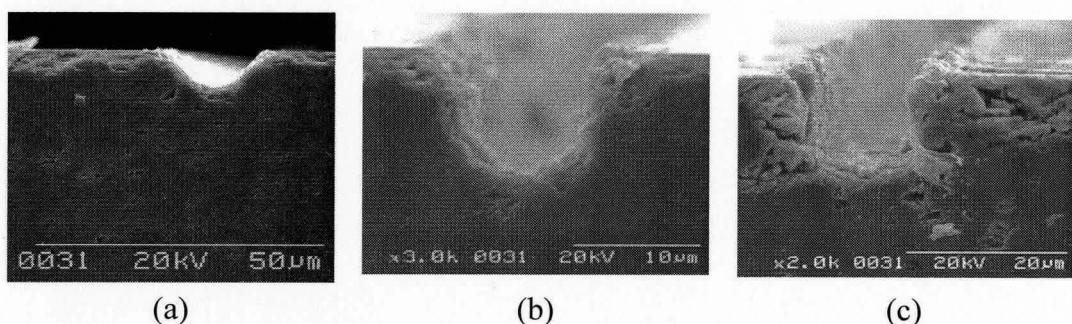
Figure 6-10: Ablation morphologies of grooves machined on a y-cut lithium niobate sample: (a) Round ablation—1000 µm/s, 24 J/cm^2, (b) Transitional, round to square—500 µm/s, 14.5 J/cm^2 and (c) Square ablation—750 µm/s, 52 J/cm^2.

(a)

(b)

(c)

(d)

(e)
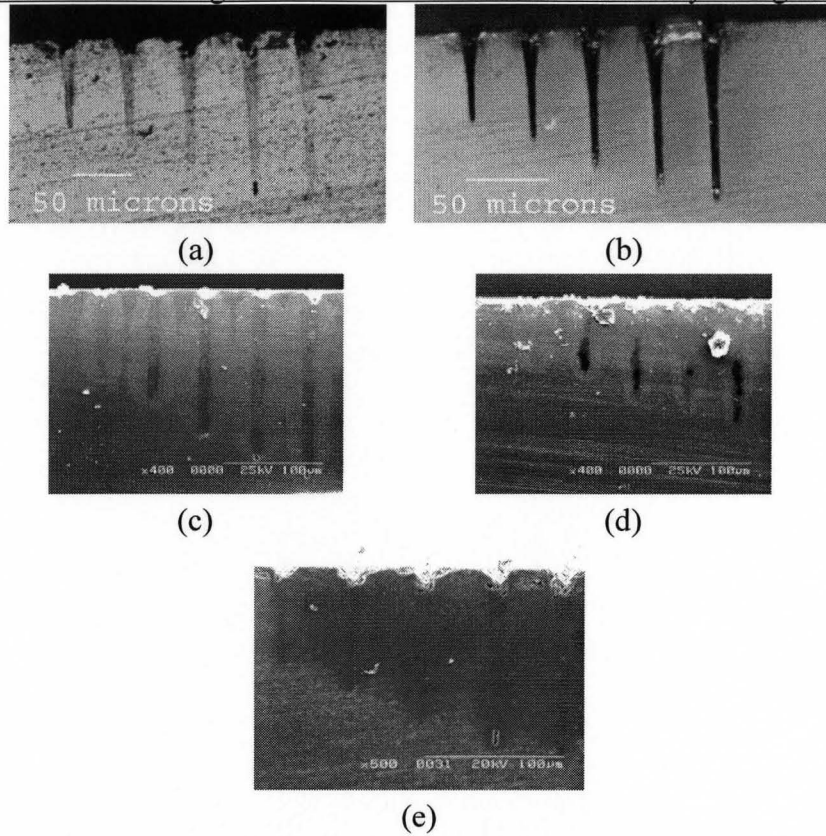
Figure 6-11: Subsurface modification in grooves machined on y-cut samples:
(a) Optical image with unpolarized light—50 μm/s—20, 26, 32, 40 and 51 J/cm^2
(b) Optical image with crossed polarizers in the light path—50 μm/s—20, 26, 32, 40
and 51 J/cm^2
(c) SEM image showing deep modification—10 μm/s—20, 26, 32, 40 and 51 J/cm^2
(d) SEM image showing deep modification—50 μm/s—20, 26, 32, 40 and 51 J/cm^2
(e) A more typical SEM image showing deep modification—50 μm/s—20, 26, 32, 40
and 51 J/cm^2
(a), (b) and (e) show the same sample. The contrast in the SEM images has been
digitally enhanced.

(a)

(b)

(c)

(d)
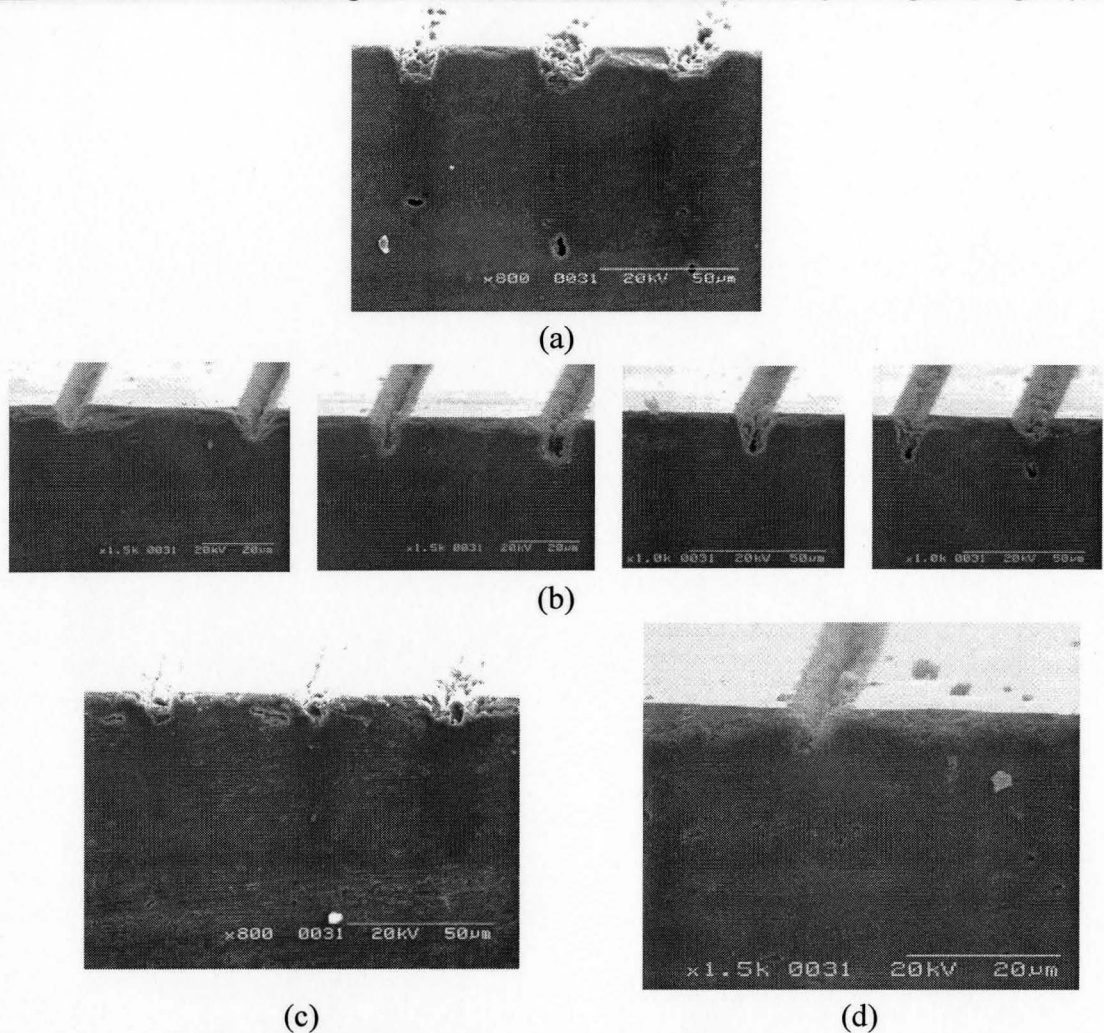
Figure 6-12: Subsurface modification in grooves machined on a y-cut sample:
(a) Groove filled with porous material, deep modification below and a void at the
bottom (Speed = 250 μm/s , Fluence = 32, 40 and 51 J/cm² (left to right))
(b) At lower pulse energies, void merges with porous material (Speed = 250 μm/s,
Fluence = 2.6, 3.2, 4.1, 5.1, 6.4, 8.1, 10.2 J/cm² (left to right))
(c) Porous material at surface, modification below, no void (Speed = 75 μm/s,
Fluence = 16, 12.8, 10.2 J/cm²)
(d) Porous material at surface—no damage below (Speed = 100 μm/s, Fluence = 2
**J/cm²)**

Experimental Phase Plots

A phase plot outlining the experimental conditions creating each of these morphologies is shown in Figure 6-13. When the fluence is plotted with a logarithmic scale as in Figure 6-13 (a), a boundary separating round ablation from the other morphologies can be defined. The line in the figure is a fit to the highest fluence at each translation speed for which clean, round ablation was observed and is defined by Equation 6-7, where F is the fluence, v is the translation speed and F_o and v_o are the fit parameters. The fit gives $F_o = 1.0 \pm 0.1$ J/cm^2 and $v_o = 241 \pm 11$ μm/s.

$$F = F_o e^{\frac{v}{v_o}} \quad \text{6-7} \qquad F = F_o e^{\frac{N_{eff,o}}{N_{eff}}} \quad \text{6-8}$$

When $F < F_o e^{\frac{v}{v_o}}$, there is ablation and when $F > F_o e^{\frac{v}{v_o}}$, there is sub-surface modification for $v<v_o$. For $F > F_o e^{\frac{v}{v_o}}$ when $v>v_o$ there is square ablation and subsurface modification with a void at the bottom. The equivalent boundary using an effective number of pulses as in Equation 4-6 is given by Equation 6-8, where $N_{eff, o} = 26 \pm 1$. The corresponding inequalities are $F < F_o e^{\frac{N_{eff,o}}{N_{eff}}}$ for ablation and $F > F_o e^{\frac{N_{eff,o}}{N_{eff}}}$ otherwise. The equivalent plot is shown in Figure 6-13 (b).
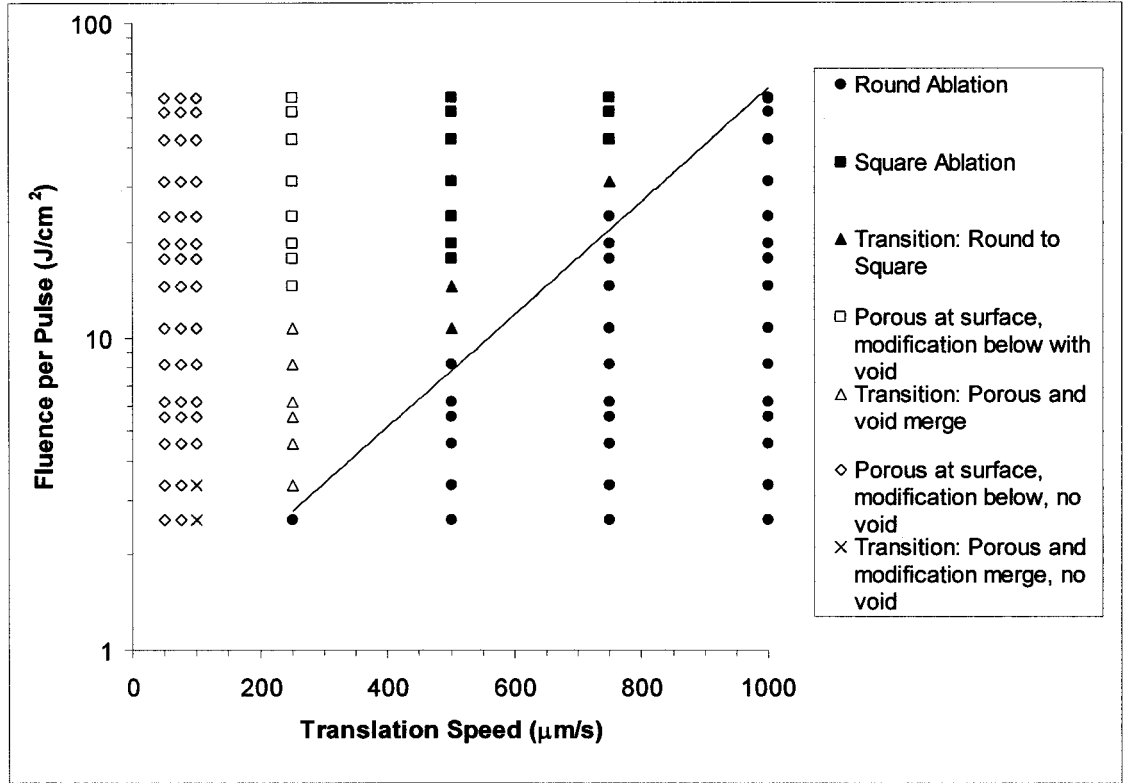
(a)
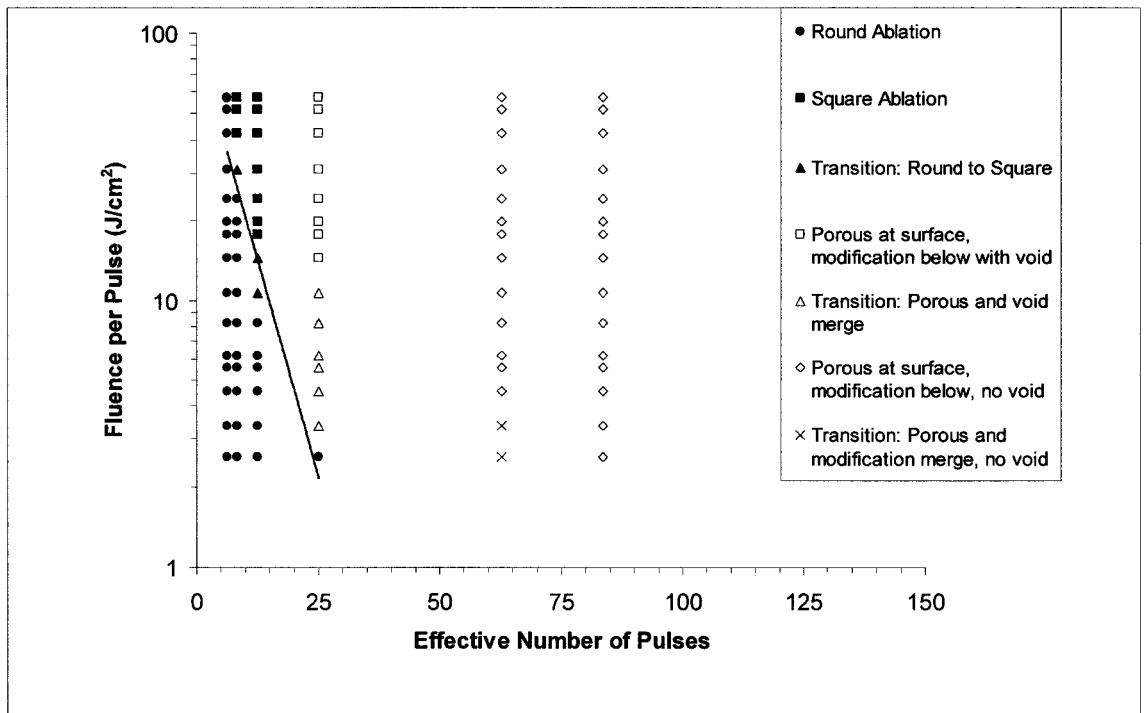
(b)

Figure 6-13: Experimental phase plots showing conditions when each type of ablation is observed. (a) Fluence per pulse vs. translation speed (b) Fluence per pulse vs. effective number of pulses

6.2.1.2   Depth Characterization: Plots and Equations

The depths of both ablation and modification were first characterized in terms of the effective number of pulses. A plot is shown in Figure 6-14. When subsurface modification occurred, there was some material removed and this was measured as an ablation depth. However, these cannot be considered true grooves as they are largely filled in with chunks of solidified material. Interestingly, there is no 'overflow'. There appears to be a threshold as N_{eff} increases past 25. Below this value there is ablation and above is subsurface modification with no void. At $N_{eff} = 25$, there is subsurface modification with a void at the bottom.

In the ablation regime, the depth as a function of N_{eff} appears to be exponential, as in Equation 6-9. The parameter a appears to be a depth when zero pulses have reached the surface. The quantity b indicates how fast the depth increases with the number of pulses, which increases with increasing fluence.

In the subsurface modification regime, the depth appears to be logarithmic, as in Equation 6-10. The parameters x and y are depths and z appears to be the number of pulses after which the subsurface modification occurs. Both fits include the point at $N_{eff} = 25$. A plot showing the fits is shown in Figure 6-15. All fit parameters are summarized in Table 6-1.

$$d = ae^{bN_{eff}} \qquad \text{6-9}$$
$$d = x + y\ln(N_{eff} - z) \qquad \text{6-10}$$

Table 6-1: Fit parameters for Equations 6-9 and 6-10 as plotted in Figure 6-13

Fluence (J/cm^2)	a (μm)	b	x (μm)	y (μm)	z
42	4.1 ± 0.3	0.106 ± 0.003	39 ± 10	17 ± 2	22 ± 1
20	3.9 ± 0.3	0.084 ± 0.003	20 ± 5	10 ± 1	21 ± 1
11	3.3 ± 0.2	0.070 ± 0.003	19 ± 5	4 ± 1	24 ± 1

A   B   C
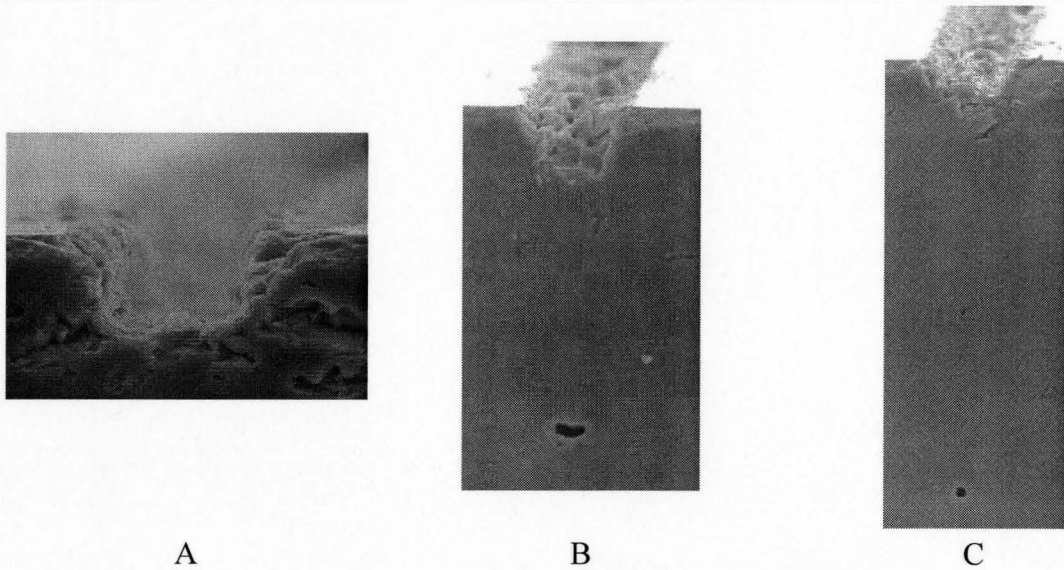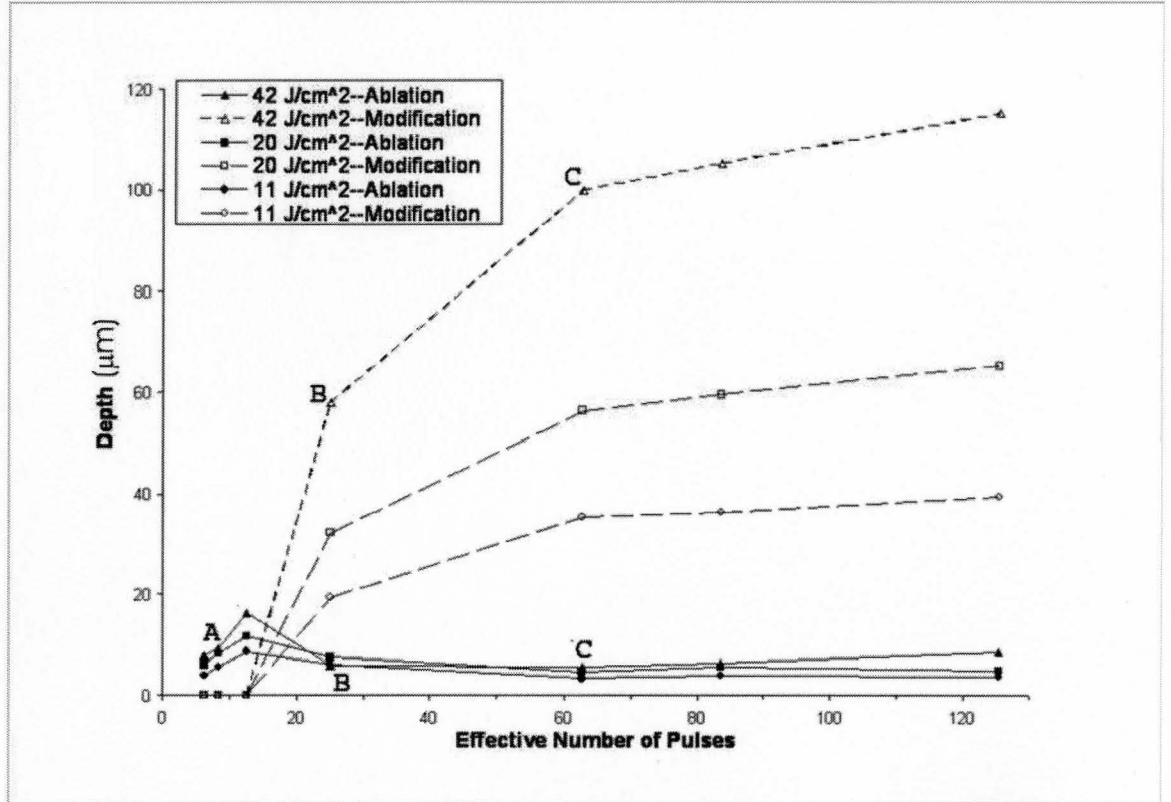
Figure 6-14: Depth as a function of N_{eff} for all damage types at various fluences Ablation below N_{eff} = 25 is much cleaner than ablation above.   At N=25 subsurface modification appears with a void at the bottom. The lines connecting the points are simply guides. The images A, B and C are of points marked in the graph at 42 J/cm^2.
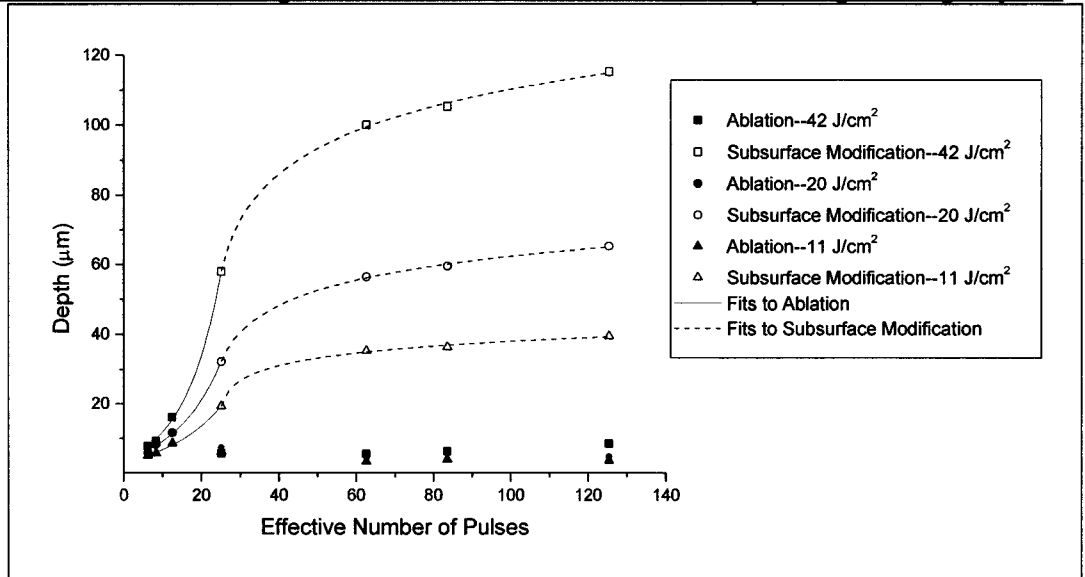
Figure 6-15: Fits for ablation and subsurface modification. The small ablation depths above N=25 are neglected. The point at N=25 are included in both fits. That is where there is deep modification with a void at the bottom. The ablation fits are exponential according to Equation 6-9. The subsurface modification fits are logarithmic according to Equation 6-10.

Next, the depth as a function of fluence was characterized. Beginning with the ablation regime, the depth shows a different behaviour for round and square ablation. As shown in Figure 6-16, up to a fluence of 20 J/cm^2 the depth increases logarithmically, as in Equation 6-11 (Equation 4-7). Above 20 J/cm^2, the depth increases exponentially, as in Equation 6-12. The parameter d_o is the ablation depth at fluence $e \times F_{th}$. F_{th} is an ablation threshold for grooves cut with a given feed rate. The quantity $l = d_o/N_{eff}$ is an ablation depth per pulse at a fluence of $e \times F_{th}$. The fit parameters are shown in Table 6-2. This shift from logarithmic to exponential increase in depth is indicative of a switch from gentle to strong ablation. In the gentle regime, the groove bottom is round. In the strong regime, the groove bottom is flatter. There appears to be a dip in the groove depth as the transition from round to square ablation takes place, so in certain cases, grooves of equal depth but different morphology can be created using different pulse energies. Figure 6-16 also shows images of where the depths are equal but the morphology is different.
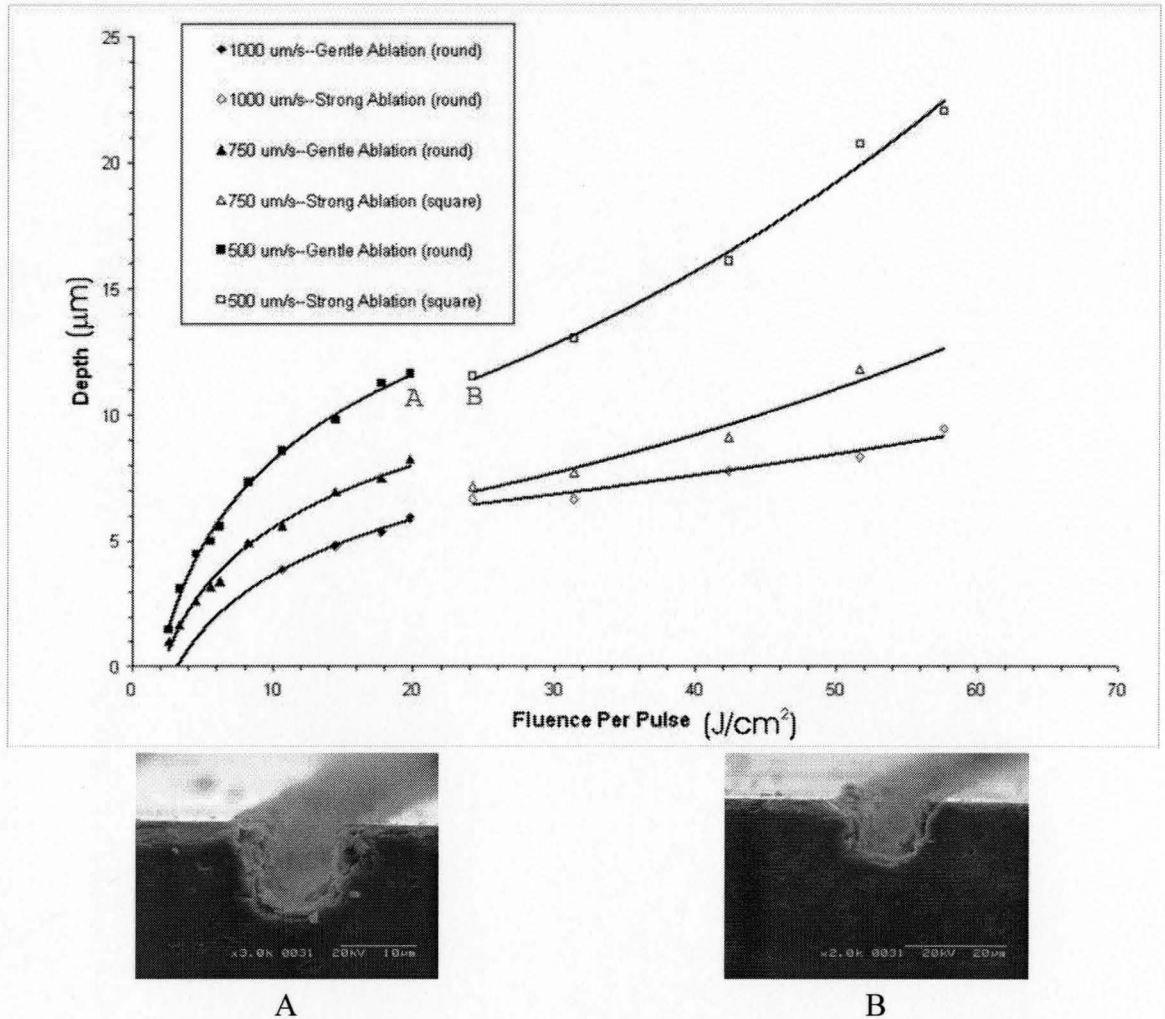
$$d(F) = d_o \ln\left(\frac{F}{F_{th}}\right) \quad \text{6-11}$$

$$d = A \cdot e^{BF} \quad \text{6-12}$$

52

Table 6-2: Fit parameters for Equations 6-11 and 6-12 as plotted in Figure 6-16

| Cutting Speed (μm/s)	N_{eff}	d_o (μm)	$l=N_{eff}/d_o$ (μm)	F_{th} (J/cm^2)	A (μm)	B (cm^2/J)
1000	6.27	3.2 ± 0.2	0.51 ± 0.03	3 ± 2	4.9 ± 0.3	0.011 ± 0.001
750	8.33	3.6 ± 0.1	0.43 ± 0.01	2.1 ± 0.6	4.3 ± 0.5	0.019 ± 0.003
500	12.53	4.9 ± 0.1	0.39 ± 0.01	1.9 ± 0.6	7.0 ± 0.5	0.020 ± 0.001

Figure 6-16: Ablation depth as a function of fluence for gentle and strong ablation. The groove shape is marked in the legend. Images A and B are of locations marked on the plot (note the different scales). The fit to gentle ablation is logarithmic according to Equation 6-11. The fit to strong ablation is exponential according to Equation 6-12.

The depth as a function of fluence for deep modification was then characterized. A slightly sub-linear power law can characterize this depth, as in Equation 6-13. Where there is a void at the bottom the parameters are quite different. The fit is shown in Figure 6-17 and the fit parameters are summarized in Table 6-3. Table 6-4 summarizes all of the characteristic equations one last time.

$$d(F) = p(F)^q \quad \text{6-13}$$

Table 6-3: Fit parameters for Equation 6-13 as plotted in Figure 6-17

Cutting Speed (μm/s)	N_{eff}	p	q
250	25.07	2.4 ± 0.2	0.87 ± 0.02
100	62.67	5.6 ± 0.2	0.77 ± 0.01
75	83.55	5.1 ± 0.3	0.82 ± 0.01
50	125.33	5.7 ± 0.2	0.80 ± 0.01
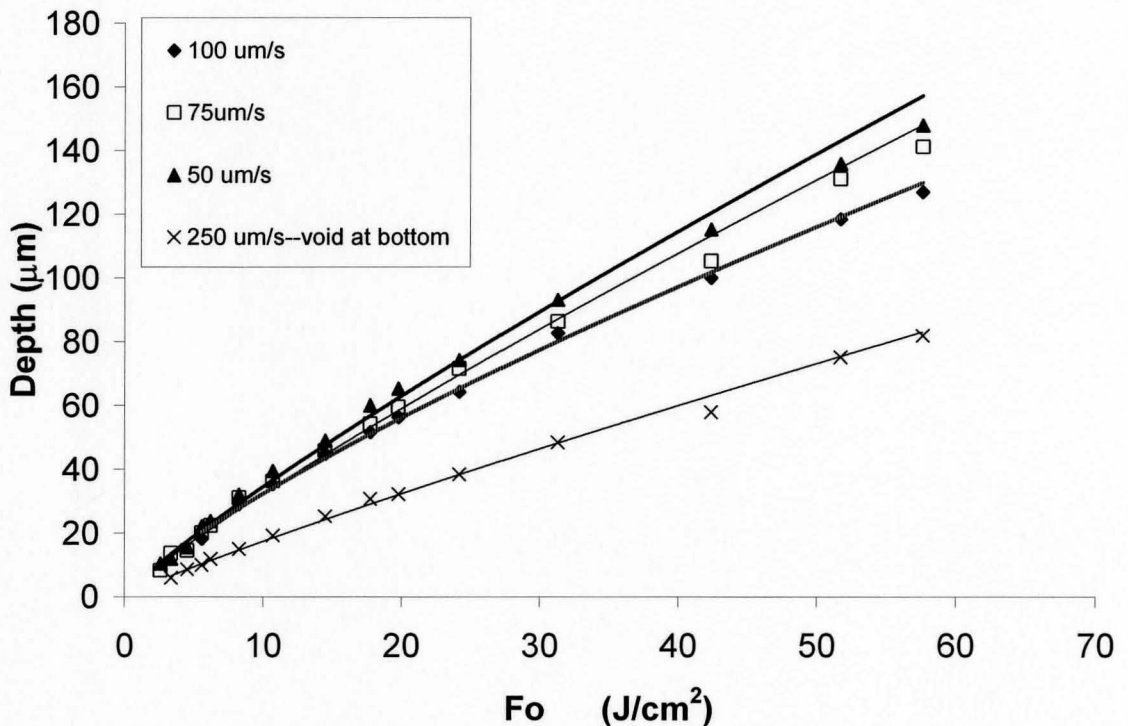
Figure 6-17: Depth as a function of fluence for deep modification. The fits are to a power law, as in Equation 6-13.
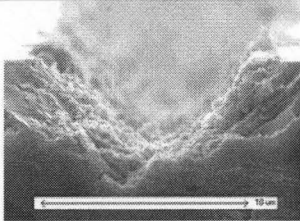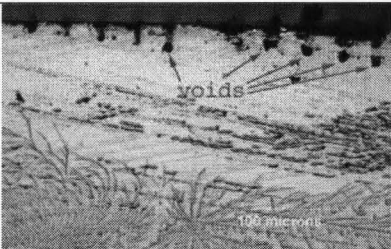
Table 6-4: Equations describing micromachining of grooves in lithium niobate

	Ablation		Subsurface Modification	
	Gentle $F < F_o e^{\frac{v}{v_o}}$	**Strong** $F > F_o e^{\frac{v}{v_o}}, v>v_o$	**Without void** $F > F_o e^{\frac{v}{v_o}}, v<v_o$	**with void** $F > F_o e^{\frac{v}{v_o}}, v=v_o$
d(F)	$d = d_o \ln\left(\dfrac{F}{F_{th}}\right)$	$d = A \cdot e^{BF}$	$d = pF^q$	
d(N_eff)	$d = ae^{bN_{eff}}$		$d = x + y\ln\left(N_{eff} - z\right)$	
$v_o = 241 \pm 11$ μm/s, $N_{eff} = 26 \pm 1$, Other fit parameters defined previously				

6.2.1.3   Crystal Orientation Dependence

The next experiments were performed in order to determine if the crystal orientation is an important factor in groove cutting. Single-pass grooves were machined on an x-cut sample parallel to the z-axis and on a z-cut sample parallel to the y-axis. In both cases the laser polarization was perpendicular to the cutting direction. On each sample, the same features were observed for as a result of micromachining: round ablation, square ablation and subsurface modification with and without a void at the bottom. Images of these features on x- and z-cut samples are shown in Figure 6-18.

The depths of the features were measured and compared with the y-cut results. There is no distinction between the crystal orientations, as shown in Figure 6-19 and, subsequently, the characterization of the machining parameters is the same as for the y-cut sample described above.

	X-Cut	Z-Cut
Round Ablation	Depth: 6 μm	
Square Ablation	Depth: 14 μm	
Modification With Void	Surface to void bottom: 58 μm	Unpolarized Optical Image
Modification Without Void	Modified Depth: 32 μm	Polarized Optical Image

Figure 6-18: Features resulting from laser micromachining of x- and z-cut lithium niobate samples
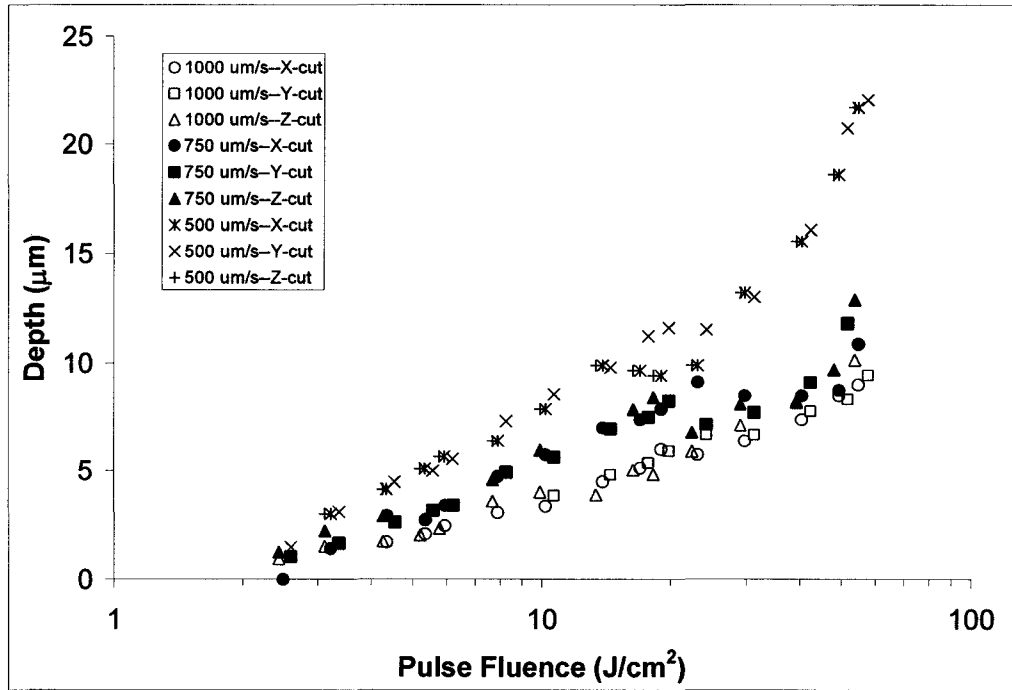
(a)
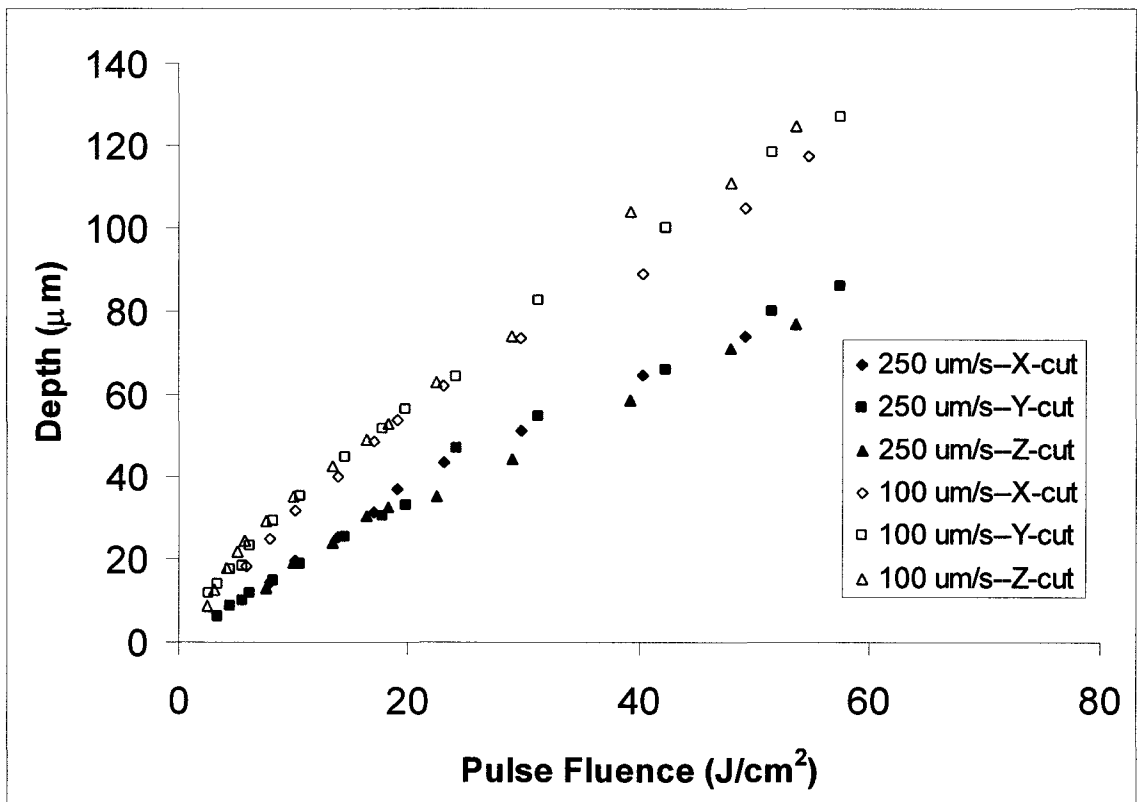
(b)

Figure 6-19: Comparison of feature depths of the three crystal orientations: (a) ablation (gentle and strong) and (b) subsurface modification.

6.2.1.4   Effect of Laser Polarization Orientation

Next, the effect of laser polarization on groove cutting was examined. Returning to the y-cut sample, grooves were machined using three different laser polarizations: perpendicular to the groove direction (as was used with all experiments presented so far), parallel to the groove direction and circular. The laser polarization has a significant effect on the groove morphology under certain conditions, as shown in Figure 6-20. In the round ablation regime, when the polarization is perpendicular to the cutting direction, the groove is very clean-looking, with no surface debris and a smooth bottom. When the polarization is parallel to the cutting direction, there is a large 'rim' along the groove on the sample surface and the groove bottom is very rough. As the fluence is reduced, the amount of surface debris and the roughness decrease. With circular polarization, the groove morphology is very similar to that of grooves cut with perpendicular polarization in all cases. Similar results are observed in the square ablation regime. A further observation is that the 'square' grooves have a slightly higher aspect ration when parallel polarization is used. In the subsurface modification regime, the surface is again much rougher with parallel polarization than with perpendicular or circular. The modification is still present. Though it is difficult to see in the SEM images, polarized light microscopy reveal the modification quite clearly. The SEM images are shown to illustrate the differences in surface morphology. The depths of ablation and modification were measured and compared for the three polarizations, as shown in Figure 6-21. For ablation, there appears to be no distinguishable difference in depth due to the laser polarization, other than a larger spread in the parallel polarization depths, likely due to the roughness of the groove bottom. For the subsurface modification, there also appears to be no significant difference in the depths for the different polarizations used.
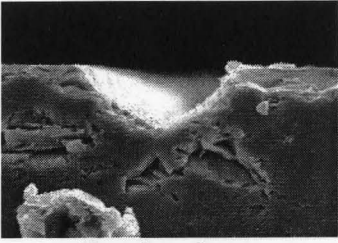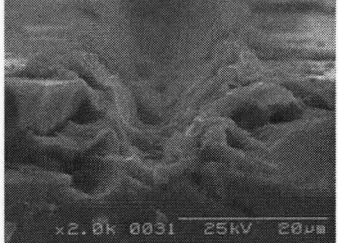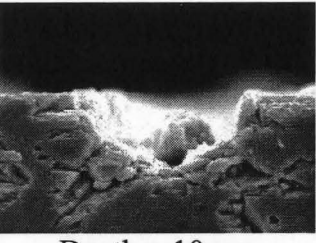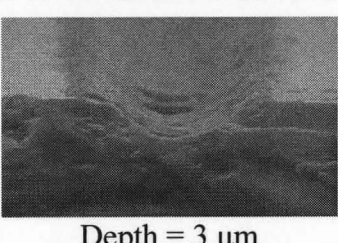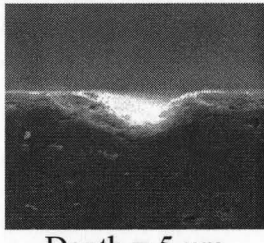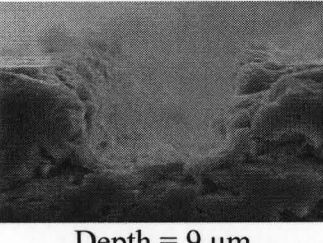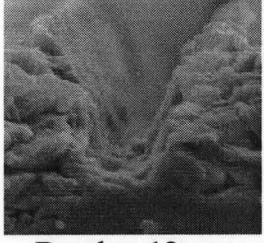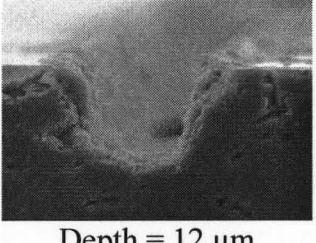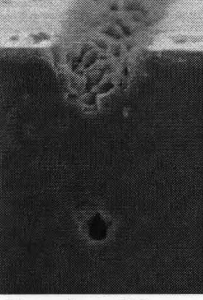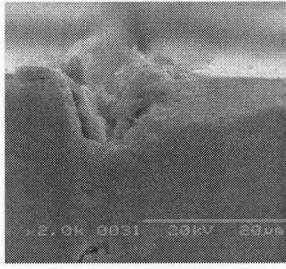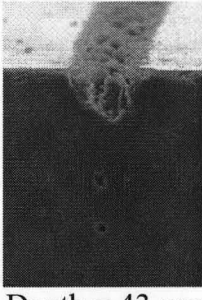
Regime/ Fluence (J/cm²)	Perpendicular to Cutting direction	Parallel to Cutting direction	Circular
Round Ablation 1000 μm/s	Depth = 9 μm	Depth = 10 μm	Depth = 10 μm
52 J/cm² 15 J/cm²	Depth = 5 μm	Depth = 3 μm	Depth = 5 μm
Square Ablation 750 μm/s 42 J/cm²	Depth = 9 μm	Depth = 12 μm	Depth = 12 μm
Subsurface Modification with void 250 μm/s 20 J/cm²	Depth = 33 μm		Depth = 43 μm
Without void 75 μm/s 52 J/cm²	Depth = 141 μm	Depth = 138 μm	Depth = 146 μm

Figure 6-20: Grooves machined using three different laser polarizations at various cutting speeds
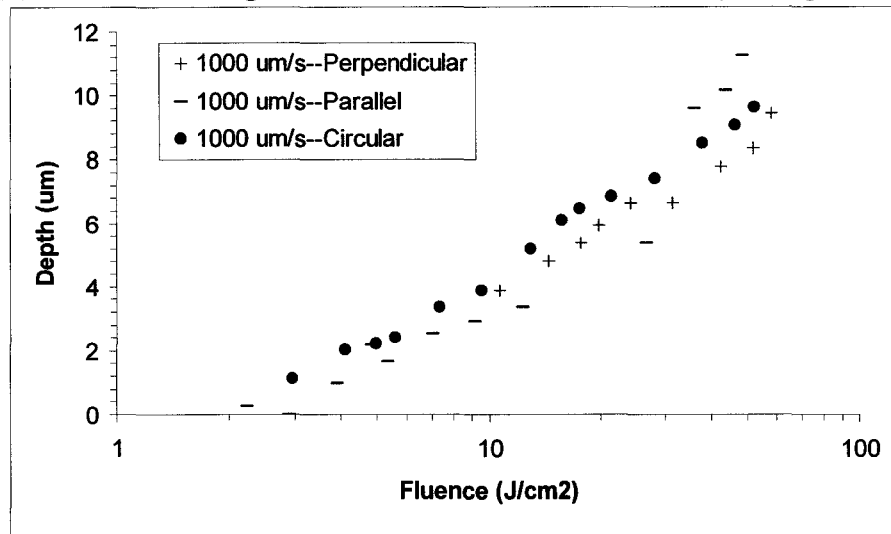
(a)
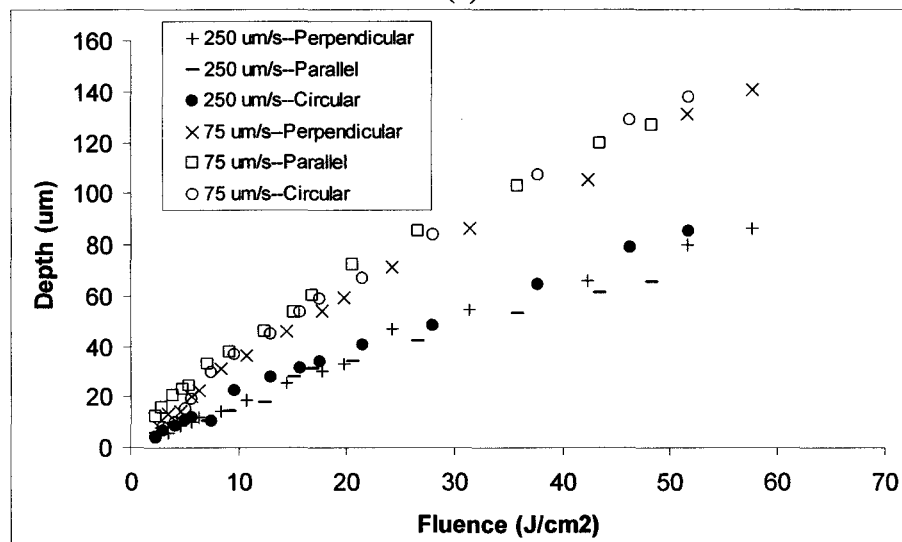
(b)

Figure 6-21: (a) Ablation and (b) modification depths of grooves machined using three different laser polarizations: Perpendicular and parallel to the cutting direction, and circular.

6.2.1.5   Analysis of Subsurface Modification

To further study the subsurface modification, a series of identical grooves were created on a single sample, cross-sectioned and thinned for TEM imaging. The grooves were created using 52 J/cm^2 pulses at 200 μm/s, spaced 60 μm apart. The images are shown in Figure 6-22. The interface between a modified region and an unmodified region is shown in Figure 6-22 (a) and (b) and the respective diffraction patterns are shown in (c) and (d). The modified region is clearly amorphous, while the unmodified region is crystalline, as one would expect. The interface is defined by a crack, which

may be the result of the laser interaction or post-irradiation sample processing. Along the interface is a region of recrystallized material.
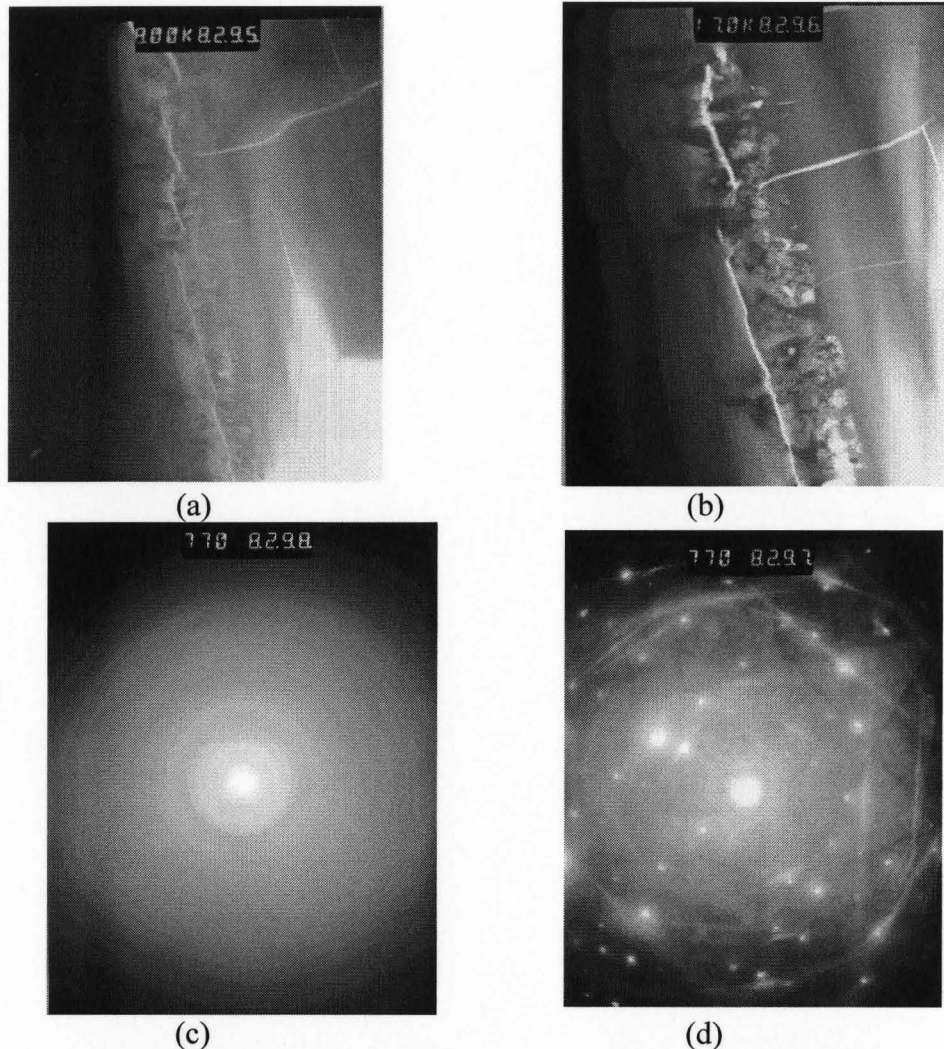
Figure 6-22: TEM images of subsurface material modification
(a) Interface between modified region (right) and unmodified bulk (left)
(b) Higher magnification of (a)
(c) Diffraction pattern of the modified region
(d) Diffraction pattern in unmodified region

Further to the characterization presented above, the depth of amorphous channels (subsurface modification) can be further simplified by plotting depth as a function of $N^{1/4}F$. As seen in Figure 6-23, allows a single Equation (6-14) to describe the depth for speeds less than 250 μm/s, where a = 2.2 ± 0.1 and b = 0.80 ± 0.01.
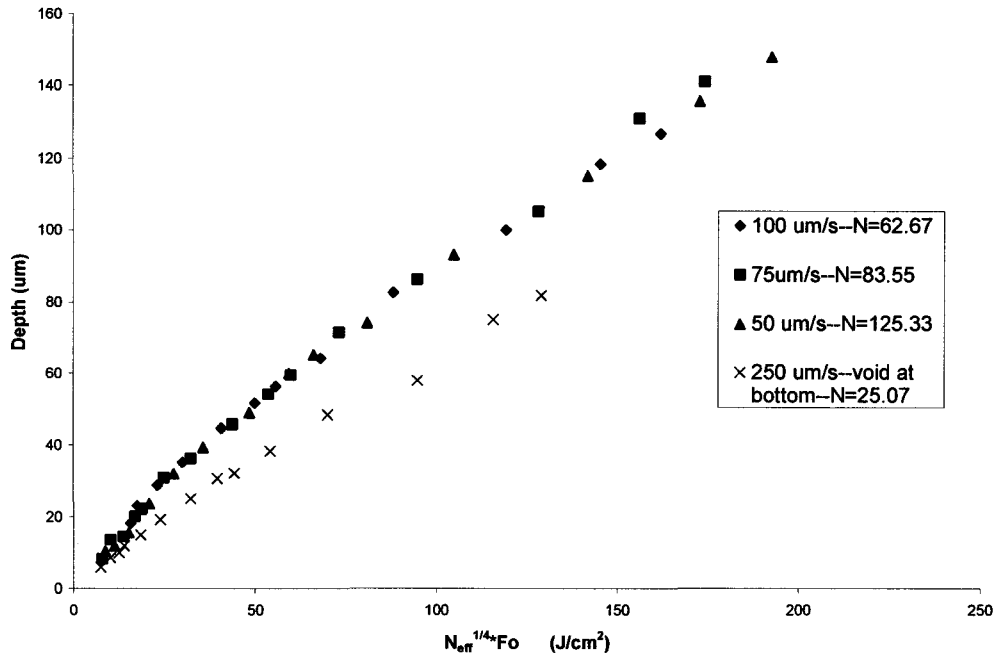
Figure 6-23: Depth characterization of amorphous channels

$$d = a\left(N_{eff}^{\frac{1}{4}}F\right)^{b} \quad \text{6-14}$$

If $N_{eff} = \sqrt{\frac{\pi}{2}}\frac{\omega_o f}{v}$ is substituted, the depth has a repetition rate dependence, which indicates a temporal effect is present.

6.2.1.6   Effect of Multiple Consecutive Passes

Finally, grooves machined with multiple consecutive passes over the same line were machined in order to determine if the creation of deep, high-aspect ratio features is possible. Figure 6-24 shows images of some of the resulting grooves.

When the conditions are such that there is subsurface modification for a single pass (100 μm/s), grooves can be created using multiple passes as seen in the bottom row of the figure. This is an interesting effect, because simply increasing the number of pulses in the single pass regime does little towards removing more material. This indicates some sort of temporal dependence, perhaps thermal or compositional effects. The groove morphology is much worse than when in the single-pass ablation regime (first two rows of the figure) until several passes are completed. The grooves are partially filled in and have a very rough bottom.

In the ablation regime, high quality deep grooves can be created. The grooves have almost no rim and the sidewalls appear quite smooth. Any depth is attainable by adjusting the number of passes and the pulse fluence.

Figure 6-25 shows the depths under various conditions. Figure 6-25 (a) shows the depths in both the modification and ablation regimes. In the modification regime, while the depth clearly increases with the number of passes, the poor groove morphology makes it difficult to define and measure the depth. In the ablation regime, the multi-pass groove depth is more clearly defined. The depth appears to have a logarithmic dependence on the number of passes, as shown in Figure 6-25 (b). At slower speeds (500 and 750 µm/s), this dependence decreases above 10 passes and appears to saturate. Figure 6-25 (c) shows the depth dependence on fluence at constant speed and number of passes. The relationship also appears to be logarithmic.
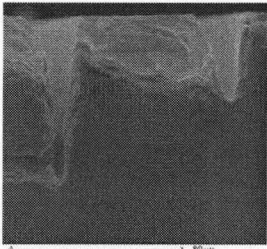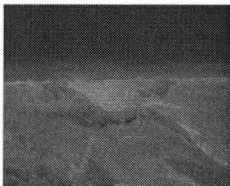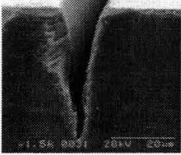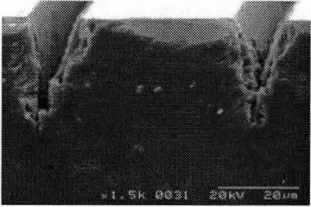
Figure 6-24: Grooves machined with multiple consecutive passes
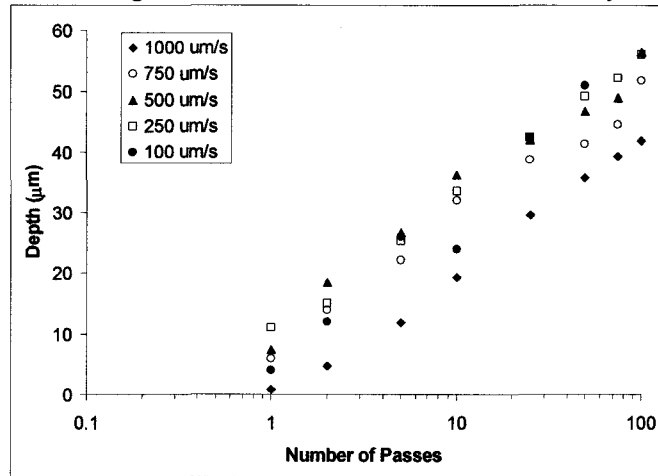
(a)
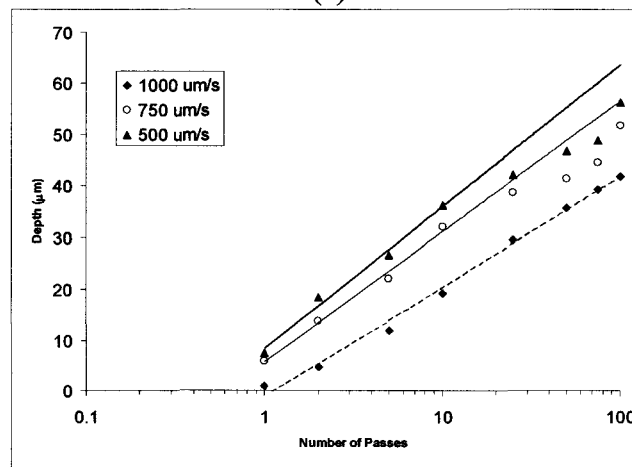
(b)
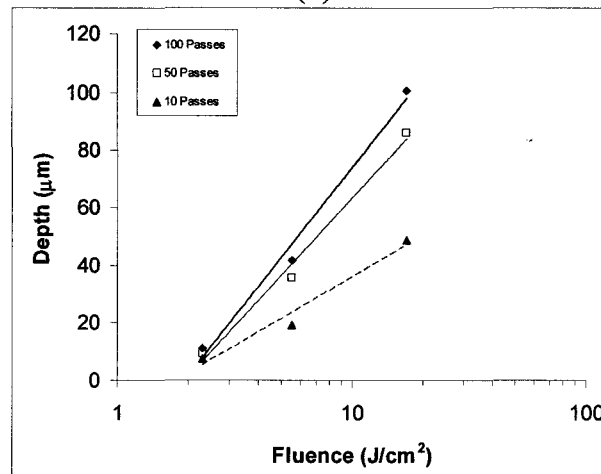
(c)

Figure 6-25: Depths of grooves machined with multiple consecutive passes at 2.5 J/cm^2: (a) Depth as a function of number of passes in ablation and subsurface modification regime
(b) Depths in ablation regime with logarithmic fits
(c) Depth as a function of fluence at 1000 μm/s

6.2.2 Discussion

6.2.2.1   Summary of Results

In groove cutting, when increasing the effective number of pulses (i.e. decreasing the cutting speed), there is a transition from an ablation regime, where grooves with excellent morphology are created, to a modification regime, where little material is removed, but the crystal is nonetheless altered down to a significant depth. This modified material was shown to be amorphous.

The ablation depths increase exponentially with increasing number of pulses until a threshold is reached, approximately $N_{eff} = 25$, and the deep modification begins. The modification depth then increases logarithmically with N_{eff}, showing a near independence on the number of pulses. With fluence, the ablation depths increase logarithmically at first and then exponentially above 20 J/cm^2. The modification depths increase slightly sub-linearly with fluence.

With multiple consecutive passes in the modification regime, amorphous material was removed with each pass. This indicates a temporal effect, since more pulses in a single pass (i.e. a slower speed) did not result in much more material being removed. The groove morphology was not very good until many passes were completed. Deep grooves with good morphology were created with multiple passes in the ablation regime.

Neither crystal orientation nor laser polarization had any significant effect on the groove depths. However, the best morphology was obtained when the laser polarization is perpendicular to the cutting direction.

6.2.2.2   Machining of Grooves—Ablation Regime

In the ablation regime, depths for single-pass grooves have been characterized using Equations 6-9, 6-11 and 6-12. Equation 6-9 gives the depth as an exponential function of N_{eff}. This is in contrast to the depth dependence for InP, which is linear with respect to N_{eff}[32]. For lithium niobate the ablation rate is accelerating. Equation 6-11 gives the depth as a logarithmic function of fluence, which at low fluence is the same relationship as for InP (with different fit parameters, naturally). At higher fluences, there is a shift to an exponential dependence for lithium niobate. This depth dependence is indicative of a shift from gentle to strong ablation. However, again in contrast to InP, the strong regime for lithium niobate is characterized by an exponential as opposed to another logarithmic function for InP.

That different relationships characterizing ablation depths are apparent in lithium niobate is not entirely surprising, given that the range of fluences and cutting speeds used here is greater than most and that the crystal structure is more complex than that of many materials previously studied. However, it is still desirable to relate certain quantities to previous results. A comparison of ablation thresholds obtained for grooves with those obtained for single and multiple pulses in these experiments shows that the thresholds $F_{th}(N_{eff})$ are slightly larger than those obtained here for the multiple-pulse cases. However, the quantity N_{eff} is only an approximation to the number of pulses, so an exact correlation would not be expected. Furthermore, the repetition rate for the multi-pulse experiments was 50 Hz and that for grooves was 1000 Hz. It appears from the multi-pass groove experiments that there is a dependence on the time between pulses. A better comparison would be to compare multi-pulse crater depths with the multi-pass groove depths, though, unfortunately, crater depths were not available. In any case, the threshold for grooves does decrease with increasing N_{eff}, indicating significant incubation, as with multiple pulses. For further comparison, Deshpande [42] reports ablation depths per pulse for single- and five-pulse processing (of stationary samples) as a function of fluence, which are in general agreement with the experiments here. Deshpande's values are slightly less than those presented in the previous section for $l = d_o/N_{eff}$ at fluence $e \times F_{th}$ and repeated here in Table 6-5. However, the uncertainties presented here are from the fitting routine only and Deshpande used stationary samples.

Table 6-5: Ablation depths per pulse at fluence $e \times F_{th}$

N_{eff}	$l = N_{eff}/d_o$ (µm)
6.27	0.51 ± 0.03
8.33	0.43 ± 0.01
12.53	0.39 ± 0.01

A transition threshold from gentle to strong ablation for lithium niobate has not to the author's knowledge been presented previously. The ablation of grooves suggests that this occurs in the range 20 to 25 J/cm². That the strong ablation grooves have vertical sidewalls and flat bottoms is interesting. This is a phenomenon that has not been reported for lithium niobate. However, flat-bottom craters have been observed and modelled in wide-bandgap dielectrics [55]. Their creation is attributed to the optical properties of the plasma generated by ablation, which affect the beam intensity profile by means of a greatly increased reflectivity and absorption coefficient. The square craters were observed for single-pulse ablation and occur only at higher fluences. Experiments were performed and compared to the model, with good results for fused silica. This theory may also apply to lithium niobate, since the square ablation was only observed at higher

fluences. The experiments here involved grooves, so the determination of depth profiles for single-pulse ablation and an application of the model to lithium niobate would be a worthwhile experiment. Whether even deeper square ablation can be achieved is also worthy of exploration, since it is often desirable to have vertical sidewalls while fabricating devices, ridge waveguides being one example.

A characterization of multiple-pass grooves was also presented. To date, it seems as though a detailed characterization for grooves has not been presented in the literature for lithium niobate, so the current results introduce an expanded set of parameters that can be used to create features of a desired depth. However, the trends for the groove depths are similar to those for other materials. It is seen that at 750 μm/s and 500 μm/s the depth appears to saturate above 10 passes. This saturation has been attributed to the groove acting as a lossy hollow waveguide, prohibiting the pulses from propagating deeper into the material due to scattering and absorption [32]. The maximum depth observed in these experiments was 100 μm. By varying the pulse fluence and number of passes, any depth up to that is attainable. A depth limit with number of passes was not apparent at 1000 μm/s, so even greater depths are quite likely possible. The existence of an overall depth limit can be easily verified with further experimentation.

The crystal orientation again did not appear to affect the quality or features of the machined grooves. It was thought that the nonlinear properties of lithium niobate might have an effect on ablation. However, these properties are sensitive to crystal composition and structure. Incubation, as mentioned above, is present and there exists the strong possibility that the microscopic changes in the lithium niobate that result in incubation distort the crystal enough to eliminate any effects optical nonlinearity would have on ablation. Incubation plays a significant role in a mechanism that can account for many of the observations. This mechanism will be explained shortly.

The polarization of the laser beam relative to the groove direction has been studied previously in indium phosphide [32] and silicon [56], and it was found that polarization perpendicular to the groove direction gives the best results. The reason for the difference in machining quality of the two polarizations is that the beam does not strike the sidewalls (region where material removal is taking place) of the groove at normal incidence. So, the result is that when the polarization is parallel to the groove, the beam is s-polarized relative to the sidewalls and the beam is p-polarized when the polarization is perpendicular to the cutting direction. Absorption for p-polarized light is higher, giving improved ablation. The results for lithium niobate are in agreement with the previous results, with the polarization perpendicular to the cutting direction giving the best morphology for single pass grooves.

6.2.2.3   Subsurface Modification

Subsurface modification, as described above, has not been previously reported in lithium niobate or, to the author's knowledge, any other material. Subsurface features have been observed in the machining of silica glass. Campbell et al [44] reported bulk structures well below the sample surface, which were attributed to self-focusing of the laser pulses. However, no surface damage or modification between the structure and the surface was observed, as was the case in the present experiments, with the disrupted 'porous' surface and the amorphous region below the surface. It appears as though this is a new phenomenon, for which an explanation is sought.

As a first explanation, the subsurface modification may be caused by absorption of the pulses, distributed over a depth, which causes melting and amorphization. This possibility will be examined. Immediately, however, there are difficulties due to the fact that absorption at 800 nm is negligible, though absorption clearly occurs. Three-photon absorption (3PA) is a likely possibility but no 3PA coefficient for lithium niobate has been reported. As such, a rough absorption coefficient will be extracted from the data. Using a cutting speed of 100 μm/s (N_{eff} = 63) and a fluence of 31 J/cm^2, an amorphous depth of 83 μm is obtained. Assuming that the pulse is attenuated exponentially down to the observed damage depth d_0 at point A and also assuming that the fluence at the 'groove' bottom is the threshold fluence (0.55 J/cm^2 for $N \cong 60$), an effective absorption coefficient α can be determined by Equation 6-15, where F_o is the fluence at the surface and z is the depth. This gives α=0.049 μm^{-1}, which is an effective absorption coefficient taking into account any changes in absorption and is much greater than the nominal linear absorption coefficient for lithium niobate.

$$F = F_o e^{-\alpha z}   \quad \text{6-15}$$

Now, the temperature rise in small increments along the axis where a pulse strikes the surface can be estimated using Equations 6-16 and 6-17. Absorption only along the axis of the peak of the pulse is assumed (i.e. the wings of the Gaussian pulse are ignored), along with a starting temperature of zero degrees Celsius. Equation 6-16 gives the temperature rise in a given increment, where ΔF is the absorbed fluence, C = 0.15 cal/g/°C is the specific heat, ρ = 4.64 g/cm^3 is the volume density [57] and z_i is the increment size. The fluence F_n at the start of each increment is given by Equation 6-17, where the second term on the right-hand side gives the absorbed energy per unit area. The resulting temperature rise is shown in Figure 6-26. The melting point of lithium

niobate is 1250 °C. This indicates that material only as deep as 35 μm could be melted with a single pulse, although there is significant heating below.

$$\Delta T = \frac{\Delta F}{C \rho z_i} \qquad 6\text{-}16$$

$$F_n = F_{n-1} - \alpha F_{n-1} z_i \qquad 6\text{-}17$$
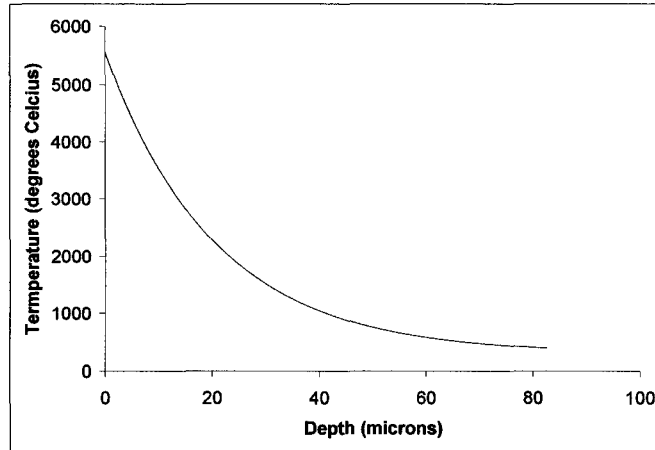
Figure 6-26: Estimated temperature rise as a function of depth along the pulse axis for a single pulse. The melting point is 1250 °C.

A single pulse cannot melt material down to the observed amorphous depths. The cutting of grooves, however, involves multiple pulses; so perhaps several pulses can cause cumulative heating and lead to deep material modification. A heating model to help determine whether this is the case is developed. The goal of the model is to determine a time constant for the heating and cooling of the region surrounding the irradiated region. If the time required for the temperature of a nearby point to cool after being heated is greater than the time between pulses, then cumulative heating due to multiple pulses is very likely to occur. A diagram outlining the model of sample heating is shown in Figure 6-27 and explained below.
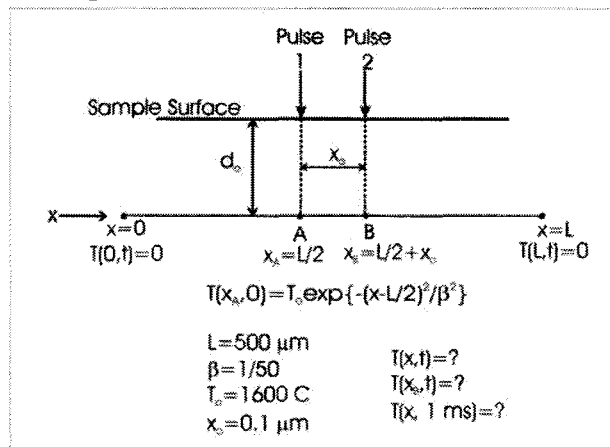
Figure 6-27: Diagram of simple heating model. See text for explanation.

It is desired to determine the effect of the heat generated by Pulse 1 on the material at the location where Pulse 2 will strike the sample. At 100 μm/s and a repetition rate of 1 kHz, this distance is $x_o = 0.1$ μm away. To simplify the problem, heat diffusion in only one dimension will be considered, and the temperature at Point B determined. For further simplification, uniform heating throughout the depth will be assumed, using the average temperature as obtained from Figure 6-26 which is $T_{av} \cong$ 1600 °C. Heat diffusion is described by Equation 6-18, where $\kappa = k/\rho C = 0.0144$ is the thermal diffusivity (assumed constant, calculated from data in [57], $k = 0.01$ cal/cm/s/°C [57]), which simplifies to Equation 6-19 in one dimension. The boundary conditions are as follows: At x = 0 and x = L in Figure 6-27, the temperature of the sample will remain unchanged, so $T(0,t)$ and $T(L,t)$ will be constant if L is large and the pulse strikes the sample at $L/2$. For simplicity in solving the Equation, $T(0,t) = T(L,t) = 0$ °C. L was chosen to be 500 μm, the y-cut sample thickness. $T(x,0)$ was assumed to be a narrow Gaussian (as an approximation to the delta function), as in Equation 6-20, where T_o is the peak temperature (T_{av} =1600 °C) and β defines the shape such that the width is much less than the spacing between pulse centres along the 'groove' (β was chosen to be 1/50). $T(x,0)$ is shown in Figure 6-28.

$$\frac{\partial T}{\partial t} = \kappa \nabla^2 T \qquad \text{6-18}$$

$$\frac{\partial T}{\partial t} = \kappa \frac{\partial^2 T}{\partial x^2} \qquad \text{6-19}$$

$$T(x,0) = T_o e^{-\frac{\left(x-\frac{L}{2}\right)^2}{\beta^2}} \qquad \text{6-20}$$
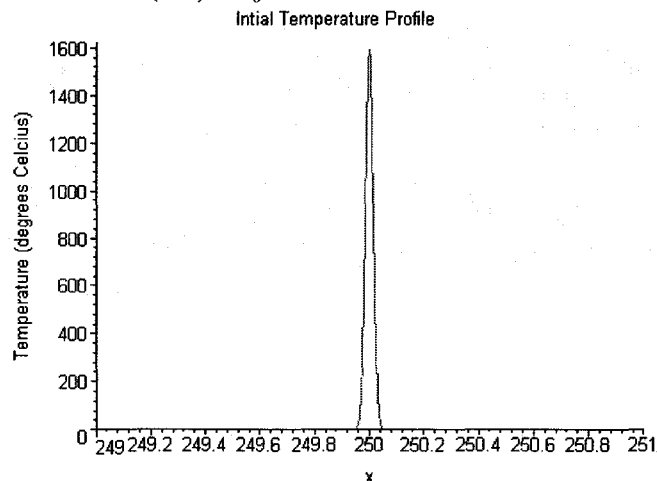
Figure 6-28: Initial temperature profile $T(x,0)$ as an approximation to the delta function for the simple heating model that is described in these paragraphs

The heat equation of 6-19 is a partial differential equation that is easily solved with the given conditions using separation of variables. The solution is a Fourier series with n terms. As a check of the solution, the distribution $T(x, 0+)$ (i.e. the temperature distribution just after heat diffusion has begun) should be very close to that of $T(x, 0)$ in Equation 6-20. These are plotted together in Figure 6-29 for $t = 1$ fs for $n = 200$ and $n = 401$. Clearly, the more terms that are used in the series, the better the approximation. Computer memory was limited, so a very good approximation was not possible; in this case the solution gives maximum temperature at $t = 0$ of 45°C is attained. However, the model is still instructive.

Temperature Profile at time T=0+
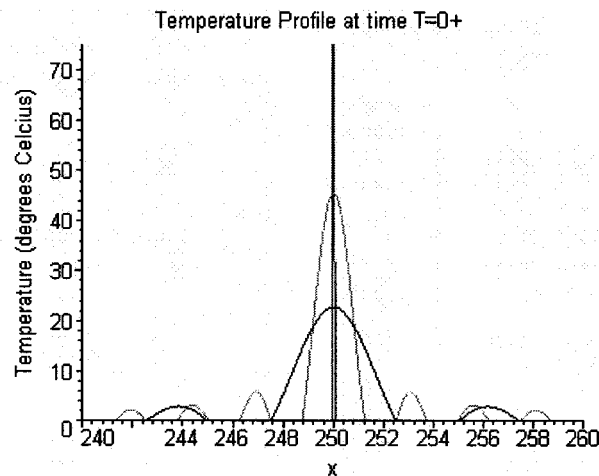
Figure 6-29: Temperature profile at time t=0 (tallest peak, which has been truncated) and time t = 0+ with n=200 terms in the Fourier series (lowest peak) and n=401 terms in the Fourier series (middle peak). The details are explained in the above paragraph.

Of interest are two main parts of the solution. The first is the temperature as function of x at 1 ms (corresponding to the 1 kHz repetition rate of the laser). A plot of this is shown in Figure 6-30. Clearly, much of the heat has dissipated, although complete cooling to the initial sample temperature hasn't yet occurred. The second is the temperature as a function of time at Point B, shown in Figure 6-31. At Point B, the temperature drops exponentially from its value at $t = 0+$ (It is expected that a rise in temperature would be seen before the drop, however, this does not appear with the number of terms used in the Fourier series. Initial temperature profile is too wide to show a rise in temperature). The time constant for the decay is 28 μs.

Temperature Profile at time T= 1 ms
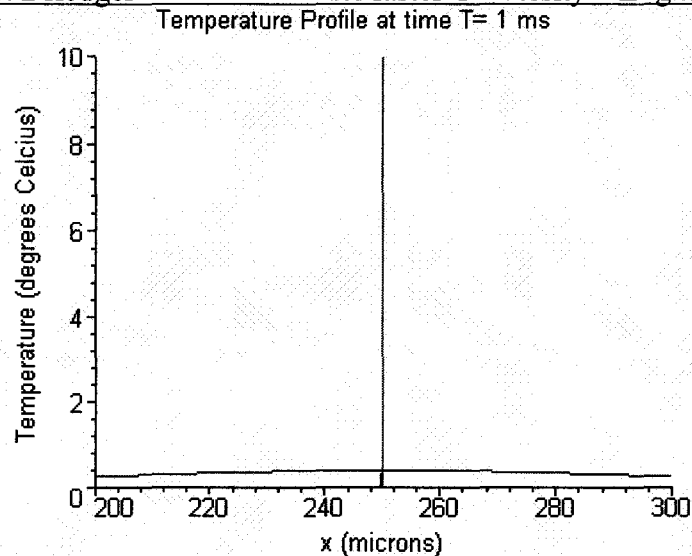
Figure 6-30: Temperature profile after 1 ms using n=401 terms

Temperature Profile at x=0.1 microns
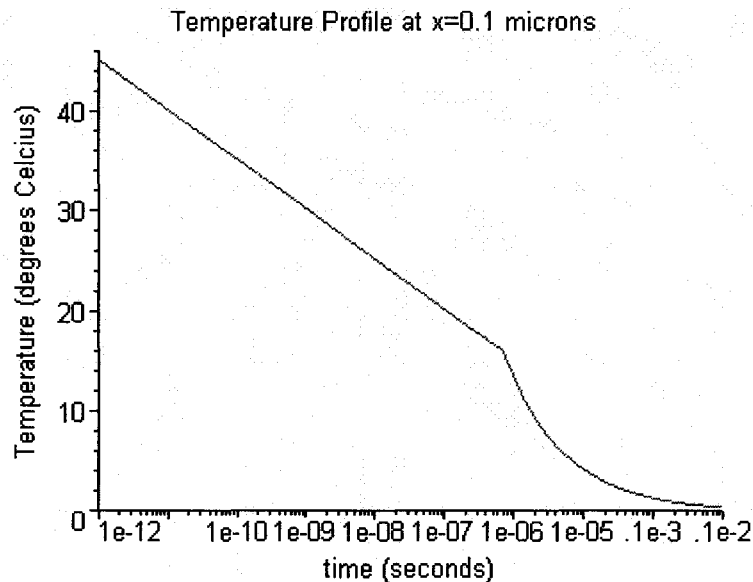
Figure 6-31: Temperature profile at Point B, x=0.1 μm from the pulse axis.

The time constant of 28 μs for the cooling is two orders of magnitude shorter than the time between pulses, which is a strong indication that cumulative heating does not occur. So, it appears that the deep channels are not the result of exponential absorption followed by cumulative heating. Clearly, this model can be greatly improved in several ways. Accounting for the Gaussian shape of the pulse would increase the amount of energy delivered to the sample with each pulse. Accounting for the three-dimensional nature of the problem would increase the volume over which the heat is distributed. The non-uniform heat distribution caused by the first pulse would also alter the solution, as would the temperature dependence of the thermal diffusivity.

Another way to check if cumulative heating occurs is to determine the thermal diffusion distance using the time between the pulses. This can be done using Equation 6-21, where κ is the thermal diffusivity as before and τ is the time between pulses (1 ms). This distance is approximately 38 μm. Compared with the pulse spacing of 0.1 μm at 100 μm/s this distance is quite large, meaning the heat from the first pulse has significantly dissipated when the second pulse strikes the sample. So, even with an improved model, it is highly unlikely that cumulative heating occurs. This means that the deep amorphization must still be accounted for.

$$l = \sqrt{\kappa \tau} \quad \text{6-21}$$

In this regard, the shape of the amorphous channels is of interest, since energy must be delivered in a columnar fashion to account for the channel shape. From the data, it seems plausible to suggest that waveguiding is occurring, as explained below.

As partial confirmation of waveguiding, the shape of the amorphous channels is compared with the beam shape. The beam divergence was determined from the numerical aperture (NA) of the objective lens, which was specified to be NA=0.14. Equation 6-22 yields the divergence angle θ_d where n is index of refraction of the propagation medium. In air, the divergence angle is 8° and in lithium niobate ($n \approx 2.21$) it is 3.63°. Assuming the focal point was at the sample surface, which was experimentally attempted for each experiment, an approximation of the beam shape can be determined, as in Figure 6-32 (a), using geometric optics. Figure 6-32 (b) shows a comparison of the beam divergence and an amorphous channel. Towards the bottom of the channel, the channel is clearly narrower than the beam width. If waveguiding were not occurring, it might be expected that the channel would widen with the beam. The lack of divergence could be due to the attenuation of the outer portion of the Gaussian-shaped pulses but, as seen in Figure 6-32 (b), the channels do not taper gradually. Instead, the edges remain virtually parallel as the depth increases after an initial tapering.

$$NA = n \cdot \sin(\theta_d) \quad \text{6-22}$$

(a)

(b)
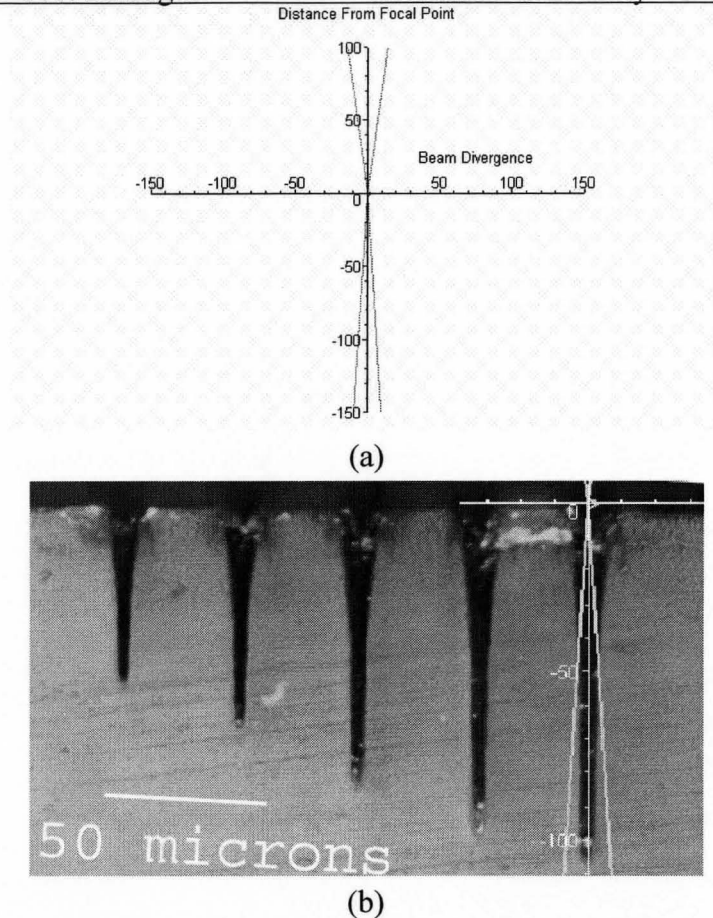
Figure 6-32: (a) Approximate beam shape after the objective, scales are in microns (b) Comparison of amorphous channel width to beam shape. Channels are made with constant cutting speed and increasing pulse energy from left to right.

To summarize this section, the amorphous channels are not the result of direct melting caused by simple absorption and cumulative heating. The shape of the channels suggests that the amorphous depths are attained by waveguiding. This observation is used, along with the incubation effect, to propose a mechanism, which can explain the deep amorphization along with the exponential increase in ablation rate.

6.2.3 Understanding the Observations

Once again, the observations so far will be summarized. When machining grooves with a decreasing cutting speed (i.e. increasing number of pulses), nice grooves are created with an exponentially increasing depth until a threshold is reached. Above the threshold, deep modification in the form of amorphous channels is created with little apparent material removal. The depth of the amorphous channels quickly saturates with increasing number of pulses. With fluence, the ablation depths increase logarithmically

and eventually exponentially. The amorphous channel depth increases nearly linearly with fluence. When multiple passes are used in the modification regime, further material is removed and after a large number of passes the groove shows a good morphology, indicating a time-dependent process exists which is likely not thermal. Multiple passes in the ablation regime give nice deep grooves with no apparent surrounding damage.

A mechanism that can consistently explain these results must account for the increase and sharp decrease in the amount of material that is removed. It also must account for the saturation of the amorphous channel depth with increasing N_{eff} as well as the fact that more pulses in a single pass do not remove material while more pulses applied with multiple passes does result in further ablation. A mechanism is suggested in the following paragraphs. The proposed mechanism requires several processes to occur and, while this one appears to account for many of the observations, there remains the possibility that other mechanisms, not yet suggested, may also explain the observations.

The process is depicted schematically in Figure 6-33, which shows what a cross-section of a groove might look like as more and more pulses are applied. The first pulse is where it is thought the most interesting phenomena occur. The first pulse is partially absorbed near the surface via three-photon absorption which results in surface ablation. Not all of the photons are absorbed since multi-photon ionization is not, in general, an efficient process. The remainder of the pulse passes deeper into the sample and remains of sufficient intensity to self-focus, thus narrowing the beam profile. The self-focussing beam results in mild incubation down to a specific depth determined by the initial pulse energy. Beyond this depth, the pulse is sufficiently attenuated to inhibit further incubation. The incubation results in an increase in refractive index, allowing further pulses to be guided along the same path, as well as increased absorption. This proposition for the effects of the first pulse requires three-photon absorption, self-focussing, a permanent increase in refractive index and increased absorption. There have been very few studies of high-order nonlinearities of lithium niobate crystals and no three-photon absorption coefficient for lithium niobate at 800 nm has been published, so a numerical model cannot as of yet be established. However, some experiments indicate that multi-photon absorption and self-focussing do occur in lithium niobate [58]. A permanent increase in refractive index caused by low intensity femtosecond laser irradiation has also been shown [59]. Prokhorov and Kuz'minov [4] review experiments showing that laser irradiation can distort the crystal structure. This distortion could possibly lead to the increased absorption.

Figure 6-33 (a) shows the sample after one pulse, which has these features: an ablated surface and an incubated region below with a shape resulting from self-focussing.
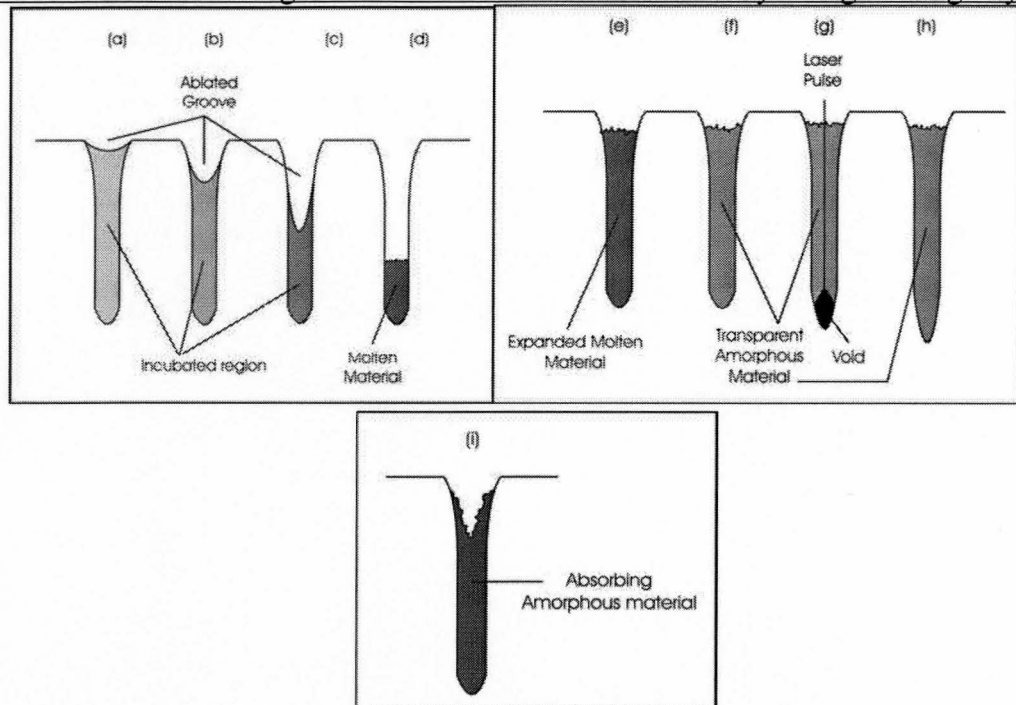
Figure 6-33: The mechanism explaining the presence of amorphous channels

(a) **The first pulse ablates some surface material and the remainder of the pulse is transmitted. Self-focussing, permanent refractive index increase and absorption increase (i.e. incubation) are thought to occur deep into the material.**

(b) **The second pulse ablates some more surface material and further incubates the 'waveguide' region.**

(c) **A few more pulses later, more ablation has occurred and enough incubation has occurred that further pulses are strongly absorbed (i.e. an incubation threshold is reached).**

(d) **The pulse is strongly absorbed, causing a large amount of material in the waveguide to be melted.**

(e) **The melted material expands to fill the groove.**

(f) **The expanded molten material cools to become a transparent amorphous solid.**

(g) **The next pulse is guided through the amorphous material, deepening the amorphous channel.**

(h) **The channel is deepened again, but only a little.**

(i) **After second pass, several seconds after the first, the amorphous material is absorbing, allowing further ablation.**

The sample after the second pulse is shown in Figure 6-33 (b). More ablation occurs via 3PA and the pulse is waveguided down the previously incubated region causing further incubation. This second pulse would not penetrate deeper into the sample than the first. Figure 6-33 (c) shows the sample after a few more pulses and iterations of the incubation and ablation process. Ablation accelerates due to the incubation process.

At the threshold, where the shift from ablation to deep modification occurs, enough incubation has occurred so that 3PA is no longer required for absorption. It becomes possible for linear absorption to occur, meaning an exponential attenuation of the pulse. This increases the absorption depth further into the incubated region and causes a significant amount of material to melt, as shown in Figure 6-33 (d). The melted material expands to nearly fill the groove due to thermal effects and the fact that the sample is in a vacuum, as shown in Figure 6-33 (e). The molten material is rapidly quenched, resulting in the formation of an amorphous solid.

As shown in Chapter 2, the phase diagram for lithium niobate (i.e. the Li_2O/Nb_2O_5 system) is rather complex, meaning a slight change in composition results in very different material properties. Deshpande et al. [42] have shown that when lithium niobate is exposed to femtosecond pulses, oxygen tends to be removed from the irradiated region. Furthermore, Sorescu [37] has shown that other crystal phases are present in samples after irradiation and ablation. Given this information, it seems inevitable that the composition of the molten lithium niobate will be different from that of the original crystal. For the results to be self-consistent within the context of this explanation, it is proposed that the amorphous material is initially transparent and remains so, on a time scale of a few milliseconds to several seconds (an admittedly broad range). After the system has equilibrated, the amorphous material becomes absorptive once again.

While this assumption may seem extreme at first, when it is used, both the rapid saturation of the channel depth (Figure 6-15) with N_{eff} without ablation along with the removal of more material with subsequent passes can be explained. Above the threshold N_{eff}, the now-filled groove acts as a waveguide with the transparent amorphous material at its core. This allows further energy to reach the bottom of the channel and increase the modification depth, as in Figure 6-33 (f). Because the channel is a poor waveguide, the energy reaching the channel bottom rapidly decreases. There are several seconds between passes of the sample under the laser, allowing the system to relax (Figure 6-33 (g)). After the second pass, ablation occurs once again (Figure 6-33 (h)).

This explanation accounts for the transition from ablation to deep modification. It also accounts for the acceleration ablation with N_{eff} as well as the limit on the depth of the amorphous channels. That the channel depth increase only with fluence, and not N_{eff}, does support the assertion that the amorphous depth is determined mainly by the first pulse.

Certainly, this explanation of the results, depicted in Figure 6-33, can be checked in a few ways. There would have to be a change in refractive index just below some of the ablated grooves. The density of the amorphous material should also be less than that of the original crystal if, in fact, molten material has thermally expanded to fill the groove. The composition of the amorphous material would also be different from that of lithium niobate. It is possible that there is an increase in oxygen content in the crystal surrounding the amorphous channels as well [42], as it has been proposed that heating and rapid cooling via laser irradiation can cause an oxygen deficiency [37]. Creating grooves using a greater variety of values of N_{eff} (i.e. different cutting speeds) would help to further characterize the process

That the amorphous material undergoes a change from being transparent to opaque would be more difficult to ascertain, but examining the effects of laser pulse repetition rate while keeping other parameters constant would be a starting point. Pulse repetition rate dependence has been investigated in lithium niobate previously [36, 39], though with much lower frequencies, longer pulse durations and shorter wavelengths were used, it was noticed that a higher repetition rate reduced desorption of atoms.

6.3 Absorption Mechanism and Incubation

6.3.1 Results

Absorption and incubation play an integral role in the explanation of the results that was just presented. As such, a preliminary investigation was conducted in order to determine the cause of incubation and any changes in absorption mechanism.

An experiment was performed where 'gratings' of slightly overlapping grooves were created. The pulse energy used was 4 µJ (9.5) J/cm^2 per pulse and two cutting speeds were used (200 µm/s and 1000 µm/s). The spacing between groove centres was 10 µm, just slightly less than the beam diameter, and the length of the grooves was 1500 µm. This created a large area patch for laser damage to be observed. The interesting

feature in this experiment is that the patch created at 1000 μm/s appeared light brown in colour and the patch created at 200 μm was dark brown.
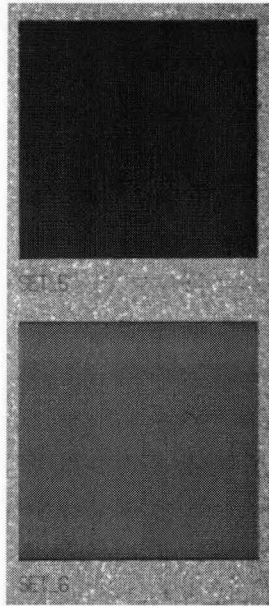
Figure 6-34: Large area 'patches' created with 4 μJ pulses at 200 μm/s (top), leaving a dark brown material, and at 1000 μm/s (bottom), leaving a light brown material. Though it is difficult to tell from this image, the patch surfaces were very rough.

6.3.2 Discussion

Now, so far an explanation for the presence of the amorphous channels has just been presented in the preceding paragraphs. What is required now is an explanation for the incubation that leads to the increase in absorption. This is discussed in the following paragraphs.

Three-photon absorption (3PA) is almost certainly the initial absorption mechanism. This can be inferred in two ways. The first is that the bandgap of lithium niobate is 3.9 eV and the photon energy was 1.55 eV (800 nm). The second is that Stuart [60] discusses an ablation model in detail, which proposes that the threshold fluence is proportional to the pulse duration τ according to Equation 6-23, where m refers to the number of photons required to overcome the bandgap energy ($m = 3$ for lithium niobate at 800 nm) and n_{cr} is the critical electron density in the conduction band for ablation to occur. This predicts a $\dfrac{\phi_{th}(150\,fs)}{\phi_{th}(300\,fs)}$ ratio of 0.63 which is very close to the experimental value of 0.60 (obtained using Deshpande's value for $\phi_{th}(300$ fs)=2.5 J/cm^2 and the current value of $\phi_{th}(150$ fs)=1.5 J/cm^2. This seems to be a good indication that 3-photon absorption is indeed the initial energy transfer mechanism in ablation of lithium niobate.

79

$$\phi_{th} \propto \tau^{\frac{m-1}{m}} n_{cr}^{\frac{1}{m}} \quad \textbf{6-23}$$

So, 3PA is likely the initial absorption mechanism. For subsequent pulses, however, 3PA is almost certainly not the main process. That initial pulses affect the absorption of subsequent pulses is evident in the non-unity incubation coefficient. This assessment is in agreement with Bunton [39]. However, exactly how incubation occurs, as well as how the absorption changes with femtosecond irradiation, in lithium niobate has not been firmly established. Again, however, the results do help indicate what is going on.

As mentioned previously, the 5-pulse ablation threshold found here and that reported by Deshpande are in agreement, despite the different pulse durations used. Normally, for multi-photon ionization, pulse duration affect the threshold. To eliminate the τ-dependence, Equation 6-23 requires $m = 1$, meaning that the absorption mechanism after 5 pulses becomes linear. (Due to the number of possible factors involved in the process and their uncertainties Campbell cautions against such inferences [44], but we will proceed nonetheless.) So, the absorption mechanism is changed from 3-photon to 1-photon.

This begs the question of what change occurs in the lithium niobate sample that results in linear absorption. In other words, what physical changes occur in the material that result in incubation? It was seen that the sample colour changes from clear to brown to dark brown when irradiated with an increasing number of pulses. This is indicative of thermal reduction [10], leaving an oxygen deficient material containing F and F^+ colour centres [11]. Arizmendi [11] found that thermally reduced samples have absorption bands centred at 2.6 eV (477 nm) and 3.1 eV (400 nm), although the absorption to below 1 eV is greatly increased. At 1.55 μm (800 nm), the room temperature absorption coefficient is increased from near zero to ~6 cm^{-1}, making linear absorption possible.

Moreover, illumination at either 2.6 eV (477 nm) or 3.1 eV (400 nm) was found to induce an absorption band at 1.6 eV (~800 nm), allowing for more efficient linear absorption. Two-photon absorption (2PA) at 800 nm would provide the necessary illumination in the 3.1 eV band. So, the creation of colour centres is a possible cause of the incubation effect.

Now, the causes of incubation and the increase in absorption coefficient as described in the previous paragraphs will be summarized: A possible absorption sequence begins with 3PA, which heats the sample on a short time scale, causing thermal

reduction, which induces broadband absorption into the near infrared due to the presence of colour centres. Linear absorption at 800 nm becomes non-negligible leading to more efficient sample heating, raising the absorption coefficient even further. Additionally, it is possible for 2PA to even further increase absorption, since absorption at 1.55 eV is greatly increased [11].

As a further test of this idea, measurement of the absorption spectrum of the dark brown material both at room temperature and elevated temperatures would certainly help to confirm this method of transition from 3PA to linear absorption. The effects of 2PA, if it occurs, would be more difficult to ascertain.

Finally, the lack of crystal orientation dependence can be addressed. Although cumulative heating does not occur, the ferroelectric properties of lithium niobate are likely destroyed due to the rapid rise in temperature. The Curie temperature is 1140 °C and, judging by the change in colour in the 'patch' experiment, this temperature is likely reached very quickly, so any nonlinear effects would be short-lived. Further, if there is indeed a lack of oxygen in the resulting material, it can no longer be considered to be lithium niobate in its most useful form. Exploring the effects of femtosecond ablation at different wavelengths might be an avenue to explore to see if nonlinear effects play a role in ablation.

6.4 Summary

The results of exploratory work on femtosecond laser micromachining of lithium niobate have been presented. Single and multiple pulse experiments were performed and the ablation threshold determined. The threshold did not depend on crystal orientation and decreased with an increasing number of pulses. In some cases, there were ripples on the crater bottoms, a phenomenon that is a field of research in itself.

The machining of grooves was also characterized. When machining grooves, increasing the effective number of pulses N_{eff} (i.e. decreasing cutting speed) gave rapidly increasing ablation depths until a threshold was reached, after which the grooves were nearly filled with amorphous material. The depth of these amorphous channels rapidly saturates and becomes nearly independent of N_{eff}. The ablation depth dependence on fluence showed gentle and strong ablation regimes. The amorphous channel depth depended almost linearly on fluence. Subsequent laser passes over amorphous channels eventually removed the amorphous material from the groove, indicating a dependence on the time between laser pulses. Crystal orientation was not a factor.

The results are understood in terms of incubation and waveguiding. The first pulses ablate some material and incubate a channel of material below the surface. With further pulses, increasing incubation accelerates ablation. At the threshold N_{eff}, the absorption coefficient has increased enough that the next pulse is able to melt a significant amount of material, which expands to fill the groove. It is suggested that, initially, the amorphous material is able to guide subsequent pulses to the bottom of the channel, resulting in a very slowly increasing depth with N_{eff}. Subsequent passes causes ablation once again since compositional changes in the amorphous material have relaxed. Irradiated samples appear thermally reduced, which would create colour centres leading to increased absorption and thus incubation. Confirmation of this explanation would include density and compositional measurements of the amorphous material, along with absorption measurements on incubated samples.

Multiple passes in the ablation regime yielded deep grooves, with laser polarization perpendicular to the groove giving the best results. This shows that femtosecond lasers are should indeed be able to create MEMS structures in lithium niobate. Fabrication of micro-cantilevers and bridges is described in the next chapter.

Chapter 7 Potential for MEMS Devices

The previous chapter lays the groundwork for the use of femtosecond laser pulses to be used as a tool for micromachining of MEMS structures in lithium niobate. This section will discuss the results as they pertain to potential devices and outline some logical next steps towards MEMS fabrication.

7.1 Femtosecond Laser as a Machining Method

To begin, with the goal of creating 'clean' features in lithium niobate in mind, femtosecond laser pulses appear to be a viable option. Using multiple pulses in the same location, craters can be created. Laser fluences below 10 J/cm^2 eliminate cracking of the substrate and minimize surface debris, even up to 100 pulses and, presumably, beyond. While crater walls are rough, they become increasingly smooth with a greater number of pulses. The creation of nice grooves is also possible. However, laser fluence and cutting speed must be such that the conditions for round ablation as described in Section 6.2 are met. The appeal of lithium niobate for MEMS use lies in its ferroelectric properties and the creation of amorphous channels would be of little use in this regard. The highest quality single-pass grooves in terms of morphology were obtained in the 'round' ablation regime, although if square ablation were maintained, with improved roughness, it would be appealing for device fabrication.

The threshold value obtained from these experiments was 1.5 J/cm^2. This is a notable parameter from a device fabrication point-of-view in that it is significantly higher than the threshold for metals (Cu: ϕ_{th} =460 mJ/cm^2 [61]) and semiconductors (Si: ϕ_{th} = 450 mJ/cm^2 [47], InP: ϕ_{th} =170 mJ/cm^2 [32]). If a thin film were to be deposited on lithium niobate, it could be patterned without ablating the substrate. This allows the possibility of using the femtosecond laser to create a desired electrode pattern for a device without the use of a mask. However, the incubation factor ξ was 0.74 (ξ = 1 implies no incubation), so the material can be modified without ablation. This modification was not evident on the surface using an optical microscope or SEM so the extent to which the material properties are affected remains to be investigated.

For both craters and grooves, there was no dependence of crater size or shape on crystal orientation. This is an advantage in micromachining in that only one set of parameters is required and no laser parameters need be changed when using different samples. The only concern is the laser polarization with respect to the cutting direction.

If linear only grooves are required, then maintaining a polarization perpendicular to the cutting direction gives the best results. For grooves that involve translating the sample in multiple directions, circular polarization would give uniform ablation in all directions.

In the machining of grooves with multiple passes, it is seen that deep grooves, high quality grooves can be created. The best groove morphology was obtained in the single-pass round ablation regime, although in no case was the amorphous channel observed below the groove. The groove depth increases logarithmically with number of passes. At 750 μm/s and 500 μm/s the depth appears to saturate above 10 passes. This saturation has been attributed to the groove acting as a lossy hollow waveguide, prohibiting the pulses from propagating deeper into the material due to scattering and absorption [32]. The maximum depth observed in these experiments was 100 μm. By varying the pulse fluence and number of passes, any depth up to that is attainable. However, a depth limit with number of passes was not apparent at 1000 μm/s, so even greater depths should be possible.

Chapter 6 gives suggestions for further characterization of the materials properties in order to gain a more thorough understanding of the laser interaction with lithium niobate. Similarly, there is much that can still be characterized in terms of possibilities for making a device. First, attempting to create improved 'square ablation' grooves would be worthwhile. If multiple passes improve the morphology (i.e. give smoother side walls) and give deeper grooves that remain 'square' this would certainly be useful, especially for ridge waveguides, which brings up the next suggestions. Two parallel grooves, with unmodified material in between should be sufficient to confine a light signal. Determining if a ridge waveguide can be made in this manner would be useful. Some parameters to explore in this respect are: the required groove depth, the number of passes required to give sufficiently smooth sidewalls and the size of the ridge (i.e. the spacing between the grooves). The minimum possible ridge size would also be of interest, to establish the parameters required to make a high quality grating. Removing a metal coating from a sample surface would also be a good test to perform to determine if, in fact, electrodes can be defined without damaging the substrate and its electro-optic properties. Attempting to drill or cut all the way through a substrate would also be useful. If sufficient depth can be attained with multiple passes to cut a sample in two, then this could be an alternative to the dicing saw as laser cutting does not seem as though it would cause any chipping. If the cutting of substrates were not possible, the maximum attainable depth would be a good quantity to know. If cutting is feasible, the optical quality of a cut edge could be studied as an alternative to mechanical polishing for waveguide facets. Finally, obtaining the smallest possible feature is often desirable. All of the experiments in this work were performed using a 5x microscope objective, which

proved to be the simplest to use, giving a beam radius of ~5 μm at the focal point. Experimentation using a larger magnification of 20x or 50x would be useful in determining the minimum attainable structure size with femtosecond micromachining.

As a side note, not only can femtosecond lasers be used to create microstructure in lithium niobate. They have also been shown capable of direct-writing waveguides into the bulk material [59]. With these capabilities, the potential for all-laser fabrication exists for lithium niobate devices.

7.2 MEMS Structures in Lithium Niobate

The fabrication of microstructures for MEMS in lithium niobate via laser ablation appears possible using femtosecond lasers. Micro-cantilevers and micro-bridges are among the more common structures used in microelectromechanical systems, and they are often used for sensors and actuators.

A cantilever with a triangular cross-section is the simplest type of structure to make using the set-up described in the previous chapter. The fundamental resonant frequency of a bridge with an equilateral triangular cross-section can be determined by Equations 7-1 and 7-2 [62], where E is the elastic modulus, I is the moment of inertia, g is the acceleration due to gravity, w is the weight per unit length, l is the bridge length and a is the triangle side length. By substituting $w = \rho \cdot A \cdot g$ and $E = \rho \cdot v_s^2$, where ρ is the mass density, A is the cross-sectional area and $v_s = 7300$ m/s [4] is the speed of sound in the material, as well as $a = 50$ μm, the resonant frequency as a function of the bridge length can be determine, as shown in Figure 7-1. The frequencies range from 75 MHz at 50 μm to 10 kHz at 4300 μm. These frequencies are well within those used for MEMS devices. While the feature length is quite large at lower frequencies, the bridge cross-section can be adjusted to compensate for this.

Triangular cantilevers and bridges were attempted and the results are shown in Figure 7-2. A structure with a flatter horizontal cross-section could be made by first cutting away more material around the groove to allow undercutting with the sample at a steeper angle relative to the beam. However, this comes at the expense of a longer fabrication process. Simply machining at a shallower angle could make a cantilever with a higher aspect ratio. It should be noted that the cantilever is raised relative to the substrate surface. This could be an indication of some residual stress in the structure.

$$f_1 = \frac{22.4}{2\pi} \sqrt{\frac{EIg}{wl^4}} \qquad \text{7-1}$$

$$I = 0.01804a^4 \qquad \text{7-2}$$
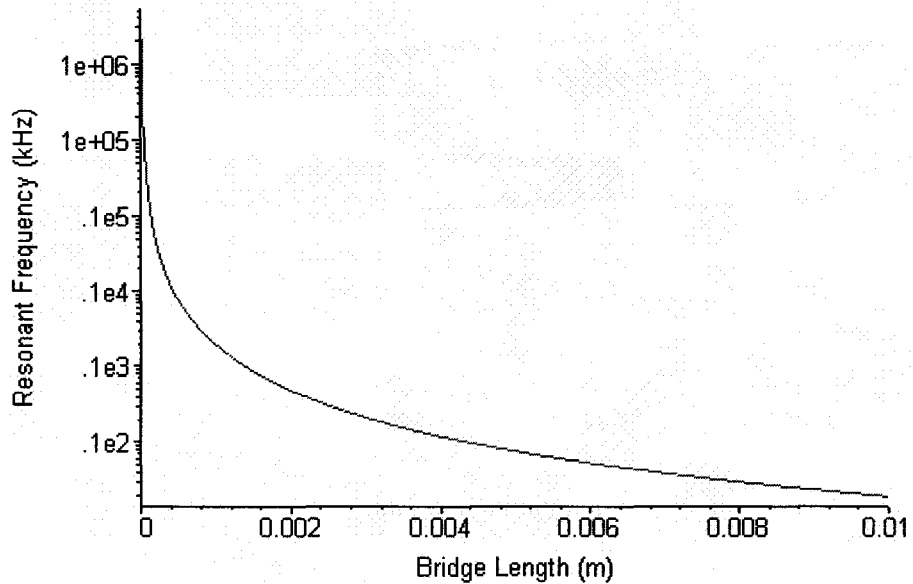
Figure 7-1: Resonant frequency as a function of length of a lithium niobate bridge fixed at both ends with an equilateral triangle cross-section of side length 50 μm.

There were some difficulties encountered in the machining process, the main one being the relatively short depth of focus of the machining/viewing lens. When the sample is tilted relative to the beam, only a narrow portion of the sample surface is in focus, making it difficult to locate the desired location for groove machining. This was simplified by marking the desired groove with a single pass when the sample is horizontal. However, more complex shapes (e.g. a rounded groove on an angle) would be quite difficult, requiring stepwise drilling and frequent repositioning of the sample and refocusing of the beam or else an automated system. Illumination of the sample was also a slight problem since the provided light to the viewing camera must be reflected from the sample at the proper angle. Slight repositioning of the sample requires large adjustments in the lamp location. So, improvements to the machining set-up are required to simplify the machining process. For these experiments, the sample was on manual rotation and tilt stages, so a first step would be to install motorized stages. In terms of structure fabrication, a first step would be to create a free bridge or cantilever without cutting unnecessarily into the substrate below. Developing a non-destructive process for determining if a bridge is free and characterizing its resonant frequency would be very useful.

A possible MEMS device configuration could involve a Mach-Zehnder interferometer with one arm undercut so that it is free to move. In this case, arm vibration could potentially modulate the index of refraction via the photoelastic effect and thus modulate the output intensity. The details of a design must still be worked out, but there is the potential to create a novel device in lithium niobate.
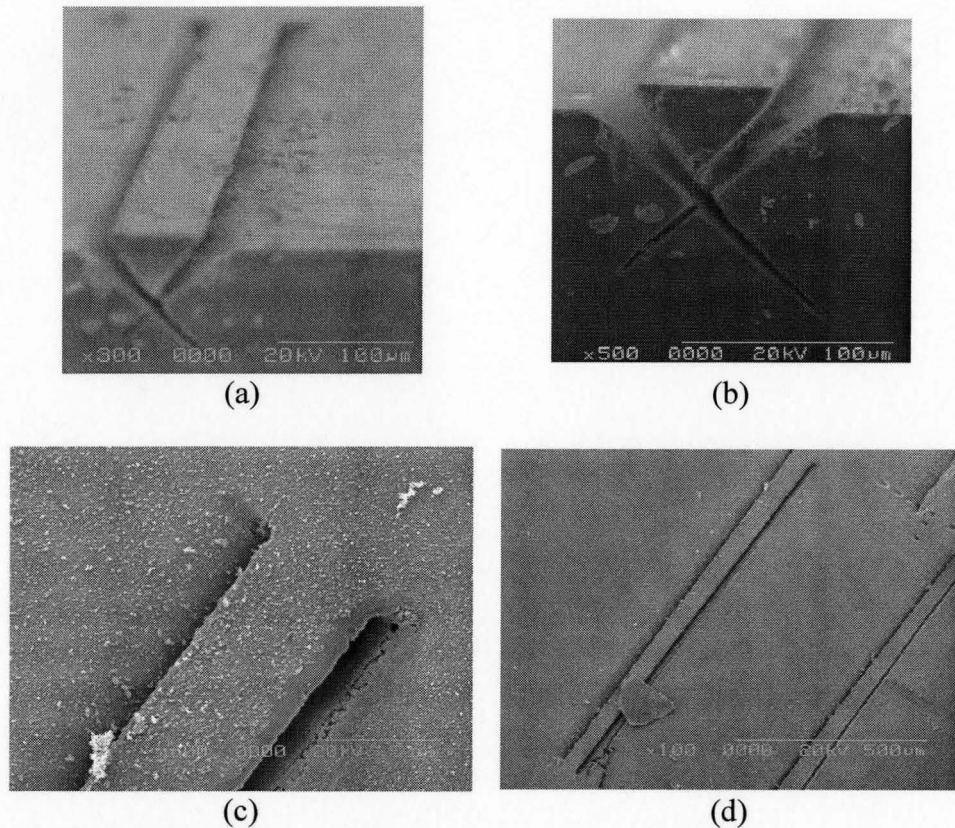
Figure 7-2: (a) A cantilever in lithium niobate, (b) Close-up of cantilever free end, (c) fixed end of cantilever and (d) Bridge in lithium niobate (partially covered with debris)

7.3 Summary

Femtosecond lasers are a viable option for machining structures in lithium niobate. Laser fluences below 10 J/cm^2 minimize sample cracking surrounding craters. For the machining of grooves, cutting speeds of 500 μm/s or greater are required so that amorphous channels are not created. Depths up to 100 μm were observed, with greater depths likely possible. The ablation threshold of 1.5 J/cm^2 opens the possibility of coating lithium niobate samples and selectively machining thin films without damage to the substrate. Crystal orientation is not a factor, although laser polarization with respect to the cutting direction is. Polarization perpendicular to the cutting direction is best, with circular polarization an option for nonlinear grooves. The fabrication of cantilevers and bridges was demonstrated. There remains much to be explored in the application of

femtosecond laser micromachining and lithium niobate to MEMS. Determination of a maximum groove depth, fabrication of a ridge waveguide and determination of the minimum ridge width, as well as exploration of the minimum feature size using different objective lenses are some avenues to pursue, as would the characterization of the mechanical properties of a bridge or cantilever. The use of a bridge in a Mach-Zehnder interferometer may be useful.

Chapter 8 Conclusion

Lithium niobate, LiNbO₃, is a very well studied ferroelectric compound. It has a complex structure and it exists in its most useful form in a narrow range of lithium dioxide content. It has been an important material in photonics due to its electro-optic, nonlinear optical, acousto-optic and photorefractive properties. Applications include, among others, optical switches and intensity modulators, as well as holographic data storage. It has potential in MEMS but the lack of a viable micromachining process has inhibited this application. This thesis is an exploratory study to determine the viability of using a femtosecond laser as a fabrication tool for lithium niobate.

A discussion of femtosecond lasers was presented. Femtosecond laser pulses have characteristic properties of large bandwidth and high peak power that make them ideal for many applications, including imaging and micromachining. Ti:sapphire lasers are among the most common femtosecond sources and, along with chirped-pulse amplification, are ideal for micromachining. Femtosecond pulses require indirect measurement techniques, such as intensity autocorrelation. The laser system used in these experiments consisted of a Ti:sapphire oscillator followed by a chirped-pulse amplifier.

Femtosecond laser machining can be used to create craters with little affect to the surrounding material, as well as grooves. These features have been well characterized in many materials. The crater diameter squared for single and multiple pulses depends logarithmically on the number of pulses. The threshold decreases with an increasing number of pulses. For grooves, the depth increases logarithmically with fluence with gentle and strong regimes present. The groove depth is inversely proportional to the cutting speed and depends linearly on the effective number of pulses. Laser ablation studies of lithium niobate to date have been limited, focussing mainly on deposition of thin films and the use of ultraviolet lasers. It has been identified that femtosecond pulses affect the composition and crystal structure of lithium niobate but there remains a need for further characterization.

Exploratory work on femtosecond laser micromachining of lithium niobate was carried out. Sample analysis consisted of polarized light microscopy followed by SEM or TEM imaging. Single and multiple pulse experiments were performed and the ablation threshold determined. The threshold did not depend on crystal orientation and decreased with an increasing number of pulses. In some cases, there were ripples on the crater

bottoms, a phenomenon that is a field of research in itself. Unexpectedly, in the machining of grooves, a rich range of behaviour, likely arising from the complex material structure and composition, was discovered. Depending on the processing conditions, it was demonstrated that machining can either result in deep, high-aspect ratio grooves with minimal surrounding damage or dramatically modify the lithium niobate to great depths with very little material removal.

The results for grooves were as follows. When increasing the effective number of pulses N_{eff} (i.e. decreasing cutting speed) rapidly increasing ablation depths were observed, until a threshold was reached, after which the grooves were nearly filled with amorphous material. The depth of these amorphous channels rapidly saturates and becomes nearly independent of N_{eff}. The ablation depth dependence on fluence showed gentle and strong ablation regimes. The amorphous channel depth depended almost linearly on fluence. Subsequent laser passes over amorphous channels eventually removed the amorphous material from the groove, indicating a dependence on the time between laser pulses. Crystal orientation was not a factor.

These results are understood in terms of incubation and waveguiding. The first pulses ablate some material and incubate a channel of material below the surface. With further pulses, increasing incubation accelerates ablation. At the threshold N_{eff}, the absorption coefficient has increased enough that the next pulse is able to melt a significant amount of material, which expands to fill the groove. It is suggested that, initially, the amorphous material is able to guide subsequent pulses to the bottom of the channel, resulting in a very slowly increasing depth with N_{eff}. Subsequent passes causes ablation once again since compositional changes in the amorphous material have relaxed. Irradiated samples appear thermally reduced, which would create colour centres leading to increased absorption and thus incubation.

Femtosecond lasers are a viable option for machining structures in lithium niobate. Laser fluences below 10 J/cm^2 minimize sample cracking surrounding craters. For the machining of grooves, cutting speeds of 500 µm/s or greater are required so that amorphous channels are not created. Depths up to 100 µm were observed, with greater depths likely possible. The ablation threshold of 1.5 J/cm^2 opens the possibility of coating lithium niobate samples and selectively machining thin films without damage to the substrate. Crystal orientation is not a factor, although laser polarization with respect to the cutting direction is. Polarization perpendicular to the cutting direction is best, with circular polarization an option for nonlinear grooves. The fabrication of cantilevers and bridges was demonstrated.

From this work, two major avenues for future research can be identified. The first involves a materials science approach. The picture of laser ablation processes associated with lithium niobate is not yet complete. An explanation of the interesting results that have been presented was proposed. Next experiments should involve further confirmation of this explanation and would include density and compositional measurements of the amorphous material, along with absorption measurements on incubated lithium niobate samples. Determining whether the observed phenomena occur in other complex materials would also be of interest

The second major research topic is an engineering project. There remains much to be explored in the application of femtosecond laser micromachining and lithium niobate to MEMS. Determination of a maximum groove depth, fabrication of a ridge waveguide and determination of the minimum ridge width, as well as exploration of the minimum feature size using different objective lenses are some avenues to pursue, as would the characterization of the mechanical properties of a bridge or cantilever. The use of a bridge in one arm of a Mach-Zehnder interferometer may be useful in sensing. Whatever the application may be, the development of a practical device that takes advantage of the varied properties of lithium niobate would be the ultimate goal.

This thesis has presented the results of a preliminary study on femtosecond laser micromachining of lithium niobate. Many results were unexpected which invites further research into laser-material interactions. It was also shown that there is a now a promising method for easily machining structures on lithium niobate, opening the path towards the development of a MEMS device. Despite the fact that lithium niobate has been so well studied and applied, there is still much to explore.

References

1 . M. Lawrence, *Reports on Progress in Physics*, **56**, 363-429 (1993)

2 . C. Sones, S. Mailis, V. Apostolopoulos, I.E. Barry, C. Gawith, P.G.R. Smith and R.W. Eason, *Journal of Micromechanics and Microengineering*, **12**, 53-57 (2002)

3 . F. Lacour, N. Courjal, M.-P. Bernal, A. Sabac, M. Bainier and M. Spajer, *Optical Materials*, **27 (8)**, 1421-1425 (2005)

4. Prokhorov, A.M. and Kuz'minov, Y.S. *Physics and Chemistry of Crystalline Lithium Niobate*. New York: IOP Publishing Ltd., 1990.

5. Wong, K.K. (ed.). *Properties of Lithium Niobate*. New York: INSPEC, Institution of Electrical Engineers, 1989.

6. Agullo-Lopez, F., Cabrera, J.M. and Agullo-Rueda, F. *Electro-optics: phenomena, materials and applications*. Toronto: Academic Press, 1994.

7. G. Malovchiko, V. Grachev, and O. Schirmer, *Applied Physics B,* **68**, 785-793 (1999)

8. D. Damjanovic, *Reports on Progress in Physics*, **61**, 1267-1324 (1998)

9 . J. Zhu, S. Zhao, D. Xiao, X. Wang, and G. Xu, *Journal of Physics: Condensed Matter*, **4**, 2977-2983 (1992)

10. A. Dhar and A. Mansingh, *Journal of Applied Physics*, **68**, 5804-5809 (1990)

11. L. Arizmendi, Cabrera, J.M. and Agullo-Lopez, F., *Journal of Physics C: Solid State Physics*, **17**, 515-529 (1984)

12. Saleh, B.E.A. and Teich, M.C. *Fundamentals of Photonics*. Toronto: John Wiley Sons, Inc., 1991.

13. L. Arizmendi, *Physica Status Solidi A*, **201 (2)**, 253-283 (2004)

14. I.E. Barry, G.W. Ross, P.G.R. Smith, R.W. Eason and G. Cook, *Materials Letters*, **37**, 246-254 (1998)

15. U. Keller, *Nature*, **424**, 831-838 (2003)

16. M. Pittman, S. Ferré, J.P. Rousseau, L. Notebaert, J.P. Chambaret G. and Chériaux, *Applied Physics B*, **74**, 529-535 (2002)

17. T. Fuji, A. Unterhuber, V.S. Yakovlev, G. Tempea, A. Stingl, F. Krausz and W. Drexler, *Applied Physics B*, **77**, 125-128 (2003)

18. W. Rudolph, P. Dorn, X. Liu, N. Vretenar and R. Stock, *Applied Surface Science*, **208-209**, 327-332 (2003).

19. H. Zhu, J. Chen, H. Gao, H.Xie, R. Li and Z. Xu, *Applied Surface Science*, **248**, 75-78 (2005).

20. H. Schwoerer, *Topics in Applied Physics 96: Femtosecond Technology for Technical and Medical Applications*, 235-253 (2004).

21. Rullière, C. (ed.). *Femtosecond Laser Pulses: Principles and Experiments*. New York: Springer-Verlag, 1998.

22. Website of the Biomolecular and Chemical Physics Group at the University of Strathclyde, Glasgow, September 2005:
http://bcp.phys.strath.ac.uk/ultrafast/dictionary/cpa/cpa.html

23. Siegman, A.E. *Lasers*. Sausalito, California: University Science Books, 1986.

24. J. Krüger and W. Kautek, *Advances in Polymer Science*, **168**, 247-289 (2004)

25. L. Shah, J. Tawney, M. Richardson and K. Richardson, *Applied Surface Science*, **183**, 151-164 (2001)

26. D. Ashkenasi, G. Müller, A. Rosenfeld, R. Stoian, I.V. Hertel, N.M. Bulgakova and E.E.B. Campbell, *Applied Physics A*, **77**, 223-228 (2003)

27. X. Liu, D. Du and G. Mourou, *IEEE Journal of Quantum Electronics*, **33 (10)**, 1706-1716 (1997)

28. X.C. Wang, G.C Lim, H.Y. Zheng, F.L. Ng, W. Liu and S.J. Chua, *Applied Surface Science*, **228**, 221-226 (2004)

29. J.M. Liu, *Optics Letters*, **7 (5)**, 196-198 (1982)

30. Y. Jee, M.F. Becker and R.M. Walser, *Journal of the Optical Society of America B*, **5 (3)**, 648-659 (1988)

31. A. Hertwig, S. Martin, J. Krüger and W. Kautek, *Applied Physics A*, **79**, 1075-1077 (2004)

32. A. Borowiec and H.K. Haugen, *Applied Physics A*, **79**, 521-592 (2004)

33. A. Boulle, L. Canale, R. Guinebretière, C. Girault-Di and A. Dauger, *Thin Solid Films*, **429**, 55-62 (2003)

34. J.A. Chaos, J. Gonzalo, C.N. Afonso, J. Perrière and M.T. García-González, *Applied Physics A*, **72**, 705-710 (2001)

35. S. Preuss, M. Späth, Y. Zhang and M. Stuke, *Applied Physics Letters*, **62 (23)**, 3049-3051 (1993)

36. M. Affatigato, K. Tang and R.F. Haglund Jr., *Applied Physics Letters*, **65 (14)**, 1751-1753 (1994)

37. M. Sorescu, J.D. Barrie, J.J. Martin and E.T. Knobbe, *Solid State Communications*, **94 (5)**, 407-411 (1995)

38. G.P. Luo, Y.Q. Lu, Y.Y. Zhu, Y.L. Lu, X.L. Guo, C.Z. Ge, Z.G. Liu, N.B. Ming, J.W. Wu and Z.H.Lu, *Japanese Journal of Applied Physics Part 2*, **35 (12a)**, L1593-L1595 (1996)

39. P. Bunton, M. Binkley and G. Asbury, *Applied Physics A*, **65**, 411-417 (1997)

40. H.-W. Chong, A. Mitchell, J.P. Hayes and M.W. Austin, *Applied Surface Science*, **201**, 196-203 (2002)

41. P.R. Herman, R.S. Marjoribanks, A. Oettl, K. Chen, I. Konovalov and S. Ness, *Applied Surface Science*, **154-155**, 577-586 (2000)

42. D.C. Deshpande, A.P. Malshe, E.A. Stach, V. Radmilovic, D. Alexander, D.Doerr and D. Hirt, *Journal of Applied Physics*, **97**, 074316 (2005)

43. P. Galinetto, D. Ballarini, D. Grando and G. Samoggia, *Applied Surface Science*, **248**, 291-294 (2005)

44. E.E.B. Campbell, D. Ashkenasi and A. Rosenfeld, *Materials Science Forum*, **301**, 123-144 (1999)

45. R. Kelly and A. Miotello, *Applied Surface Science*, **96-98**, 205-215 (1996)

46. J. Bonse, J.M. Wrobel, J. Kruger and W. Kautek, *Applied Physics A*, **72**, 89-94 (2001)

47. E. Coyne, J.P. Magee, P. Mannion, G.M. O'Connor and T.J. Glynn, *Applied Surface Science*, **229**, 148-160 (2004)

48. W. Kautek, J. Krüger, M. Lenzner, S. Sartania, C. Spielmann and F. Krausz, *Applied Physics Letters*, **69**, 3146-3148 (1996)

49. R. Kitano, K. Ozono, M. Obara and H. Tsuda, *Photon Processing in Microelectronics and Photonics II,Proceedings of SPIE*, **4977**, 386-393 (2003).

50. A.M. Ozkan, A.P. Malshe, T.A. Railkar, W.D. Brown, M.D. Shirk and P.A. Molian, *Applied Physics Letters*, **75**, 3716-3718 (1999)

51. J. Reif, F. Costache, M. Henyk and S.V. Pandelov, *Applied Surface Science*, **197-198**, 891-895 (2002)

52. G. Seifert, M. Kaempfe, F. Syrowatka, C. Harnagea, D. Hesse and H. Graener, *Applied Physics A*, **81**, 799-803 (2005)

53. J.E. Sife, Jeff F. Young, J.S. Preston and H.M. van Driel, *Physical Review B*, **27 (2)**, 1141-1154 (1983)

54. Jeff F. Young, J.S. Preston, H.M. van Driel and J.E. Sipe, *Physical Review B*, **27 (2)**, 1155-1181 (1983)

55. L. Jiang and H.L. Tsai, *International Journal of Heat and Mass Transfer*, **48**, 487-499 (2005)

56. N. Bärsch, K. Körber, A. Ostendorf and K.H. Tönshoff, *Applied Physics A*, **77**, 237-242 (2003)

57. Crystal Technology product data sheet for lithium niobate optical crystals: http://www.crystaltechnology.com/LN_Optical_Crystals.pdf (2006)

58. R.A. Ganeev, I.A. Kulagin, A.I. Ryasnyansky, R.I. Tugushev and T. Usmanov, *Optics Communications*, **229**, 403-412 (2004)

59. L. Gui, B. Xu and T.C. Chong, *IEEE Photonics Technology Letters*, **16 (5)**, 1337-1339 (2004)

60. B.C. Stuart, M.D. Feit, S. Herman, A.M.Rubenchik, B.W. Shore and M.D. Perry, *Journal of the Optical Society of America B*, **13**, 459-468 (1996)

61. S. Nolte, C. Momma, H. Jacobs, A. Tünnermann, B.N. Chichkov, B. Wellegehausen and H. Welling, *Journal of the Optical Society of America B*, **14**, 2716-2722 (1997)

62. Young, Warren C. *Roark's Formulas for Stress and Strain, Sixth Edition*. Toronto: McGraw-Hill, Inc., 1989.